5

Machining

5-1

Optimization of cutting parameters for drilling Nickel-based alloys using statistical experimental design techniques

L. J. Zhang, T. Wagner and D. Biermann
Institute of Machining Technology (ISF), Baroper Str. 301, Technische Universität Dortmund, 44227 Dortmund, Germany

Abstract. Nickel-based alloys are frequently applied in the aerospace and power generation industries due to their excellent material properties, such as high temperature strength and high corrosion resistance. These advantageous material properties, however, result in challenges for cutting operations. Contrary to turning, where good results for the machining of nickel-based alloys have been obtained, drilling processes are less investigated until now. In general, coated cemented carbide drills have been proven to show good performances in drilling operations based on their higher strength compared to high speed steel (HSS) tools. Hence, they can be utilized with more efficient process parameters, whereby tool life will likely be reduced as a consequence of the higher loads. In order to find reasonable trade-offs between efficiency and tool life, a multi-objective optimization based on both criteria is presented in this article. The optimization of the cutting parameters is performed for drilling the popular nickel-based alloy Inconel 718. It is assisted by empirical models based on statistical experimental design techniques. By these means, the trade-off surface between process efficiency and tool wear can be approximated within a small experimental effort. In addition, the dominant mechanisms behind the tool wear for different process parameters are discussed.

Keywords: Nickel-based alloys, Inconel 718, Drilling, Optimization

1. Introduction

High temperature materials, such as nickel-based alloys, are often used to produce components in the aerospace and gas turbine industries [1]. In particular, they are appropriate for the hot sections of turbine parts due to their good tensile, fatigue, creep, and rupture strength at high temperatures up to 700 °C [2]. During machining processes, however, the low thermal conductivity and high tendency to work hardening of nickel-based alloys could make the cutting process problematic. High levels of tool wear and a poor surface finish are typical issues for the machining of these materials [3-5]. In comparison to turning processes, drilling operations are even more challenging. The cutting zone of those processes is more closed than the one of turning operations. As a consequence, high cutting temperatures result in high levels of tool wear and an inefficient chip evacuation [6]. TiAlN (or TiAlN multi-layered) coated cemented carbide drills have commonly been used to deal with nickel-based alloys because of a good cutting performance by the cemented carbide and a superior oxidation protection under high temperatures by the TiAlN (based) coating due to a protective aluminium oxide layer at the surface [7]. In general, the amorphous aluminium oxide forms on the surface of the TiAlN coating realize a higher operating temperature during the machining in comparison to most other coatings, such as TiN or TiCN. However, the range of the process parameters was still limited in the case of drilling high temperature materials with TiAlN coated tools, as the high cutting temperatures result in higher levels of tool wear compared to the one of other workpiece materials like steels or iron-based alloys [8-9]. Increasing the process parameters can enhance the cutting performance, but the tool life will be reduced correspondingly. Lower process parameters can reduce the tool wear, but increase the operating time. In this paper, the trade-off surface between these two criteria, tool life and performance, is empirically approximated. A statistical experimental design is employed to obtain the process parameters resulting in optimal trade-offs.

2. Experimental setup

Drilling experiments were carried out to build up a statistical empirical model for the optimization of the process parameters. These experiments were conducted on a 4-axis machining centre GROB BZ 600. Whereas the efficiency of the process parameters could be directly calculated by means of the material removal rate Q_w, circular arrays of holes were drilled for each experimental setup (cf. Table 1) in order to evalaluate the tool life. After each drilled hole, the tool wear at specific positions of the drills, namely the primary cutting edge, the minor cutting edge, the chisel edge and the flute, were inspected optically and recorded using a light optical microscope. An experiment was stopped as soon as an average flank

S. Hinduja and L. Li (eds.), *Proceedings of the 37th International MATADOR Conference*,
DOI: 10.1007/978-1-4471-4480-9_5,

wear of VB = 0.25 mm or a maximum flank wear of VB_{max} = 0.5 mm was reached. The corresponding tool life volume V_w was recorded as wear criterion.

2.1. Workpiece

Inconel 718, one of the most important nickel-based alloys, was supplied as face-milled cylindrical plates with a diameter of d = 130 mm and a thickness of δ = 35 mm. The plates were solution heat-treated and have a hardness of 382 HBW 10/3000 (42 HRC). The chemical composition of the material is shown in Table 1.

Table 1. Chemical composition of the workpiece material

Ni+Co	Fe	Cr	Cb	Mo	Ti+Al
54.01	18.43	17.83	5.19	2.93	1.49

2.2. Tool

Cemented carbide drills (K10/20) having TiAlN coatings were employed. The drill diameter and the maximum cutting length were d = 8.5 mm and l_c = 47 mm, respectively. The drill point angle was designed as σ = 120°. The cutting edge is composed of a concave edge near the periphery and a straight edge near the chisel edge. For all drills considered in the experiments, the cutting edges were prepared and measured by a structured light microscope. Basic statistics of the cutting edge parameters are detailed in Table 2. The values Sα and Sγ indicate the asymmetry of the curvature. Their ratio k = 1 means a symmetrically rounded edge. The distance Δr indicates the general magnitude of the rounding. A sharper edge has a smaller Δr value.

Table 2. Cutting edge geometry of the new drilling tools

radius			k-factor			Δr		
mean	min	max	mean	min	max	mean	min	max
9	8	10,1	0,798	0,491	1,111	15,5	9,8	21,4
9	7,9	10	0,717	0,405	1,056	19,4	15,1	23,6
Sα			**Sγ**			**chipping**		
mean	min	max	mean	min	max	mean	max	
20,9	11	31,6	24,3	13,5	35,5	1,5	5,1	
24,9	18,5	32,3	31,1	13,6	49	1,2	4	

2.3. Design of experiments

The cutting speed and the feed rate were varied from v_c = 20 m/min to v_c = 60 m/min and from f = 0.04 mm/rev to f = 0.16 mm/rev, respectively, in order to analyze a wide spectrum of tool wear levels. In order to maximize the number of factor steps, the first six experiments were designed using Latin hypercube sampling [10]. The two additional experiments were sequentially planned based on the available evaluations. Using the criterion of the SMS-EGO [11], the new experiments aimed at improving the approximation of the trade-off surface between efficiency and tool wear. The direction of the feed rate was horizontal for a center drilling. The lubricant used was a water-based 6% emulsion supplied by an internal cooling setting with a pressure of p = 20 bar. The experimental design and the observed response values are provided in Table 3.

Table 3. Experimental designs and the corresponding observations of the considered response values

v_c [m/min]	f [mm/rev]	n [rev/min]	V_w [mm³]	Q_w [mm³/min]
20	0.15	748	29791.13	6366.79
45	0.1	1685	7944.30	9561.54
60	0.11	2246	3972.15	14019.42
35	0.16	1310	9930.38	11893.76
50	0.14	1872	1986.08	14871.73
30	0.12	1123	25818.98	7646.96
25	0.08	936	77456.95	4249.07
35	0.04	1392	39721.51	3159.56

3. Results and discussion

3.1. Tool wear

The drilling operations of Inconel 718 are more complex than the ones of steels with the same hardness. Hence, the drilling tools of all experiments suffered from high stresses, high cutting temperatures in the cutting zone, and high forces during the process. These effects result in a strong wear of the drilling tool. The empirical measurements of the tool life volume V_w were used as basis for computing an empirical model which can be used for the optimization of the tool wear. In order to not assume any functional form of the response, modern empirical models of the design and analysis of computer experiments were used [12]. In these models, no trend function and a Gaussian correlation kernel were applied. A leave-one-out cross-validation resulted in a determination coefficient of R2 = 0.85. The model could thus be used to predict the tool life volume V_w. The model of the tool life volume is shown in Fig. 1. It rapidly decreases with increasing cutting speed v_c and feed rate f. The mechanisms behind this decrease are explained in the following.

3.1.1. Flank wear

The flank wears after experiments with different cutting speeds v_c and almost the same feed rate f are shown in Fig. 2. It is visible that the higher cutting speed of v_c = 50 m/min (right) induced more heat in the cutting zone, which caused a high thermal load on the drilling tool. In conjuction with mechanical stresses in the flow zone of the tool-workpiece-interface, the flank wear of

the drilling tool for the experiment with the higher cutting speed is thus significantly higher leading to the decrease in the tool life volume. In contrast, the variation of feed rates did not have a significant influence on the flank wear.

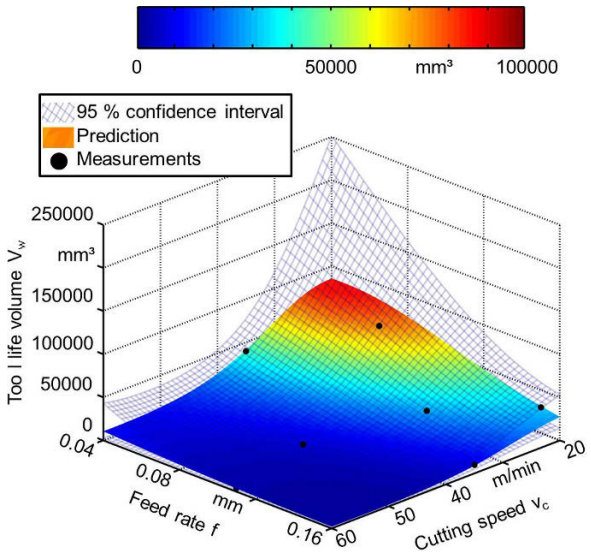

Fig. 1. Observed values of the material removal volume V_w (black dots) and model prediction of V_w (colored surface) over the considered ranges of the feed rate f and the cutting speed v_c

Chipping on the cutting edges of the drills was found in all the experiments except in the test with the lowest cutting speed of $v_c = 20$ m/min and the feed rate of f = 0.15 mm/rev.

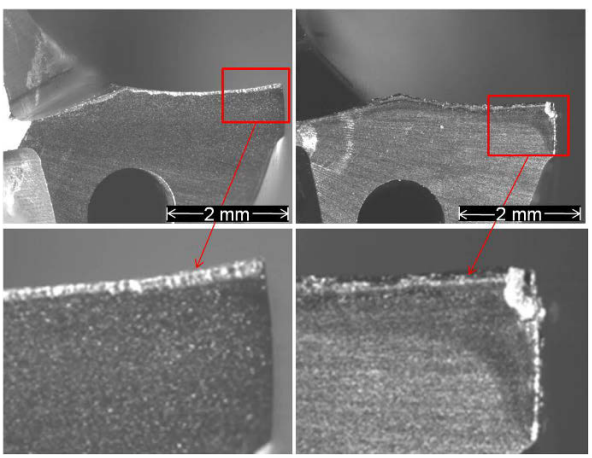

Fig. 2. Flank wear comparison of the process parameters $v_c = 20$ m/min, f = 0.15 mm/rev (left) and $v_c = 50$ m/min, f = 0.14 mm/rev (right) for a cutting length of L = 35 mm

3.1.2. Wear of the chisel edge and the rake face

The effect of the feed rate f on the wear of the chisel edge and the rake face are analyzed in Fig. 3 and 4. For lower values of the feed rate f (left), the wear was marginal. However, it could be found that the highest feed rate f = 0.16 mm/rev led to a rather large plastic deformation of the chisel edge compared to the test with the lower feed rate f = 0.04 mm/rev. This is due to the higher feed rate, with which more material is pushed and extruded under the chisel point during one revolution. In conjuction with that, the rake face in the tests with higher feed rates was also more stressed as shown in Fig. 4 and the tool life volume V_w is decreased.

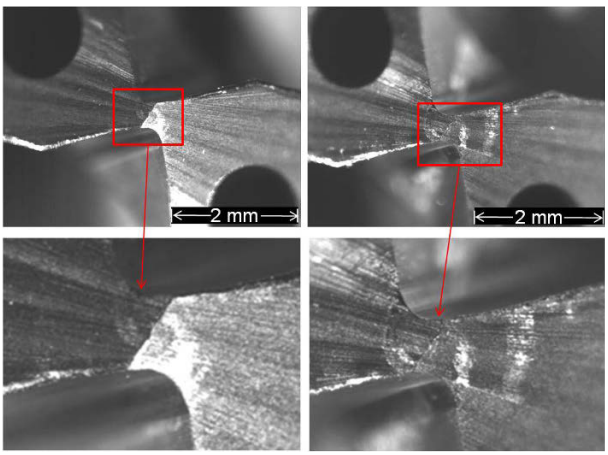

Fig. 3. Chisel edge wear comparison of the process parameters $v_c = 35$ m/min, f = 0.04 mm/rev (left) and $v_c = 35$ m/min, f = 0.16 mm/rev (right) for a cutting length of L = 35 mm

3.2. Multi-objective optimization

The material removal rate Q_w is calculated using the simple formula $Q_w = f * n * \pi * (d/2)^2$. It is thus linearly increasing with the feed rate f and the cutting speed v_c. As a consequence, the effects of cutting speed v_c and feed rate f on tool life volume V_w and material removal rate Q_w are opposing. It seems not to be possible to optimize both criteria at the same time. Nonetheless, a model-based multi-objective optimization of the empirical models of both quality indicators was performed. To accomplish this, a regular grid of points with steps of 1 m/min in the cutting speed v_c and steps of 0.01 mm of the feed rate f was evaluated on the empirical models. Interestingly, not all parameter settings resulted in a trade-off in which no criterion can be improved without deteriorating the other. There were possibilities to simultaneously improve both of them by varying the cutting speed v_c and the feed rate f. This is shown in Fig. 5 (right), in which the gray points depict all evaluations of the grid, whereas the red points highlight the ones which cannot be improved in both objectives. These points represent the optimal trade-off surface, from which

the final parameter setting can be chosen, e. g. based on the current price of a machine hour and a drilling tool.

The corresponding parameter vectors are also shown (left). The desired trade-offs, again highlighted using red color, are obtained for values of the cutting speed from $v_c = 20$ m/min to $v_c = 45$ m/min and for $f = 0.04$ mm/rev to $f = 0.16$ mm/rev, whereby these parameters have to be increased accordingly.

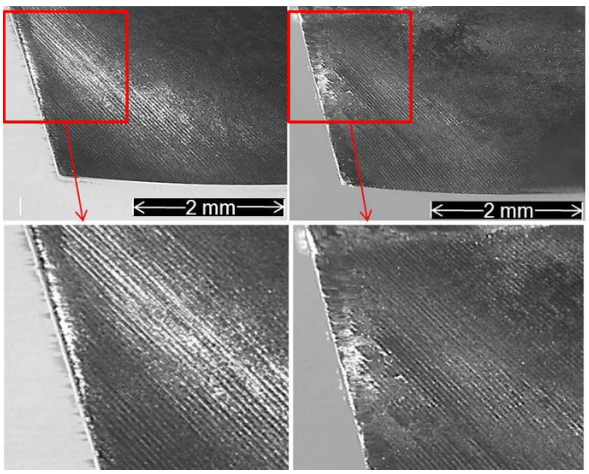

Fig. 4. Rake face wear comparison of the process parameters $v_c = 35$ m/min, $f = 0.04$ mm/rev (left) and $v_c = 35$ m/min, $f = 0.16$ mm/rev (right) for a cutting length of $L = 35$ mm

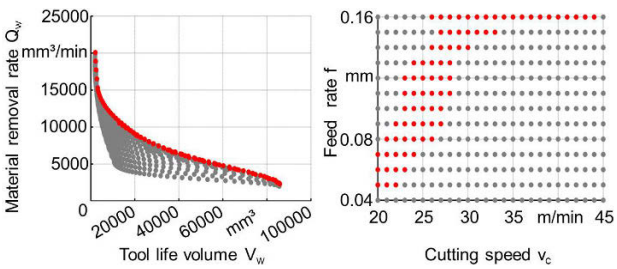

Fig. 5. Visualization of the possible and optimal trade-offs (left) and the corresponding process parameters (right)

4. Conclusion

In this paper, drilling operations of Inconel 718 using TiAlN coated cemented carbide drills were carried out. The experiments conducted with varying process parameters have shown significant effects of these parameters on the tool life volume and the material removal rate. Higher feed rates reduced the operating time, but led to more plastic deformation on the chisel edge. The same holds for higher cutting speeds for which the tool cutting edges encounter higher thermal loads and mechanical stresses. By using modern techniques of statistical experimental design and principles from multi-objective optimization, it was found that cutting speeds from $v_c = 20$ m/min to $v_c = 45$ m/min and appropriately chosen settings of the feed rate f result in optimal trade-offs between both criteria.

Acknowledgments: The work presented in this paper was supported by the Graduate School of Energy Efficient Production and Logistics, North-Rhine Westphalia, Germany and is based on investigations of the project D5 “Synthesis and multi-objective model-based optimisation of process chains for manufacturing parts with functionally graded properties” as part of the collaborative research center SFB/TR TRR 30, which is kindly supported by the Deutsche Forschungsgemeinschaft (DFG).

References

[1] Adam P, (1998) Fertigungsverfahren von Turboflugwerken. Birkhäuser, Basel

[2] Loria EA, (1988) The status and prospects of alloy 718. Journal of Metal 40:36–41

[3] Choudhury IA, El Baradie MA, (1998) Machinability of nickel-based super alloys: A general review. Journal of Materials Processing Technology 77:278–284

[4] Thakur DG, Ramamoorthy B, Vijayaraghavan L, (2009) Machinability investigation of Inconel 718 in high-speed turning. International Journal of Advanced Manufacturing Technology 45:421–429

[5] Arunachalam R, Mannan MA, (2000) Machinability of nickel-based high temperature alloys. Machining Science and Technology 4:127–168

[6] Ezugwu EO, Lai CJ, (1995) Failure modes and wear mechanisms of M35 high-speed steel drills when machining Inconel 901. Journal of Materials Processing Technology 49:295–312

[7] Sharman ARC, Amarasinghe A, Ridgway K, (2008) Tool life and surface integrity aspects when drilling and hole making in Inconel 718. Journal of Materials Processing Technology 200:424–432

[8] Klocke F, Gerschwiler K, Frisch R, Lung D, (2006) PVD-coated tools and native ester – an advanced system for enviromentally friendly machining. Surface and Coatings Technology 201:4389–4394

[9] Chen YC, Liao YS, (2003) Study on wear mechanisms in drilling of Inconel 718 superalloy. Journal of Materials Processing Technology 140:269–273

[10] McKay MD, Conover WJ, Beckman, RJ, (1979) A comparison of three methods for selecting values of input variables in the analysis of output from a computer code. Technometrics 21:239–245

[11] Wagner T, Emmerich MTM, Deutz A, Ponweiser W, (2010) On expected-improvement criteria for model-based multi-objective optimization. In: Schaefer R, Cotta C, Kolodziej J, Rudolph G (eds.), Proc. 11th Int’l Conf. Parallel Problem Solving from Nature (PPSN XI). Springer, Berlin

[12] Biermann D, Weinert K, Wagner T, (2008) Model-Based Optimization Revisited: Towards Real-World Processes. In: Michalewicz Z, Reynolds RG (eds.), Proc. 2008 IEEE Congress on Evolutionary Computation (CEC 2008). IEEE press, Los Alamitos, CA.

5-2

Machining performance of a graphitic SiC-Aluminium matrix composite

V. Songmene, R. D. Njoya and B. T. Nkengue
Department of Mechanical Engineering; Ecole de Technologie Supérieure (ÉTS); Université du Québec,
1100 Notre-Dame Street West, Montreal, QC, H3C 1K3, Canada

Abstract. Graphitic SiC-reinforced aluminium matrix composites were developed for high wear resistance application as replacement for cast iron, where lower part weight, high thermal conductivity and diffusivity are desired. Original graphitic metal matrix composites consisted of an aluminium matrix reinforced with both hard particles (SiC) for wear resistance and soft particles (nickel-coated graphite particles) for improved friction and machinability. Coating the graphite with nickel improves the wettability of the coated particle and thus facilitates its incorporation into the aluminium alloy, but adversely, also leads to the formation of nickel-based intermetallic precipitates (Al_3Ni), which can have adverse effects on the machinability of the composite. Also, the machining of this type of composite, as that of most metals, generates fine metallic particle that can be detrimental to the machine-tools parts' reliability and to occupational health and safety. This paper investigates the machining strategies to cost effectively machine a graphitic SiC-aluminium matrix composite made of an A356 aluminium alloy reinforced with 10vol%SiC and 4vol%Gr. The machinability is evaluated through tool wear, tool life and fine metallic particle emission. Empirical models governing the tool life and the fine metallic particle emission are developed to help determining the machining conditions leading to economical, ecological and occupational safe machining practices.

Keywords: Composite, dry milling, tool life, fine metallic particle.

1. Introduction

The strength and the physical properties of the composite materials are improved by the presence of the reinforcing particles. However, the rapid tool wear and the associated poor surface finish during machining MMCs are the leading drawbacks of the existence of the reinforcement particles as well [1]. In order to improve the machinability and the friction properties of particulate composites, aluminium MMC reinforced with both soft lubricating graphite particles and hard silicon carbide particles was developed [2,3,4,5]. Rohatgi, Bell and Stephenson [2] demonstrated the beneficial effects of a dispersion of graphite within the composite, which acts as a solid lubricant in aluminium silicon alloys. The introduction of both soft graphite particles and hard silicon carbide particles into the aluminium matrix improves its wear resistance while the graphite lowers the coefficient of friction of the resultant composite.

The first composite of this family, GrA-Ni 10S-4G, consisted of the A356 aluminium matrix reinforced with 10vol% SiC and 4vol% nickel-coated graphite [7]. By coating the graphite with nickel, the wettability of the coated particle is improved and this facilitates its incorporation into the aluminium alloy [3], but adversely, also leads to the formation of nickel-based intermetallic precipitates (Al_3Ni). Both the Al_3Ni precipitates and the SiC particles can have adverse effects on the machinability of the composite. Hard and abrasive particles such as SiC reinforcing particles and Al_3Ni intermetallics abrade the tool flank face, causing excessive wear. While studying the performance of the GrA-Ni 10S4G when machined with diamond tools, Songmene and Balazinski [8] found that diamond-coated carbide tools outperform polycrystalline diamond tools in terms of productivity while polycrystalline diamond tools produce a better surface finish on the part.

During the machining of this type of composite, fine metallic particle are emitted. These fine particles can be detrimental to the machine-tools parts' reliability and to occupational health and safety. Some researchers [9, 10-16] have investigated the emission of metallic particle during machining but very limited work was done for metal matrix composites. It was found that during machining of SiC-reinforced MMC, a tool with smooth coating emits more dust than rough coating with sharp structure [19]. The authors [19] attributed it to the wavier shear plane during machining with s of a rough surface coated tool as they also identified the friction at the shear plane to be the main source of dust emission.

The purpose of this work is to examine the performance of the GrA-Ni 10S-4G composite during dry milling process using carbide cutting tools. The machining process performance indicators used include the tool wear, the tool life and the emission of fine metallic particle.

2. Experimental procedure

2.1. Workpiece material

The workpiece used for this work is a GrA-Ni 10S.4G composite. It consists of an aluminium matrix reinforced by SiC (10-15 µm) and nickel coated graphite particles (100-150 µm). Its microstructure (Fig. 1) consists of a matrix of aluminium-silicon (grey) with a 10 vol% dispersion of SiC particles (small black phase) and 5 vol% coarser graphite particles (large black phase). Also found in the matrix are 6 vol% Ni-based intermetallic precipitates (Al_3Ni), which are formed on solidification of the alloy as a result of the dissolution of the nickel coating in molten aluminium. Graphite improves the machinability by lubricating the cutting and facilitating chip breaking [3, 5]. It also improves the composite tribological properties [4, 6]. GrA-Ni 10S 4G composite is designed for high wear resistance applications (cylinder liners and brake rotors) as replacement for grey cast iron [3].

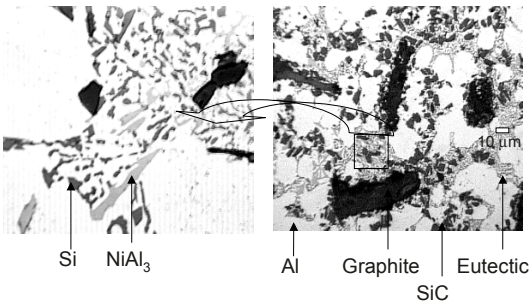

Fig. 1. Description of GrA-Ni 10S 4G composite [7]

2.2. Machine-tool and cutting tools

The machining operation was performed on a CNC milling machining tool (10,000 rpm, 17 kW), using an Iscar ADK-D1.50 helimill cutter (Clearance angle : 11°; Lead angle : 90°; Rake angle : 8°; Number of teeth: 3; Tool diameter: 30.48 mm). The inserts used were Iscar ADKR 1505 PDR-HM (clearance angle: 15°; wiper clearance angle: 15°; entering angle: 90°; corner radius: 0.8 mm), TiCN-coating.

In order to increase the metallic particle emission measurement efficiency a plexiglas box is added on the table so that the machining process is carried out in a closed and limited environment (Fig. 2). Polluted air within the closed box is dragged into the dust measurement unit through a 10 mm diameter polyester tube (about 1 foot) and kept straight to minimize dust lost in the tube. The dust monitoring unit used (Fig. 2) is the TSI8520 Dust track laser aerosol monitor capable of measuring mass concentration ranging from 0.1 to 100 mg/m^3 and particle size ranging from 0.1 to 10 µm. The air dragged passes through a 2.5 µm impactor (filter) before entering into the dust measurement unit (laser photometer). The system flow rate was set to 1.7 L/min.

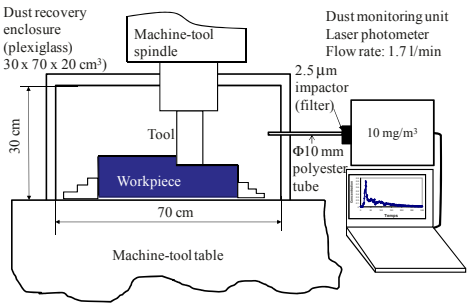

Fig. 2. Schematic representation of the experimental set-up used

3. Results and discussions

The main wear pattern observed was regular flank wear (Fig. 3). The wear of the flank face is similar to that observed in other studies [17, 18]. Flank wear is due to the abrasive action of the reinforced particles within the composite on the flank face of the tool. The harder SiC particles (2700-3500 HV), Figure 4, grind the face of the tool on similar way of a grinding wheel.

The flank wear (VB) was measured and the data plotted to show the evolution of the flank wear as a function of the volume of chip removed (Fig. 5). As expected, the tool flank wear rate increased with the increase in cutting speeds. Curves similar to those presented in Fig. 6 were constructed for other machining parameters (feed, depth of cut and tool immersion) and based on a 0.3 mm flank wear criterion, the tool life curves as a function of these machining parameters were constructed (Fig. 6)

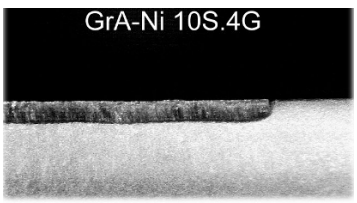

Fig. 3. Image of a worn insert after 10 minutes of cut. Cutting speed: 61 m/min, Feed rate: 0.254 mm **[5]**

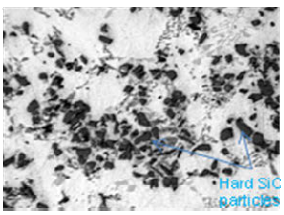

Fig. 4. SEM image of GrA-Ni 10S-4G composite (200 x) showing hard and abrasive SiC-reinforcing particles

The initial wear rate (Fig. 5) increases when the cutting speed is increased. Similar results were found for the effects of feed rate, and that of the width of cut on tool wear. This is the result of the increased normal force on the flank face of the tool.

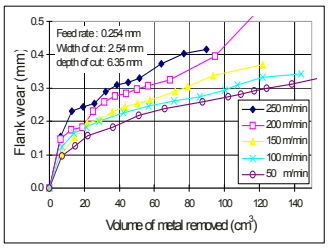

Fig. 5. Flank wear as function of volume of metal removed

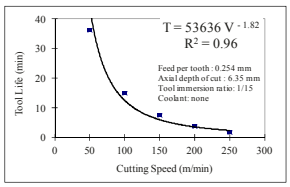

a) Effect of cutting speed

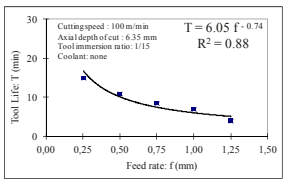

b) Effect of feed rate

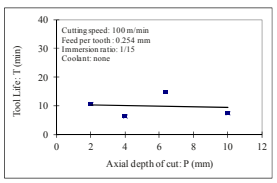

c) Effect of depth of cut

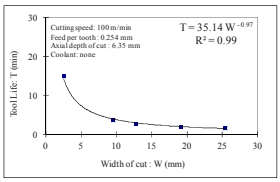

d) Effect of width of cut

Fig. 6. Tool life as function of cutting parameters (Tool life critera: 0.3 mm flank wear)

From Fig. 6, it appears that the speed, the feed rates and the width of cut have similar impact on tool life while the axial depth of cut seemed not to influence the tool life or the wear rate. It did increase the total worn area on the flank face on the tool without increasing the flank wear length. This can be explained by the fact that in side milling the increase of depth of cut plays a key role on radial load on the tool. This load impacts more in deflecting the tool than increasing the normal load, responsible for abrasion wear on the flank face of the tool. The use of higher feed, depth of cut and width of cut will increase the tool life and the tool performance since the metal removal rates will be increased and the tool will have limited contacts with abrasive particles for a given volume of material to remove.

Figure 7 shows the progression of the total metallic particle emission (PM2.5) as a function of the cutting parameters. In general, increasing the cutting speed, the depth of cut or the tool immersion led to increased amount of dust produced. A statistical analysis of the dust generation led to the modeling of the dust generation (*Dg*), Eq. 1 as a function of the cutting speed (*V*), the feed rate (*f*), the width of cut (*W*) and the depth of cut (*p*). This model
(Eq. 1) explained 89 % of the variability found in dust generation (*Dg*).

$$D_g = \frac{p^{0.645} \cdot W^{0.072}}{V^{0.107} \cdot f^{0.79}} \qquad R^2 = 89\ \% \qquad (1)$$

The product of the depth of cut and the width of cut present in the numerator of the Eq.1 describe the chip section and the surface of the chip generated at each advance of the tool. The terms on the numerator (depth of cut (p) and width of cut (W) of the Eq.1 are related to chip geometry while those in the denominator (the cutting speed (V) and the Feed rate or the feed per tooth (f)) are related to the speed at which chip is being generated
Let us define:

$C_p = d\ W$ the chip parameter. It represents the volume of chip removed per unit length of workpiece.
$S_p = f\ V$ the tool speed parameter,

From Eq. 1, it comes that the total dust emission is proportional to the chip parameter and inversely proportional to the speed parameter. A statistical analysis of the dust emission as a function of C_p and S_p has led to the two regression models that follow (Eq. 2 and 3):

$$e^{D_g} = A \times \frac{C_p^{1.31}}{S_p^{0.42}} \qquad R^2 = 83\ \% \qquad (2)$$

$$D_g = k \frac{C_p^{0.44}}{S_p^{0.182}} = k \frac{(p \cdot W)^{0.44}}{(V \cdot f)^{0.182}} \qquad R^2 = 74\ \% \qquad (3)$$

Where *Dg* (µg) is the total dust, *A* and k are constants depending on material (A = 0.307 and *k* = 0.60 for the GrA-Ni 10S 4G composite tested), C_p (mm^2) the chip parameter, S_p (mm^2/s) the speeding parameter

According to Eq. 1, 2 and 3, low depth of cut and width of cut combined with higher cutting speed and feed rates will result in very limited dust emission. This strategy is very practical as the low chip volume is combined to higher speed, thus maintaining the productivity at the same time that the dust emission is reduced. The use of high feed rate will also limit the wear of the cutting tools [5]. Higher feed rates will limit the amount of time the tool is in contact with the abrasive workpiece material.

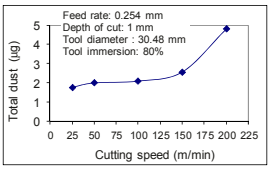

a) Effect of the cutting speed

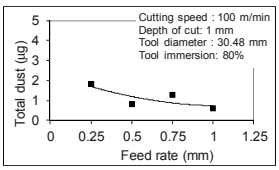

b) Effect of feed rate

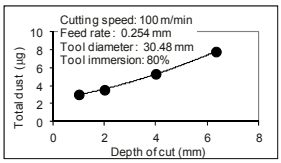

c) Effect of depth of cut

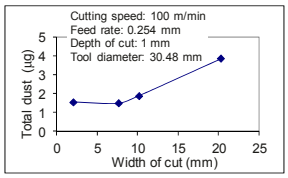

d) Effect of tool immersion (width of cut)

Fig. 7. Metallic particle emission (total dust) as function of cutting parameters

4. Conclusions

This work has shown that during the milling of graphitic SiC-reinforced aluminum matrix composite with carbide tools, the wear mechanism is pure abrasion. The wear and the tool life are determined by the speed, feed and with of cut used. The axial depth of cut does not influence the flank wear land nor the tool life. The metallic particle emission during this milling process was found to be proportional to the chip parameter (product of depth of cut and width of cut) and inversely proportional to the speed parameter (product of the feed rate and the cutting speed). Empirical models describing the relationship between the dusts produced and the cutting parameters were proposed. A strategy for reducing the dust production while maintaining the machining process productivity was recommended: use of small chip section associated with higher cutting speed and feeds. The use of higher feed rate is also favorable for the tool life as a large volume of metal will be removed before the tool wears out completely.

References

[1] Balazinski M., Songmene V. and H. Khishawi, (2011), Analyzing the machinability of metal matrix composites, in H. Hocheng: Machining Technology Composite Mat.: Principles &Practice, Woodhead Publishing Ltd, 394-411.

[2] Rohatgi, PK, Bell J.A., Stephenson T.F., Aluminium-Base Metal Matrix Composite, European Patent Ep0567284A2, Inco, April 20 & October 27, 1993.

[3] Bell J.A., Stephenson T.F., Warner A.E.M, Songmene V., 1997, Phy. Prop.of Graphitic Silicon Carbide Aluminium Metal Matrix Composites, SAE technical paper 970788.

[4] Rohatgi P.K., Narendranath C.S., 1993, Tribological Properties of Al-Si-Gr-SiC Hybrid Composite, proc. of ASM Materials Congress, Pittsburgh, Pennsylvania, 17-21, 21-25.

[5] Songmene V., Balazinski M.,1999, Machinability of Graphitic MMCs as a Function of Reinforcing Particles, Annals of CIRP, 48/1, 77-80

[6] Ames W., Alpas A.T., 1993, Sliding Wear of an Al-Si Alloy Reinforced with Silicon Carbide Particles and Graphite Flakes, proc. of ASM Mat. Congress, Pittsburgh, Pennsylvania, Oct. 17-21: 27-35.

[7] Azzi, L.; Ajersch, F., Stephenson, T.F., 2000, Rheological Characteristics of Semi-Solid GrA-Ni® Composite Alloy, 6th international conference on Semi-Solid Processing of Alloys and composites, Sept. 27-29, Turin, Italy. Pre-print

[8] Songmene V., Balazinski M., 2001, Machining of graphitic SiC aluminium MMC with Diamond Tools, Proc. 1st Int. conf. On Progress in Innovative Manufacturing Engineering, Genoa, Italy, June 20-22, 2001, 73-76.

[9] Sutherland JW, Kulur VN, N.C. King, (2000), An Experimental Investigation of Air Quality in Wet and Dry Turning. CIRP Ann, Manufacturing Technology 49(1):61-64

[10] Arumugam, P. U., Malshe, A. P., and Batzer, S. A., Bhat, D. G., (2002), Study of airborne dust emission and process performance during dry machining of aluminium-silicon alloy with PCD and CVD diamond coated tools NAMRC. Society of Manufacturing Engineers MR02-153, 1-8

[11] Khettabi R., Songmene V., Zaghbani I. and Masounave J (2010), Modeling of fine and ultrafine particle emission during orthogonal cutting, Mat. Eng. & Perf. 19, 776–789.

[12] Khettabi R., Songmene V., and Masounave J, (2010), Effects of cutting speeds, materials and tool rake angles on metallic particle emission during orthogonal cutting, Materials Engineering & Performance, 19, 767–775.

[13] Khettabi, R. Songmene, V. (2009), Particle emission during orthogonal and oblique cutting, Int. J. Advances Machining and Forming Operations, v. 1, N.1, Jan-June 2009, 1-11.

[14] Zaghbani, I., Songmene, V. and Khettabi, R., (2009), Fine and Ultra fine particle characterisation and Modeling In High Speed Milling of 6061-T6 Aluminium Alloy; Materials Eng. & Performance, Vol.18, I. 1, 38-49.

[15] Songmene V., Balout B. and Masounave J. (2008), Clean Machining: Experimental Investigation on Dust Formation, Int. J. of Environmentally Conscious Design and Manufacturing, vol. 14, N. 1, 1-33.

[16] Balout B., Songmene V. et Masounave J., (2007) An Experimental Study of Dust Generation during Dry Drilling of Pre-cooled and Pre-heated Workpiece Materials, Manuf. Processes, SME, vol. 9; No 1, 23-34.

[17] Tomac, N., Tonnessen, K.. and Rasch, F.O. 1992, Machinability of Particulate Aluminium Matrix Composites, Annals of CIRP, 41/1, 55-58.

[18] Weinert, K.; Köning, W.; 1993, A consideration of tool wear Mechanism when Machining Metal Matrix Composites (MMC), Annals of CIRP, 42/1, 95-98.

[19] Kremer, A.; El Mansori, (2009), Influence of nanostructured CVD diamond coatings on dust emission and machinability of SiC particle-reinforced metal matrix composite; Surface and Coatings Technology, 204, n 6-7, Dec. 2009, 1051-1055.

5-3

Surface integrity of Al6061-T6 drilled in wet, semi-wet and dry conditions

Y. Zedan, V. Songmene, R. Khettabi, J. Kouam and J. Masounave
Department of Mechanical Engineering, École de Technologie Supérieure (ÉTS), 1100 rue Notre-Dame West, Montréal, Québec, Canada.

Abstract. The quality of the surface dictates the functional performance and service-life of produced parts. The main objective of the present paper is to investigate the effect of different lubrication types and modes on the integrity of the surface produced during high speed drilling of 6061-T6 aluminum alloy. Surface integrity index investigated include surface roughness, dimentional accuracy, and microhardness of the subsurface of the drilled hole. Exit burr height is also investigated as a function of the lubrication modes. Results of this study revealed that, in general lubrication types and their interaction with cutting parameters have significant effects on the surface quality and integrity of the drilled holes. It is also found that dry and semi-wet also called mist lubrication machining can produce parts with surface quality comparable to that obtained in wet drilling conditions. Some loss of part mechanical properties have been observed from the microhardness analysis of the drilled holes, for all tested lubrication conditions.

Keywords: aluminum alloys, drilling, cutting fluid, Mist, dry drilling, surface integrity, burr height

1. Introduction

Aluminum alloys have been the most widely used structural materials in the aerospace and automotive industries for several decades. Currently, one of the most commonly used aluminum alloys is the 6000-series (Al-Mg-Si) [1]. This attributes to superior mechanical properties such as a high strengh/weight ratio, good corrosion resistance, weldability, and deformability. The functional behavior and dimensional stability of a finished component is greatly influenced by the surface intergrity induced during machining [2]. To improve the part surface finish and limit the tool wear, the machining process has been performed for long times using metal working fluids. The use of cutting fluid in machining however degrades the environment and increases the machining cost. Therefore, a special interest is given to dry machining since last few years [3]. Dry drilling is one of the most difficult machining processes because of difficulties associated with chip removal and the resulting high cutting temperatures [4]. To limit this elevated temperature, it is recommended to use minnimum quantity lubrication machining (MQL). This new technique consist of applying only a few millimeter of fluid in form of mist to the tool's cutting edge [5]. The cutting fluid was found to have a significant effect on thermal deformation and dimensional error [6].

Very limited studies so far, dealt with the influence of lubrication modes and its interaction with machining parametes on surface integrity of non-ferrous alloys such as drilled aluminum alloys. While studying the effect of lubrication (dry, mist and flooded lubrication) on drilling of AA1050 aluminum, Davim *et al.* [7] found no difference in hole surface texture between mist and flooded drilling.

The objective of this reserach study is to investigate the effects of lubrication and machining parameters on surface texture, dimentional accuracy, burr formation and microhardness of the subsurface of drilled holes performed on 6061-T6 aluminium alloy.

2. Experimental work

A set of experiments was performed to investigate the effect of different lubrication method in drilling of aluminum alloy 6061-T6 (95BHN). Drilling experiments were carried out on CNC high speed machining center (28000 rpm, 50 N.m) using 9.525 mm high speed steel twist drills. The machining conditions used are shown in Tables 1. and 2.

The surface roughness of holes was evaluated using Mitutoyo SJ 400 profilometer. The surface roughness was taken at four locations (90^o apart) and repated twice at each point on the face of the machined surface. The sample from last holes drilled for each condition was sectioned in parallel to feed direction. These samples were ultrasonically cleaned in ethanol bath in order to investigate the surface texture of drilled hole using SEM for each case. The hole diameter dimension was measured in order to appreciate the component accuracy using Coordinate Measuring Machine CMM.

Table1. Lubrication modes

Type of Machining	Quantity and description of lubricant
Dry	0 m/h
Mist	Delivery pressure is 6 bar gauge; flow rate is 50 ml/h. The lubricant was a vegetable oil
Wet	Water miscible mineral oil at concentration of 5% ; flow rate of 5000 ml/h

Table 2. Machining parameters

Parameters	Condition
Material	6061-T6 (200 mm x40 mm x3 mm)
Tool	HSS twist drill-9.525 mm diameter , 118° point angle
Speed	30, 60, 120, 180, 240 , 300 m/min
Feed	0.15, 0.25, 0.35 mm/rev
Depth of cut	3 mm

The burr height was obtained using Mitutoyo Height Gauges with a sensitivity of 0.0005 in (13 µm). To measure the burr height, the gauge indictor was first placed on the datum surface at the hole exit, and then move on the top of the burr. The distance between the two measurements was thus the burr height. The measurements were done four times and then the average value was used for analysis. The burr form was also captured using optical microscopy.

Microhardness measurements of the workpiece and chip were undertaken with a Vickers indenter (Digital Microhardness Tester, FM-1) using a load of 50 g and a loading time of 10 s. Ten indentation loads were carried out on the middle of the sample to obtain the baseline value of the bulk microhardness. A series of five readings were taken at equispaced distances in the direction normal to the hole surface, and to depth aproximely 350 µm below the surface, as shown in Figs. 1.a, b and c.

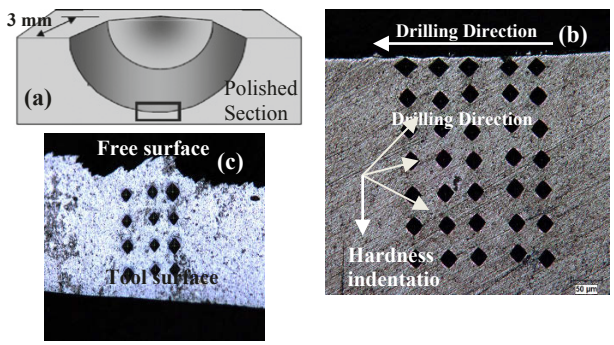

Fig. 1. (a) Schematic diagram of the quarter section of drilled hole showing the plan which is the mid-section of the hole parallel to the workpiece; (b) an optical micrograph of this section with the Vickers indentation impressions; and (c) optical micrograph showing microhardness variations beneath the chip produced.

3. Results and discussions

Fig. 2 (a) represents the vartions in the microhardness as function of depth below the ground surface. The results obtained from microhardness measurement of Al6061-T6 in dry, mist and wet application did not indicate significant sub-surface modification. Microhadness variation is gradually increasing with increase depth below the machined surface. This figure exhibts also an increasing in the micro hardness values ranging from 15-20 $HV_{0.05}$ confining to depth of cut around 50 µm from the machined surface before the reaching its stable bulk microharness values. This could be due to the fact that, depending upon the temperature of cutting process, annealing of the work-piece may occur during machining, causing softenting close to the finished surface.

Fig. 2 (b) compares the average microhardness value of the produced chips with diffirent lubrication mode at the same cutting conditions. For both the dry and mist cutting, the microhardness measurments show higher values compatred to wet application. This result is mostly likely due to the higher cutting temperature induced into produced the chips during dry and mist applications. This in turn leads to higher flow stress resulting in an increase in surface deformation that ultimately led to an increase in the work hardening of the produced chips dominated by plastic deformation.

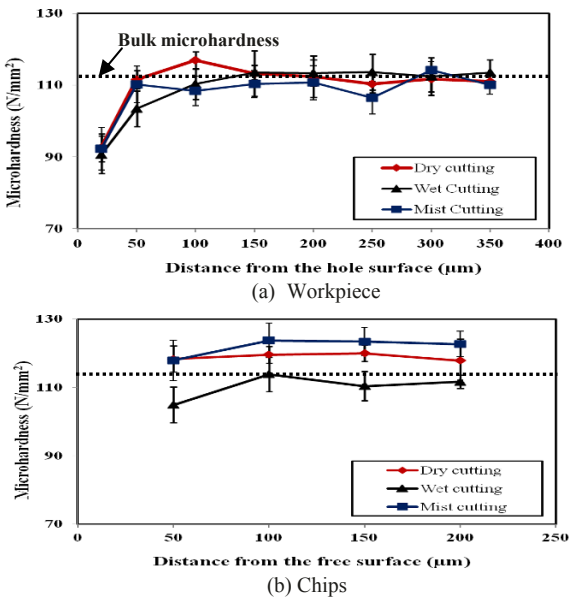

Fig. 2. a. Microhardness variations beneath the surface produced for dry, mist and wet conditions; (b) Microhardness variations beneath the chip produced for various lubrication. Machining condition: cutting speed = 120 m/min, feed rate 0.25 mm/rev). The dashed line indicates the average bulk hardness.

Cutting fluid application was found to have an effect on the average diameter of holes drilled with different cutting speeds and feed rates. Fig. 3 (a) shows the effect of the feed rate on the mean diameter with different cutting speeds during wet drilling. It was observed that

the mean diameter decreases with increased feed rates. This observation is more pronounced at high cutting speeds (300 m/min), however the effect of feed rate on the mean diameter is insignificant with the low cutting speed i.e. 60 m/min. Fig.3 (b) presents a comparison of mean diameter values obtained against cutting speed with various cutting fluid application methods. It was found that the wet condition exhibits a high increase in mean diameter compared to mist and dry applications. One explanation of the larger mean diameter seen with the cutting fluid [Fig.3(b)] may be attributed to the thermal expansion and heat-removal properties of the cutting fluid. This would suggest that, without cutting fluids, enough heat is retained in the workpiece to allow expansion to occur. After machining, the workpiece cooled down, and the diameters of the holes become smaller in comparison to the holes drilled with cutting fluids [8]. The effect of drill temperature can be ignored because of the depth of cut used in this study is very small about 3 mm and the time the drill was in contact of the material very limited.

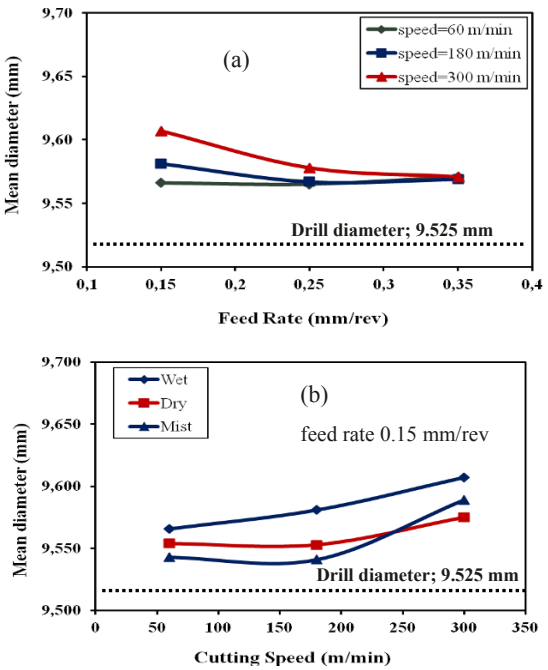

Fig.3. a. Showing the effect of feed rate on the mean diameter; (b) comparison of average values of machined hole diameters obtained with wet, dry and mist lubrication versus cutting speed

Fig. 4 shows SEM photographs of typical sectioned drilled hole surface and corresponding surface for three drilling conditions with the same cutting speed (120 m/min) and feed rate (0.25 mm/rev). As shown clearly, the dry and mist drilled holes exhibit a smoother surface while the wet conditions produce heavily deformed zones on the side-wall with significant feed marks resulting in increased roughness. The surface roughness measurements show that the Ra values of holes drilled in the wet condition are almost one-and-half times higher than those drilled with mist and dry conditions. The adverse surface effects found with wet drilling applications may be explained by the following phenomena: post-cut (drill removal) occurrences, being which chips dragged against the side wall of the hole as the drill is being retracted, this phenomene was alerady observed by [4]. The severity of this effect was high with the external pressurized cutting fluid application. The denoting that external high pressure fluid application might have trapped the chip within the tdrill flute.

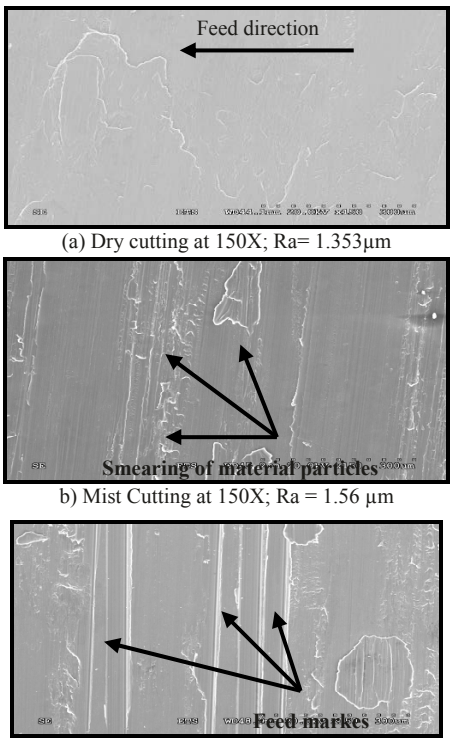

(a) Dry cutting at 150X; Ra= 1.353µm

b) Mist Cutting at 150X; Ra = 1.56 µm

(c) Wet Cutting at 150X; Ra = 2.36 µm

Fig. 4. SEM of surface texture was observed on the holes drilled with various methods of cutting fluid application with the same cutting speed and feed rate.

Burrs generated during machining may cause part reliability problems and deterioated the performance. Fig. 5 show the two burr types created on the exit surface of the drilled holes under dry, mist and wet lubrication modes. Two types of burr form namely the transient and the uniform burrs were observed. The transient type was created for dry condition with low cutting speed and feed rate [Fig. 5(a)]. The uniforms burr with a uniform height and thickness was found to form at low cutting speed and feed rate for wet and mist lubrication modes [Figs. 5 (b) and (c)]. The most common burr type observed in this study was the uniform burr.

Fig. 6 exhibits that the burr height decreases significantly with increase in feed rate. In addition lubrication conditions have shown a great influence on drilling burr size. This is due to the intense effect of

cutting fluid on temperature reduction in cutting zone area which greatly facilitate the cutting process and chip evacuation in drilling process; therefore less burr height was expected by using wet cutting condition. Fig. 5 proves also that at lower cutting speed, lubricated machining application (mist and wet) produces smaller-size burrs compared to dry machining; however the burr height is not influenced under various cutting fluid applications at high cutting speed as shown in Fig. 6 (b).

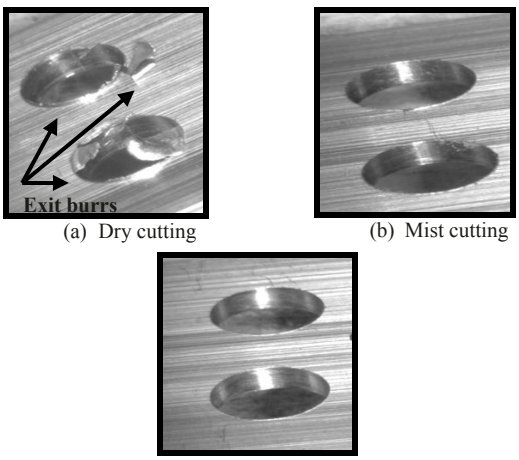

(a) Dry cutting (b) Mist cutting

(c) Wet cutting

Fig. 5. Optical microscopy image showing typical burr formation for 6061-T6 for various cutting fluid applications

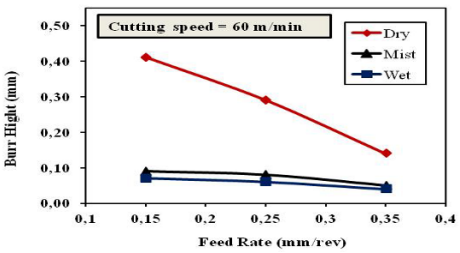

(a)

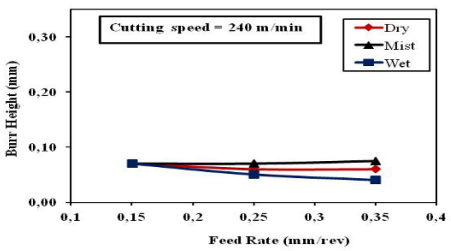

(b)

Fig. 6. A comparison of average values of burr height obtained with wet, dry and mist lubrication versus feed rate at differen cutting speed

4. Conclusions

The effects of lubrication modes on machining performance were investigated. It was found that with a proper selection of cutting parameters, mist and dry drilling can led to advantageous performances in terms of hole surface finish and burr height, compared to wet drilling. More specifically, it can be concluded that:The results obtained from microhardness measurements indicate a loss in hardness values from 110 to 90 $HV_{0.05}$ at 20 µm beneath the surface produced for dry, mist, and wet conditions. The cutting fluid applications has an effect on the average diameter of the drilled hole, The wet condition produces an increase in mean diameter as compared to mist and dry applications. Dry and mist drilled holes exhibit smoother surfaces while wet conditions produce heavily deformed zones on the side wall, with feed marks resulting in increased roughness. The burr height decreased significantly with an increase in the cutting speed and feed rate, independently of the various methods of cutting fluid applications. However, at lower cutting speeds, lubricated machining applications (mist and wet) produced smaller size burrs as compared to dry machining.

References

[1] Lee SH, Saito Y, Sakai T, Utsunomiya H, (2002) Microstructures and mechanical properties of 6061 aluminum alloys processed by accumulative roll-bonding. Materials science and engineering A 325: 228-235

[2] Toh CK, Kanno S, (2004) Surface integrity effects on turned 6061 and 6061-T6 aluminum alloys. J. Materials Science 39:3497-3500

[3] Dasch, JM, Ang, CC, Wong, CA, Cheng, YT, Weiner, AM, Lev, LC, Konca, E (2006) A comparison of five categories of carbon-based tool coatings for dry drilling of aluminum. Surface & coatings technology 200: 2970-2977

[4] Kalidas S, DeVor RE, Kapoor SG (2001) Experimental investigation of the effect of drill coatings on hole quality under dry and wet drilling conditions. Surface & coatings technology. 148:117-128.

[5] Weinert K, Inasaki I, Sutherland JW, Wakabayashi T. (2004) Dry machining and minimum quantity lubrication. CIRP Annals-Manufacturing Technology. 53: 511-537

[6] Lopez de Lacalle LN, Lamikiz A, Sanchez, JA, Cabanes I (2001) Cutting conditions and tool optimization in high speed milling of aluminum alloys. Proceedings of the Institution of Mechanical Engineers, Part B: Journal of engineering manufacture. 215: 1257-1269

[7] Davim, JP, Sreejith, PS, Gomes, R, Peixoto C (2006) Experimental studies on drilling of aluminum (AA1050) under dry, minimum quantity of lubricant, and flood-lubricated conditions. Proceedings of the institution of mechanical engineers, Part B: J.Eng. Manuf. 220: 1605-1611

[8] Haan DM, Batzer SA, Olson WW, Sutherland JW (1997) An experimental study of cutting fluid effects in drilling. Materials processing technology. 71: 305-313.

5-4

Dry machining of aluminum alloys and air quality

A. Djebara and V. Songmene
Products, Processes, and Systems Engineering Laboratory (P_2SEL), Department of mechanical Engineering
Ecole de technologie Supérieure, ÉTS, 1100 Notre-Dame West, Montréal (Qc), Canada.

Abstract. Most manufacturing and especially metal working activities generate aerosols (dry or wet) that can be harmful or degrade the environment due to the use of new processes and advanced materials such as materials containing nanoparticles. Dry machining is an environmentally conscious process, but under certain conditions, it can produce significant quantities of metallic particles. A new problem appears concerning the risk related to the exposure to metallic particles dispersed in air. To limit the metallic particles generation, it is essential to know under what conditions they are formed as well as the mechanisms underlying their formation. The main objective of this study was to evaluate the impact of machining conditions on metallic particles emission during dry machining. This work was carried out in order to minimize dust emission and thus preserve the environment and improve air quality in machine shops. Microscopy observations of particles produced during dry machining show that there are a great heterogeneity in the particles shape and a large dispersion for the size (a few nanometers to a micrometer). It is also found that during high speed machining, the emission of metallic particles decreases with the increase of cutting speed. This result is very encouraging from a practical standpoint. It is thus possible to machine parts at very high speeds, which ensures high productivity, good quality parts and limited metallic particles emission.

Keywords: Dry machining, aluminium alloys, ultrafine particles, fine particles.

1. Introduction

Indoor air quality is an emergent issue, directly related to worker exposure to polluted indoor air [1]. Machining occupies a privileged place in the shaping process because of its necessity and its large application domain, but it also represents a potential danger to health and the environment due to the aerosol generated. These aerosols may be liquid (from cutting fluids) or solid (metal particles emitted during cutting). The subject has gained a lot of interest in scientific and governmental circles in the last decade [2, 3] because of high risk associated with exposure metallic particle.

It is accepted that exposure to fine or ultrafine metallic particles can be responsible for diseases ranging from simple irritation of the lung airways to cancers [3]. Some countries have set regulations and standards for dust emission in workplace. In Germany for example, the new limit value is 0.3 mg/m^3 for respirable dust [4]. The National Institute for Occupational Safety and Health (NIOSH) recommended exposure limits of 1.5 mg/m^3 for fine particles and 0.1 mg/m^3 for ultrafine particles [5]. Air quality control in the industrial environment is usually carried out by sampling particulate matter smaller than 2.5µm ($PM_{2.5}$) or by gas receptors, in situations where the main polluters are gases [6]. If the liquid aerosols can be reduced by eliminating the use of cutting fluid, it remains solid particles emitted during metal cutting. For example, aluminum, titanium and composite materials used in aerospace can decompose into dangerous and explosive dust [7].

Djebara et al. (2010) show that the metallic particles produced when milling at high speed have different shapes [8, 9]. Kouam et al. (2011) found that friction produces more ultrafine particles than fine particles [10]. Various research studies have been conducted to identify the major factors influencing exposure to metalworking aerosols [1, 6, 8, 11-13]. A committee of risk prevention and control of the working environment of the World Health Organization held in Switzerland in 1999 wished there be research relating to the dust production process parameters, which would help assess the reliability and cost of changing systems to improve control of dust [14].

The experimental setup used in this work, the sampling method and the analyses proposed address some of those challenge. The main objective of this study is to show the effects of machining processes parameters, workpiece materials and tooling on metallic particle emission during a slot milling process. Such knowledge is needed by design and process engineers in selecting appropriate ventilation systems and controlling strategies to minimize exposure to indoor metallic particles. Only dry machining is considered because of its beneficial effects on environment and machining costs.

2. Experimental procedure

The experiments were performed on CNC milling center (Power: 50kW, Speed: 28000 rpm Torque: 50 Nm). Fine

and ultrafine particles size were measured using Scanning Mobility Particle Sizer (SMPS). The experimental setup used is presented in Fig.1.

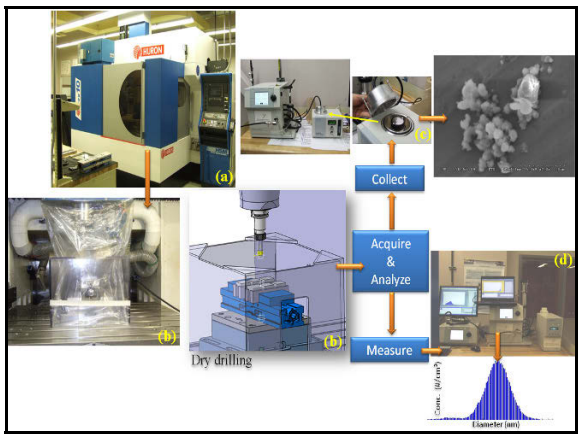

Fig. 1 Experimental setup

The workpiece materials used and their mechanical properties are presented in Table 1. The machining tests were based on a multi-level full factorial design (DOE), Table 2. The cutting tool used was a 19 mm diameter three flutes end mill cutter. The inserts has the following characteristics:

IC328: 0.5 mm nose radius, TiCN coating
IC928: 0.83 mm nose radius, TiAlN coating
IC4050: 0.5mm nose radius, TiCN/Al_2O_3/TiN coating

Table 1 Mechanical properties of the three aluminium alloys

Material	Brinell - Hardness	Yield Strength
Al 6061-T6	95 HB	275 MPa
Al 2024-T351	120 HB	325 MPa
Al 7075-T6	150 HB	505 MPa

Table 2 Factors and levels used in DOE

Factors	min	midle	max
Cutting speed (m/min)	300	750	1200
Feed rate (mm/rev)	0.03	0.165	0.3
Depth of cut (mm)	1	-	2
Workpiece materials	6061-T6	2024-T351	7075-T6
Tools (inserts)	IC328	IC908	IC4050
Cutting fluid	None		

3. Results and Discussions

3.1. Typical machining particle generation: direction, morphology and size distribution

Prior to performing the machining tests, a preliminary test was performed using an ice block to determine the direction taken by the generated aerosol. When machining a long and deep slot (Fig.2) most of the dust produced is ejected from the slot machined in the opposite direction of the feed rate. Therefore the appropriate location of the dust or metallic particle sampling is at the back side, opposed to tool path direction.

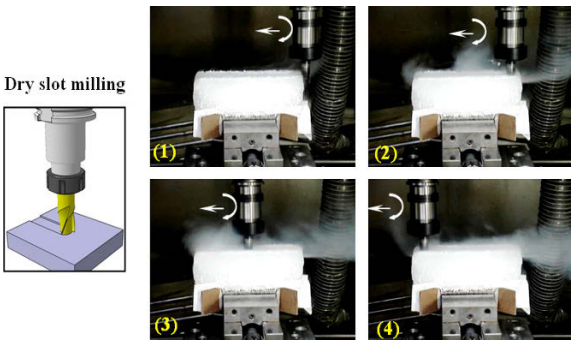

Fig. 2. Direction taken by the particles emitted during milling process: (750 m/min, 0.165 mm/rev, 19 mm tool diameter)

An analysis of the chip obtained during the machining process gives an indication on one of the possible mechanism of metallic particle generation (Fig. 3). The formation of particles during the machining is caused by different phenomena such as: macroscopic and microscopic friction, plastic deformation and chip formation mode. The friction of the chip micro-segments between themselves produces particles of micrometric and nanometric in size. Similarly, the friction at the tool rake face with the chip also produces particles. The outer surface irregularity of the chip observed (Fig. 3) shows that the separation degree between the segments coincides with the particles generation for each material. These results reflect the high segmentation number and the spacing between them generated much metallic particle. It is likely that much particle emission comes from this area.

Figure 4 shows typical particle emission results as a function of the particle diameters obtained using SMPS. All the distribution curves obtained have the same profiles (Fig.4). Table 3 summarizes the distribution of metallic particles as a function of three selected intervals. After collecting the ultrafine particles with the NAS (Nanometer Aerosol Sampler), observations with transmission electron microscope and scanning electron microscope showed ultrafine particles to be heterogeneous (Fig.5) and agglomerate (Fig.6).

This morphology depends on the nature of the material and the mechanism that produced it. Similarly, the agglomeration of ultrafine particles does not lead to spherical particles (Fig.6).

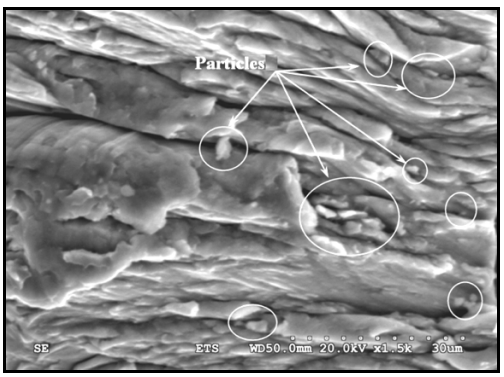

Fig. 3. SEM image of chip

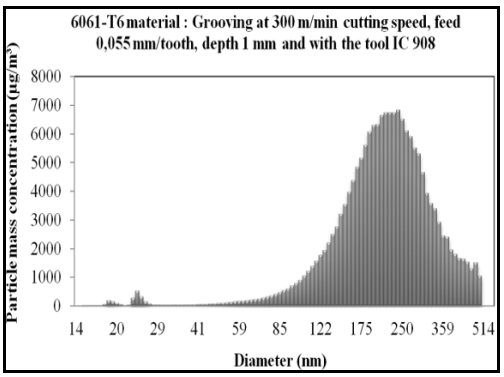

Fig. 4. Mass concentration from SMPS of 6061-T6 at cutting speed 300 m/min, feed 0,165 mm/rev

Table 3 Particle number fraction distribution

Diameters range	Percentage of total particle
Φ between 0.1 and 0.5 µm	15% of total particles generated
Φ between 0.02 and 0.1 µm	20 % of total particles generated
Φ < 0.02 µm	65 % of total particles generated

While the equivalent sphere concept used to represent particles is widely used, in some cases, it is however too simplistic. For particles with irregular shapes, it is necessary to refine the size and description in order to characterize the particle, rather than using a single parameter. This characterization should be done by attaching additional parameters that attempt to quantify the extent to which the studied particle moves away from the sphere model [11].

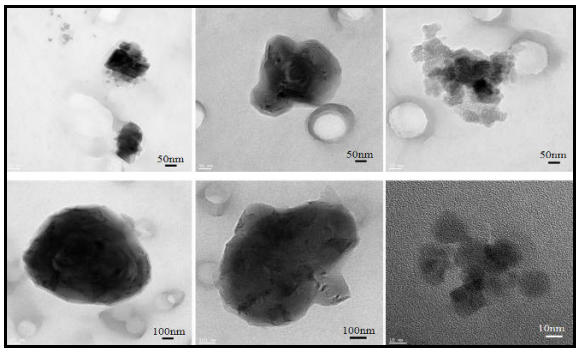

Fig. 5. TEM images of particles emitted during machining of aluminum alloy 6061-T6

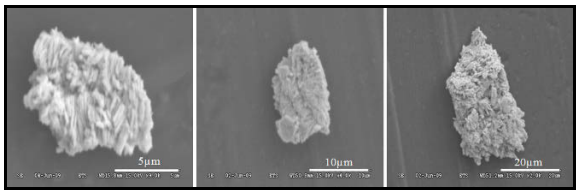

Fig. 6. SEM image of particles emitted during machining of aluminum alloy 6061-T6

3.2. Statistical analysis of effects of process parameters, tooling and workpiece materials on particle emission

A series of tests was conducted to analyze the contributions of the milling process parameters (speed, feed and depth cut), workpiece materials and cutting tool (geometry and coating) on particle emission during a. dry slot milling process. A multi-level full factorial design was used in this study (Table 2). The total number of experiments performed was 162 tests.

The diagram of direct effects (Fig.7) of the total particles mass generated highlight the important factors, namely, the material and the tool. The 7075-T6 material generates less particles than the material 2024-T351 in the same cutting conditions. Reducing the tool nose radius decreases the dust emission. Factors such as depth, cutting speed and feed rate had small influences.

The Pareto diagram (Fig.8) compares the relative importance and statistical significance of main factors and interaction effects between factors. The reference line in the Pareto chart indicates the statistically significance level at a confidence level of 95%. The Pareto diagram shows the predominance of the material factor for the response mass concentration. The material and tool alone explain more than 90% of the variation found in the response. The contributions of feed rate and cutting speed are very small and not significative. Therefore, the tool and the workpiece material factors appear as those

controlling the reduction in particle emission for the studied process and conditions.

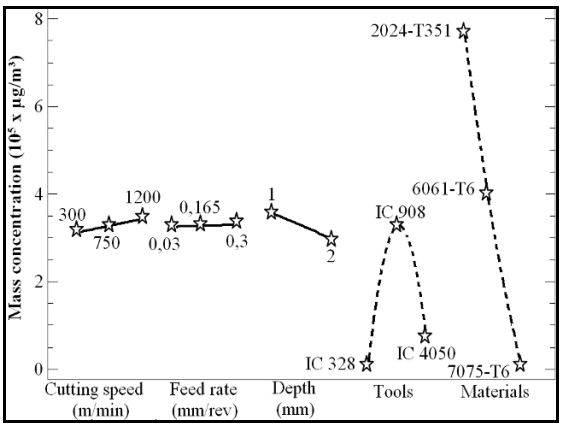

Fig. 7. Direct factors effects for the particles generation

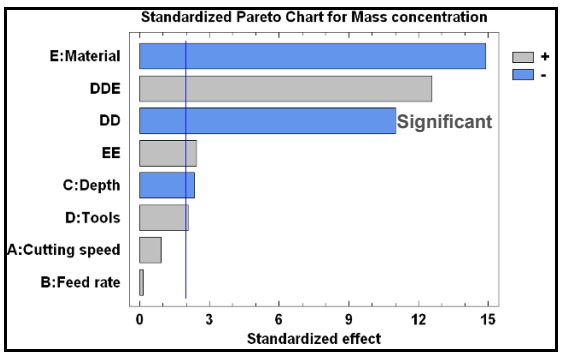

Fig. 8. Pareto diagram of mass concentration

Figure 9 presents the comparison results of the total mass concentration obtained during dry slot milling tests for 6061-T6 and 7075-T6. For 6061-T6, the particles emission are higher compared to 7075-T6 material at low cutting speed (< 400 m/min), but at high speed the particles emission are higher for 7075-T6 material. This observation can be explained by the 7075-T6 hardness is higher than the 6061-T6 one. On the other hand, their mechanical properties as well as their hardness (150 HRB for 7075-T6 and 95 HRB for 6061-T6) could have played an important role.

The response surfaces (Fig.10) embody the change in the dust generation as a function of cutting speed and feed rate. Figure 10 (c) shows that the airborne swarf of the aluminum alloy 7075-T6 is uniform across the cutting speed and feed ranges selected. Conversely, for aluminum alloy 2024-T351, there is a wide variation. Eventually, the response surface identified a region of the experimental field in which the dust emission is maximal (to be avoided). This maximum is given by the combination of a critical cutting speed and feed rate. For the 6061-T6 material, the experimental field in which the ultrafine particles emission is maximal to correspond to a feed rate less than 0.06mm/rev at low cutting speed or to a feed rate less than 0.03mm/rev when using a high cutting speed.

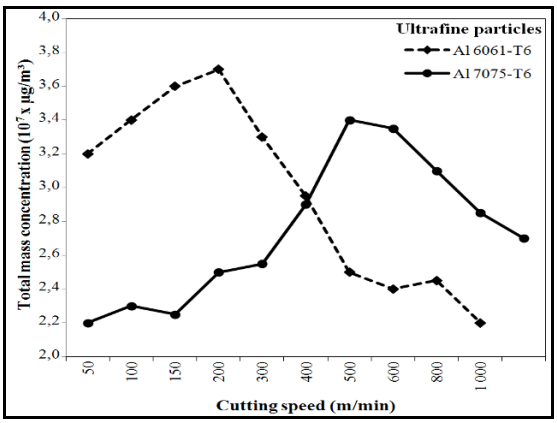

Fig. 9. Total mass concentration at different speeds obtained from SMPS at 0,165 mm/rev of feed and indexable inserts IC908

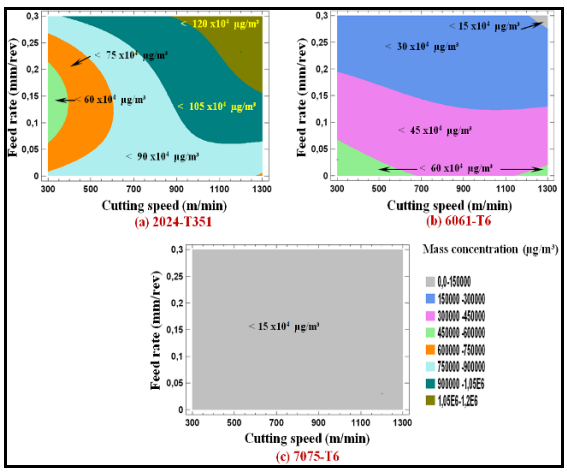

Fig. 10. Contours of estimated response surface for the mass concentration

4. Conclusion

In this work it was shown that dust emission in machining is affected by the combination of material and tool geometry. Statistical analysis has shown for a full slot milling of wrought aluminum alloys, the particle emission is controlled by the cutting tool geometry and coating, and the workpiece material rather than the cutting parameters. Using special tool geometry during dry cutting, the machining can be advantageous and sustainable. The results also confirm the existence of ranges cutting speed and feed rate to what the dust emissions is minimal.

This examination indicates that is possible to machine parts at very high speeds, which ensures high productivity, good quality parts, and without producing harmful metallic particles. Implementing this should

represent a very great step in industry because manufacturers could become more productive and more competitive without compromising workers' health.

References

[1] Sutherland JW, Kulur VN, N.C. King, (2000) An Experimental Investigation of Air Quality in Wet and Dry Turning. CIRP Annals Manufact. Technology 49(1):61-64

[2] EPA US, (1995) Characterizing Air Emissions from Indoor Sources. U.S. Environmental Protection Agency, Washington, DC. EPA 600/F-95/005

[3] Ostiguy C, Roberge B, Ménard L, Endo C, (2009) A good practice guide for safe work with nanoparticles: The Quebec approach. IOP Publishing 012037

[4] Aronson RB, (1995) Why dry cutting? Manufacturing Engineering 2(1):33–36

[5] Sreejith PS and Ngoi BKA, (2000) Dry machining, machining of the future. Journal of Materials Processing Technology 101:287–291

[6] Arumugam, P. U., Malshe, A. P., and Batzer, S. A., Bhat, D. G., (2002) Study of airborne dust emission and process performance during dry machining of aluminum-silicon alloy with PCD and CVD diamond coated tools NAMRC. Society of Manufacturing Engineers MR02-153, 1-8

[7] Agrawal JP, Hodgson RD, and Corporation E, (2007) Organic chemistry of explosives: Wiley Online Library

[8] Djebara A, Songmene V, al. e, (2010) Experimental investigation on ultrafine particles emission during dry machining using statistical tools. Proceedings of the International Conference on Nanotechnology: Fundamentals and Applications 490(1):1-10

[9] Djebara A, Khettabi R, Kouam J and Songmene V, (2011) Comparison of the Capability of Peak Function in Describing Real Condensation Particle Counter Profiles. Advanced Materials Research 227:96-100

[10] Kouam J, Songmene V, Djebara A, Khettabi R (2011) Effect of Friction Testing of Metals on Particle Emission. Journal of Materials Engineering and Performance:1-8

[11] Djebara, A., (2011), Métrologie des particules ultrafines d'usinage : optimisation de la caractérisation et de la mesure, Ph.D thesis, École de technologie supérieure, ÉTS, Montréal, Canada, 200 pages (In french).

[12] Songmene, V., Balout, B., Masounave, J. (2008), Clean machining : Experimental investigation on dust formation, International Journal of Environmentally Conscious Design & Manufacturing 14(1): 1-34

[13] Khettabi, R., Songmene, V., Masounave, J. (2010). Effects of Speeds, Materials, and Tool Rake Angles on Metallic Particle Emission During Orthogonal Cutting, Journal of Materials Engineering and Performance 19 (6): 767-775

[14] WHO (1999). Global Air Quality Guidelines. Geneva. WHO.

5-5

Study on hybrid magnetic force assistant abrasive flow machining process

Ramandeep Singh and R.S. Walia
PEC University of Technology, Chandigarh, India

Abstract: Abrasive flow machining is a non-conventional machining process and was developed in late 1960's as a method to deburr, polish and radius difficult to reach surfaces such as intricate geometries by flowing a semi-liquid paste over them. Abrasion occurs wherever the medium passes through the highly restrictive passage. The key components of AFM process are the machine, tooling and abrasive medium. The AFM is capable of economically producing high surface finish. One serious limitation of this process is its low productivity in terms of rate of improvement in surface roughness. Till now limited efforts have been done towards enhancing the productivity of this process with regard to better quality of work piece surface. In recent years, hybrid-machining processes have been developed to improve the efficiency of such processes. This paper discusses magnetic force as a technique for productivity enhancement in terms of percentage improvement in surface roughness (Ra) and material removal (MR). The magnetic force is generate around the full length of the cylindrical work piece by applying DC current to the solenoid, which provides the magnetic force to the abrasive particles normal to the axis of work piece. The result shows that magnetic force assisted AFM gives better results in terms of material Removal and percentage improvement in surface roughness compared to conventional AFM..

Keywords: Abrasive Flow Machining (AFM), Magnetic Force, MFAAFM. MAFM

1. Introduction

Abrasive flow machining (AFM) is one of the latest non-conventional finishing processes, which possesses excellent capabilities for finish-machining of inaccessible regions of a component. It has been successfully employed for deburring, radiusing, and removing recast layers of precision components by extruding an abrasive laden polymer medium with very special rheological properties. High levels of surface finish and sufficiently close tolerances have been achieved for a wide range of components [6]. The polymer abrasive medium which is used in this process possesses easy flowability, better self deformability and fine abrading capability. A special fixture is generally required to create restrictive passage or to direct the medium to the desired locations in the workpiece.

The basic principle behind AFM process is to use a large number of random cutting edges with indefinite orientation and geometry for effective removal of material. The extremely thin chips produced in abrasive flow machining allow better surface finish upto 50nm, close tolerances in the range ± 0.5μm, and generation of more intricate surface [2]. In this process tooling plays very important role in finishing of material.

In order to cater to the requirement of high-accuracy and high-efficiency finishing of materials, AFM is gaining importance day by day. The AFM process has a limitation too, with regard to achieving required surface finish. With the aim to overcome the difficulty of longer cycle time, the present paper reports the findings of a hybrid process, which permits AFM to be carried out with additional centrifugal force applied onto the cutting media.

The elements required for AFM process are the machine, workpiece fixture (tooling) and media. The machine used in AFM process hydraulically clamps the work-holding fixtures between two vertically opposed media cylinder. These cylinders extrude the media back and forth through the workpiece(s).Two cylinder strokes, one from the lower cylinder and one from the upper cylinder, make up one process cycle. Both semiautomatic machines and high-production fully automated system are widely used. The extrusion pressure is controlled between 7-200bars, as well as the displacement per stroke and the number of reciprocating cycles are controlled. AFM process is an efficient method of the inner surface finishing process. Generally speaking, the control parameters of the AFM process are extrusion pressure, media flow volume, number of working cycle etc. The result of the surface quality will be harmfully affected if improperly control the parameters in the process. It is necessary that an engineer must work on accumulating experience of the test results and does his/her best to understand the control parameters of the process such as engaging in the parameter experiment of the AFM process in order to identify the dominant factors, supporting the on-sight operation as consultant, promoting the efficiency of manufacture process and reducing the variables.

A number of studies [3, 5, 7, 8, 9, 10, 12, 13, 14] show that the material removal rapidly increases during the

initial cycles and there after it stabilized at higher number of cycles. This is due to the fact that higher peaks are removed during the initial process cycles when abrasive particles abrade these peaks; later the peaks become somewhat flatter and the rate of material removal and that of ΔRa reduce. Increased extrusion pressure, with all other parameters remaining constant, has significantly affected the work surface roughness [3,4,11]. Jain and Jain [9] reported that at higher pressure the improvement in material removal just tends to stabilize probably due to localized rolling of abrasion particles. The media flow rate has been reported to be a less-influential parameter in respect to material removal [2]. It has also been observed that greater the reduction ratio the more is the material removal from the work piece for a specified number of cycles. It has been noted that the fine grain size of the abrasive particles results in greater improvement of surface finish and the material removal decreases. The reason for this seems obvious as the fine grains are expected to make finer but large number of cuts on the high spots on the work surface, thus generating smoother surface. There exists the possibility of using a large range of concentration of abrasive particles in carrier media (2–12 times the weight of carrier media) [14]. However, it has also been suggested that abrasive grain to base material ratio (by weight) should vary from 4:1 to 1:4 with 1:1 as the most appropriate ratio [1]. The media viscosity and geometrical shape of the work piece also affect the flow pattern.

2. Magnetic Force Assisted Abrasive Flow Machining (MFAAFM)

The fixture employed for the MFAAFM process is shown in Fig. 1. In the current investigation the work piece was placed in between the media cylinders to create an artificial dead zone and increase the pressure required for extruding the media. The fixture was made in three parts. The work piece and the attachment were placed in central part. During the operation, the media containing the abrasive particles was made to flow from one cylinder to the other cylinder through the central hole in the work piece. The work piece was surrounded by an attachment specially designed to give necessary magnetic force through the whole length of the work piece resulting in pulling of the abrasive particles on the internal surface (normal to the axis) of the work piece. Thus the media was subjected to the extrusion pressure as well as to the additional magnetic force.

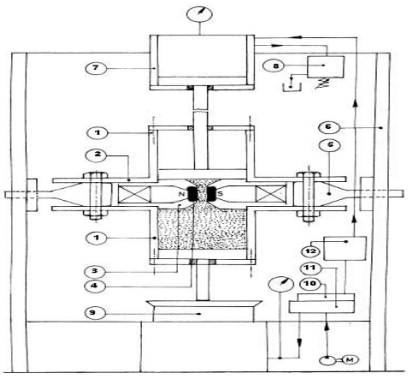

Fig. 1. Schematic illustration of the MFAAFM setup: 1 Cylinder Containing Medim; 2 Flange; 3 Nylon Fixture; 4 Workpiece; 5 Eye Bolt; 6 Hydraulic Press; 7 Auxiliary Cylinder; 8 Modular Relief Valve; 9 Piston of Hydraulic Press; 10 Directional Control Valve; 11 & 12 Manifold Blocks; 13 Electromagnet.

2.1. The Electromagnet

The electromagnet was designed and fabricated for its location around the cylindrical work-piece. It consists of two poles that are surrounded by coils arranged in such a manner as to provide the maximum magnetic field near the entire internal surface of the work-piece.

2.2. Media

Media used for present investigation consists of silicon based polymer, hydrocarbon gel and abrasive and iron particles. A Polymer-to-Gel (PGR) 1:1 has been taken. Abrasives-to-media ratio is also one. The abrasive was of Aluminium Oxide and Iron Powder, both of grit size 200, in a ratio of 3:2 have been used.

2.3. Work-piece

In the present investigation, brass as work-piece material was used. The cavity to be machined in the test specimen was prepared by drilling operation followed by boring to the required size. The test work piece is shown in Fig. 2. The internal cylindrical surface was finished by AFM process. Each work-piece was machined for a predetermined number of cycles. The work-piece was taken out from the setup and cleaned with acetone before the subsequent measurement.

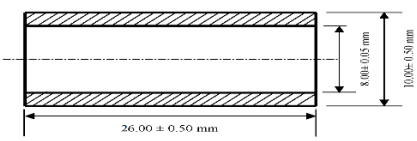

Fig. 2. Test Piece

The selected parameters and their range for the detailed experiments are shown in Table 1.

Table 1. Selected Process Parameters and their Range.

S. N.	Process Parameter	Range	Unit
1	Magnetic Flux	0.2-0.7	Tesla
2	Extrusion Pressure	5	N/mm2
3	Number of cycles	4	No.
4	Abrasive particle size	60-65	Micron
5	Media Flow Volume	290	cm3
6	Abrasive to media concentration	1:1	% by weight
7	Polymer-to-Gel Ratio	1:1	% by weight
8	Aluminium Oxide - to- Iron Powder	3:2	% by weight
9	Temperature of media	32 ± 2	°C
10	Reduction Ratio	0.90	---
11	Initial Surface Roughness	0.6-1.1	µm

3. Scheme of experiments

The magnetic flux density was selected as independent variable keeping the other parameters constant as described in table-1 and eight experiments were conducted. MR and percentage improvement in surface roughness value (ΔRa) were taken as the response parameter. The experimental specimens were chosen from a large set of specimens in such a way that selected specimens had inherent variation in their initial surface roughness values in a narrow range. It was not possible to remove this variability completely; therefore percentage improvement in surface roughness (ΔRa) has been taken as the response parameter.

4. Results and discussion

Eight experiments were conducted with magnetic flux as only variable. Figs. 3 and 4 show the simultaneous effect of magnetic flux density on MR and ΔRa respectively. From these figures it can be observed that material removal and percentage improvement in surface roughness both increase with the increase in applied magnetic flux density. The effect of magnetic field is typically more prominent beyond a magnetic flux density of 0.2T. The simultaneous increase in MR and ΔRa indicates a unique behaviour of AFM when compared with other machining processes. In AFM, the material removal takes place first from hills or peaks of the surface profile. More material removal produces a smoother surface. This holds good until all of the high hills are removed and quite a smooth surface is produced. It is also clear from the trend of the surface obtained in Figs.3 and 4 which indicates that whereas the ΔRa to improve continues with increase in magnetic field, material removal appears to start stabilising at higher densities of magnetic field. When a strong magnetic field is applied around the workpiece, the flowing abrasive particles experience a sideways pull that causes a deflection in their path of movement to get them to impinge on to the work surface with a small angle, thereby resulting in microchipping of the surface. The particles that otherwise would have passed without striking the surface now change their path and take an active part in the abrasion process, thus causing an enhancement in material removal. It is to be mentioned here that although the mechanical pull generated by the magnetic field is small, it is sufficient to deflect the abrasive particles, which are already moving at considerable speed. Therefore it appears that, by virtue of the application of the magnetic field, more abrasive particles strike the surface. Simultaneously, some of them impinge on the surface at small angles, resulting in an increased amount of cutting wear and thereby giving rise to an overall enhancement of material removal rate.

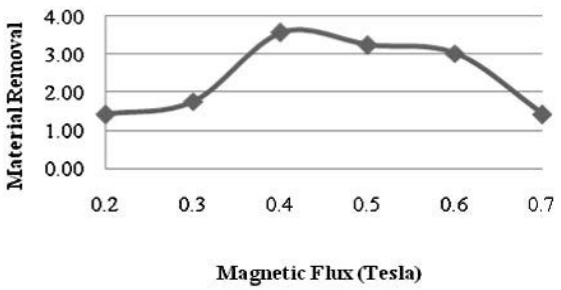

Fig. 3. Effect of magnetic flux density on MR

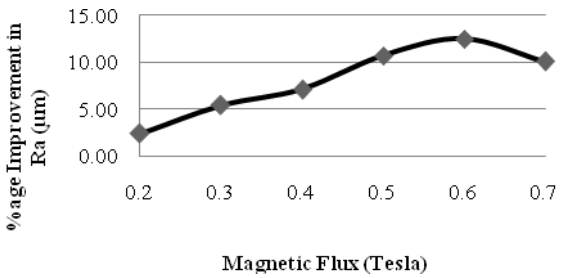

Fig. 4. Effect of magnetic flux density on (ΔRa)

It is further seen from Figs.3 and 4 that both MR and ΔRa decreases at higher values of magnetic flux density. This is a consequence of the fact that, initially, the total peaks available upon the surface of the workpiece are more. The greater the number of peaks, the more will be the material removal. However, as the surface is subjected to repeated cycles, the number of peaks and their heights continue decreasing, and hence the material removal declines after certain value of magnetic flux density. This may be explained as when a very strong magnetic field is applied around the workpiece, the abrasive particles get *ploughed* instead of *impinge* on to the work surface, thereby resulting in macro-chipping of the surface and enhancing the surface roughness.

5. Conclusions

A magnetic field has been applied around the workpiece being processed by MFAAFM and an enhanced rate of material removal and increase in percentage improvement in surface roughness were achieved. It can be concluded from study that; Magnetic field significantly affects both MR and ΔRa. The slope of the curve indicates that MR increases with magnetic field more than ΔRa. At 0.4 Tesla magnetic field densities MR is maximum and then there is marginal variation upto 0.6 Tesla. Thereafter the MR reduces sharply. ΔRa increases almost linearly upto 0.6 Tesla and thereafter after it reduces sharply.

References

[1] Siwert, D.E. (1974), “Tooling for the extrude hone process”, SME International Engineering Conference, pp.302–315.

[2] L.J. Rhoades (1985), “Abrasive flow machining and its use”. Proceedings of Non Traditional Machining Conference, Cincinnati, OH, December, pp. 111–120

[3] Przyklenk (1986) “Abrasive flow machining: a process for surface finishing and deburring of workpiece with a complicated shape by means of an abrasive laden medium”, Advances in Non-traditional Machining, PED, ASME,22:101–110.

[4] Williams, R.E., Rajurkar, K.P. and Rhoades, L.J. (1989) “Performance Characteristics of Abrasive Flow Machining”, SME Technical Paper No. FC 89-806

[5] Williams, R.E. and Rajurkar, K.P. (1992) “Stochastic modeling and analysis of abrasive flow machining”, Trans. ASME, J. Engg. for Ind., 114:74–81.

[6] Loveless T.R., Williams R.E., Rajurkar K.P.(1994), “A study of the effects of abrasive-flow finishing on various machined surfaces”, Journal of Materials Processing Technology 47:133-151.

[7] Shan, H.S. and Dubey, A.K. (1997). “Micro Machining by Flow of Abrasives”. Proceedings 17th AIMTDR Conference, Warrangal, India, 269–275.

[8] Jain R.K. and Jain V.K. (1999), “Abrasive fine finishing processes- a review", Int. J. of Manufacturing Science and Production, 2(1):55-68

[9] Jain, R.K., Jain, V.K. and Dixit, P.M. (1999) “Modelling of material removal and surface roughness in abrasive flow machining process”, Int. J. Machine Tool and Manufacture, 39:1903–1923.

[10] Rajurkar, K.P. and Kozak, J. (1999), “Hybrid Machining Process Evaluation and Development”, Online, www.unl.com

[11] Singh S. ,Shan H.S., and Kumar P. (2001),"Effects of magnetic field on abrasive flow machining processes", Proc. 12th Int. DAAAM Symposium Jena, Germany, October.

[12] Walia R.S., Shan H.S., Kumar P. (2006), “Parametric optimization of centrifugal force assisted abrasive flow machining (CFAAFM) By the Taguchi Method”. Journal of Materials and Manufacturing Processes, USA. Vol. 21, Issue 4,375-382.

[13] Walia R.S., Shan H.S., Kumar P. (2006b) “Multi-response optimization of centrifugal force assisted abrasive flow machining (CFAAFM) process through Taguchi method and Utility concept”, Journal of Materials and Manufacturing Processes, 21:907-914.

[14] Sankar R.M., Monda, S., Ramkumar J., Jain V.K. (2009), “Experimental investigations and modelling of drill bit-guided abrasive flow finishing (DBG-AFF) process”, International Journal of Advanced Manufacturing Technology, 42:678–688.

5-6

The effect of in-plane exit angle on burr minimization in face milling of medium carbon steels in dry environment

P.P. Saha, A. Das and S. Das
Department of Mechanical Engineering, Kalyani Govt. Engineering College, Kalyani- 741325, West Bengal, India

Abstract. Machining burr is a plastically deformed material adhered to the edge of the machined surface. It usually creates problem in production lines in terms of product quality and injury to the operator. So, burr prevention and its minimization are essential. An additional, non-productive deburring process is generally required for removal of burr. A number of experimental observation was performed in the past on burr formation and its minimization. The present experimental investigation has been performed on medium carbon steel (45C8) specimens to observe the extent of burr formation with different in-plane exit angles with and without an exit edge bevel. Encouraging results have been found when an exit edge bevel angle of 15° and in-plane exit angle is 60° are provided on the workpiece leading to negligible burr.

Keywords: Burr, exit edge bevel, in-plane exit angle

1. Introduction

Burrs are often observed in milling operation at the exit edge of the workpiece. Presence of burr in the finished component creates problem in assembly, work handling, etc. So, a finished component should be free from any burr. For this, an additional deburring operation may be employed to remove burr. It adds an extra cost that may be as high as 30% of the production cost. To understand the mechanism of burr formation and its minimization, several research works were carried out [1- 3].

Nakayama and Arai [1] classified machining burrs and reported that burrs might cause grove wear and accelerate burr growth. Gillespie [4, 5] observed that cost of deburring and edge finishing for precision components might constitute as much as 30% of the part cost. Chern and Dornfeld [6] did experiments on burr formation mechanism in orthogonal cutting and found out that negative shear plane tends to form when steady state chip formation stops as the tool moves to the end of the cut. Lee and Dornfeld [7] investigated micro-burr formation in machining. They studied the type and size of burr created on stainless steel 304 and also developed a control chart to minimize burr size. On the other hand, Luo et al. [8] did experimental investigation on the mechanism of burr formation in slot milling of aluminium alloy workpiece in feed direction. They found out an increasing trend of exit burr height with the increase in exit angle, and at 90° exit angle, large burr was observed. Biermann and Heilmann [9] did experiments on improvement of workpiece quality in face milling of aluminium alloys. They noted that the modification on machining process along with the use of cutting fluid is a promising approach to avoid deburring. On the other hand, Pekelharing [10], Hashimura et al. [11] and Das et al. [12] tried to explore burr formation mechanism using finite element method, and validated experimental findings. Classification of milling burrs according to the shape, location and burr formation mechanism based on fractography was also proposed [10]. Heisel et al. [13] observed that the influence of minimum quantity lubrication had minor effect on burr formation in face milling.

Saha et al. [14], Das et al. [15, 16], Saha and Das [17-19] and Das et al. [12] did experiments on burr formation. They reported that burr formation depends on various parameters, like exit edge bevel angle, in-plane exit angle, cutting velocity and feed. They investigated the machining burr formation in milling and shaping on different steels and aluminium alloy, and observed that burr became minimum at 15° exit edge bevel angle of the workpiece. This may be due to the need of less backup support material along the bevel.

The aim of the present experimental work is to obtain minimum or negligible burr formation on medium carbon steel (45C8) workpiece under different machining conditions considered. The influence of in-plane exit angle on burr formation of 45C8 steel workpiece without edge bevel and at 15^{o} exit edge bevel in face milling using coated carbide tool insert is experimentally investigated.

2. Experimental investigation

Experiments are done in a vertical axis CNC milling machine on medium carbon steel, with a single titanium titride (TiN) coated carbide tool insert mounted on a 54 mm diameter cutter to observe the nature of burr formation. Two set of experiments (set 1 and set 2) are carried out in dry environment. Constant cutting velocity *vc* = 339 m/min, depth of cut of *ap* = 3 mm and feed of *fz* of 0.1 mm/tooth are considered during experiments performed in dry condition. In-plane exit angle is varied from 30° to 150° at a step of 15° without any exit edge bevel in experiment set 1 to find out the condition for minimum burr formation.

Table 1. Experimental set up in CNC milling

Machine Tool	Vertical axis CNC milling machine Make: Bharat Fritz Werner (BFW) Ltd., Bangalore, India Model: Akshara VF30CNC, Sl. No 5081/269
Cutting Tool	Face milling cutter with a single TiN coated carbide insert Cutter specification: 490-054Q22-08M241259, Diameter: 54mm Make: Sandvik Asia Ltd., India Insert specification: 490R-08T308M-PM, Make: Sandvik Asia Ltd., India Condition and type of tool: Sharp new negative rake tool Normal clearance angle = 15°, Principal cutting edge angle = 75°
Job Material	Medium carbon steel (45C8) Size : 63 mm x 55 mm x 21 mm, Hardness: 175 HB Composition (wt%): C (0.44%), Si (0.29%), Mn (0.85), S (0.033%), P (0.028%), Fe (remainder)

In-plane exit angle is the angle between the cutting velocity vector at the exit point of the cutter leaving the workpiece and the cutter feed direction which is along the exit edge of the workpiece as considered in this work. To provide an exit edge bevel angle, the end portion of the workpiece where the cutter leaves it is beveled to have an inclination downward. Definition of in-plane exit angle and exit edge bevel angle was shown with schematic presentation in references [18, 19] of the first and corresponding author of this paper.

Next, in-plane exit angle is varied from 60° to 150° at a step of 15° with 15° exit edge bevel angle in experiment set 2. An exit edge bevel angle of 15° is chosen in this work following the observation reported earlier [12, 14, 17- 19]. The bevel is made of a height of 3 mm. After machining, the exit edge of workpiece is observed under a Mitutoyo, Japan make tool makers microscope, and the respective height of burr is measured. Details of the experimental set up and machining conditions are shown in Table 1 and Table 2 respectively.

3. Discussion on experimental results

After conducting milling experiments in experimental set 1, burr height of the specimen is measured using a tool makers microscope. Measured burr heights are presented in Fig. 1. It is noted from Fig. 1 that burr height is increased with increase in in-plane exit angle up to 105º, and has a decreasing tendency after that. Quit low burr height is observed at 30º in-plane exit angle. Low tool engagement may be the reason for small amount of burr height (68 μm) at 30º in-plane exit angle. Similar observation was also made by Avila and Dornfeld [20]. At 105º and 120º in-plane exit angle, burr height at exit edge is observed to be more than 300 μm.

Table 2. Machining conditions

Variables	**Experimental set 1**	**Experimental set 2**
Exit edge bevel angle (°)	0	15
In-plane exit angle (°)	30, 45, 60, 75, 90, 105, 120, 135, 150	60, 75, 90, 105, 120
Cutting velocity *vc* = 339 m/min, Depth of cut of *ap* = 3 mm, Feed of *fz* 0.1 mm/tooth, Environment: Dry		

Microscopic views of typical burrs for in-plane exit angle of 30º and 90º with no exit edge bevel angle of the workpiece are shown in Fig. 2 (a) and (b). It is clear from the photograph that at 30° in-plane exit angle, notably less burr is there, when at 90° in-plane exit angle, distinct saw tooth type burr is present.

In experiment set 2, face milling of medium carbon steel (45C8) has been performed with an exit edge bevel angle of 15°; in-plane exit angle is varied from 60º to 120º at a step of 15º for this experiment. As beyond an in-plane exit angle of 45°, average burr height of more than 100 μm occurs, in the experiment set 2, burr height is tried to reduce substantially with 15° exit edge bevel corresponding to in-plane exit angle of 60°-120°. Other machining conditions are given in Table 2.

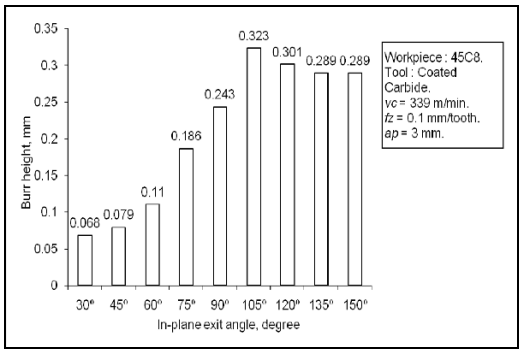

Fig. 1. Variation of average burr height with different in-plane exit angles of medium carbon steel specimens without beveled exit edge for experiment set 1

(a)

(b)

Fig. 2. Microscopic view of burrs of a face milled specimen for in-plane exit angle of (a) 30° and (b) 90º for medium carbon steel specimens with no edge bevel angle for experiment set 1 (View in the microscope is taken under x20 magnification)

Variation of average burr height with different in-plane exit angles under 15° exit edge bevel angle is presented in Fig. 3. It shows that burr height increases with an increase in in-plane exit angle up to 105° and then decreased at 120°. On the whole, burr height observed at these conditions is lesser than that observed without an exit edge bevel.

Gradual reduction in cutting force along the beveled edge results in less need of back up support, and thus reducing the height of burr. Quite low burr height of 16 μm is observed at 60° in-plane exit angle. Low tool engagement and less requirement of back up support material along the beveled exit edge of the workpiece may be the reason behind formation of negligible burr.

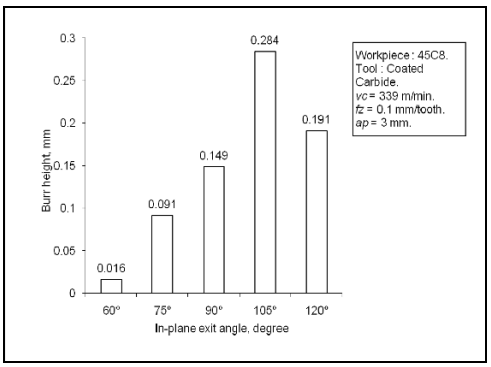

Fig. 3. Variation of burr height with different in-plane exit angles under 15° exit edge bevel of medium carbon steel specimens for experiment set 2

Figure 4 (a) and (b) show microscopic view of typical burrs for in-plane exit angle of 60º and 90º with 15º exit edge bevel of the workpiece. Presence of almost no burr is observed from Fig. 4 (a) at 60° in-plane exit angle, while saw tooth type burr with lesser frequency is there as seen in Fig. 4 (b) at 90° in-plane exit angle with the provision of an exit edge bevel angle of 15°.

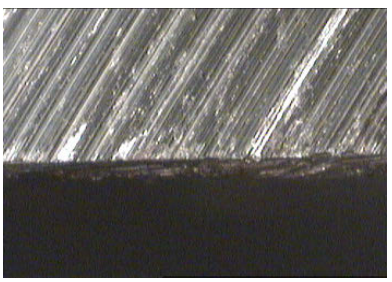

(a)

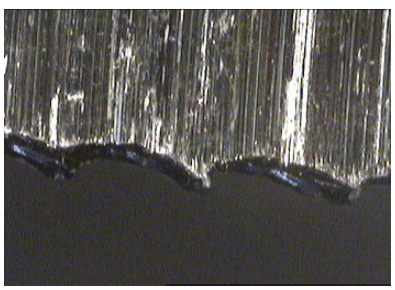

(b)

Fig. 4. Microscopic view of burrs of a face milled specimen for in-plane exit angle of (a) 60° and (b) 90º for medium carbon steel specimens with 15º edge bevel angle for experiment set 2 (View in the microscope is taken under X20 magnification)

4. Conclusions

From the experimental observation on milling burr formation at the exit edge of medium carbon steel (45C8) specimens under dry environment, following conclusions may be drawn; Low burr height of 68μm is observed using coated carbide tool at 30° in-plane exit angle with no exit edge bevel of the workpiece at the selected machining condition. When an exit edge bevel angle of 15° is provided, burr height observed at these conditions is lesser than that observed without an exit edge bevel. Negligible burr of only 16 μm height is also found corresponding to an in-plane exit angle of 60°. To obtain negligible burr, hence, either quite small in-plane exit angle is to be provided, or an exit edge bevel angle of 15° is to provide with a suitable in-plane exit angle.

References

[1] Nakayama K, Arai M, (1987) Burr formation in metal cutting, Annals of the CRIP, 36(1): 33-36.
[2] Gillespie LK, Bolter PT, (1976) The formation and properties of machining burr, Transactions of the ASME, Journal of Engineering for Industry, 98(1): 66-74.
[3] Ko SL, Dornfeld DA, (1991) A Study on burr formation mechanism, Transactions of the ASME, Journal of Engineering Materials and Technology, 113(1): 75-87.
[4] Gillespie LK, (1985) The academic challenge of burr technology, Allied bendix aerospace, KC division, SME paper no. BDX 613-3151.
[5] Gillespie LK, (1979) Deburring precision miniature parts, Precision Engineering, 1(4): 189-198.
[6] Chern GL, Dornfeld DA, (1996) Burr/Break out model development and experimental verification, Transactions of the ASME, Journal of Engineering Materials and Technology, 118(2): 201-206.
[7] Lee K, Dornfeld DA, (2005) Micro-burr formation and minimization through process control, Precision Engineering, 9: 246-252.
[8] Luo M, Lin G, Chen M, (2008) Mechanism of burr formation in slot milling Al-alloy, International Journal of Materials and Product Technology, 31(1): 63-71.
[9] Bierman D, Heilmann M, (2009) Burr minimization strategies in machining operations, Proceedings of the CIRP International Conference on Burrs- Analysis, Control and Removal, Part-1, University of Kaiserslautern, Germany: 13-20.
[10] Pekelharing AJ, (1978) The exit angle failure in interrupted cutting, Annals of the CIRP, 27(1): 5-10.
[11] Hashimura H, Chang YP, Dornfeld DA, (1999) Analysis of burr formation mechanism in orthogonal cutting, Transactions of the ASME, Journal of Manufacturing Science and Engineering, 121(1): 1-7.
[12] Das A, Saha PP, Das S, (2011) Burr minimization in shaping En25 steels: using experimental and stress analysis technique, International Journal of Manufacturing and Industrial Engineering, 2(2): 61-65.
[13] Heisel H, Schaal M, Wolf G, (2009) Burr formation in milling with minimum quantity lubrication, Production Engineering Research and Development, 3: 23-30.
[14] Saha PP, Das D, Das S, (2007) Effect of edge beveling on burr formation in face milling, Proceedings of the 35th International MATADOR Conference, Taipai, Taiwan: 199-202.
[15] Das A, Mondal P, Samanta S, Das S, Mahata S, (2011) Burr minimization in milling: through proper selection of in-plane exit angle, Journal of the Association of Engineers, India, 81: 38- 47.
[16] Das A, Saha PP, Das S, (2011) Minimization of burr formation in milling of nickel chrome alloy steels: through appropriate selection of in-plane exit angle, Indian Science Cruiser, 25(5): 43-49.
[17] Saha PP, Das S, (2010) A study on the effect of process parameters and exit edge beveling on foot and burr formation during machining of medium carbon steels. Proceedings of the National Conference on Recent Advances in Manufacturing Technology and Management, Jadavpur University, Kolkata: 30-35.
[18] Saha PP, Das S, (2011) A simple approach for minimization of burr formation using edge beveling of alloy steel workpieces, International Journal of Mechatronics and Intelligent Manufacturing, 2(1/2): 73-84.
[19] Saha PP, Das S, (2011) Burr minimization in face milling: an edge beveling approach, Proceedings of the Institution of Mechanical Engineers, Part B: Journal of Engineering Manufacture, 225(9): 1528-1534.
[20] Avila MC, Dornfeld DA, (2004) On the face milling burr formation mechanism and minimization strategies at high tool engagement, Proceedings of the International Conference on Deburring and Edge Finishing, University of California, Berkeley: 191-200.

5-7

A surface generation model for micro cutting processes with geometrically defined cutting edges

Jost Vehmeyer[1], Iwona Piotrowska-Kurczewski[1] and Sven Twardy[2]
[1] University of Bremen, Center for Industrial Mathematics, 28359 Bremen, Germany
[2] University of Bremen, Laboratory for precision machining, 28359 Bremen, Germany

Abstract. Conventional machining techniques like milling and turning are well established techniques in manufacturing. In the last years considerable progress in miniaturisation of components has been made. Micro-machining operations have made the production of small components flexible, but scaling down these processes is extremely challenging. In the production of dies and molds special attention is paid to the forming zone where surfaces interact under heavy stress. Optimization of the tribological behaviour has been investigated over the last few years due to high rejection rates. The simulation of micro-structures and topographical characterisation are essential factors for the study of the functional performance of surfaces. Our contribution is a numerical surface generation model, which is able to simulate the micro-topography for machining operations with geometrically defined cutting edges. In the presented model the tool-workpiece kinematics are described by static and dynamic motions, including tool run-out and tool deflection caused by cutting forces. In the material removal algorithm, the minimum chip thickness and tool wear are considered. Experiments for ball-end milling are carried out for different process parameters to verify the simulation results.

Keywords: surface generation, micro-topography, ball-end milling, tool deflection

1. Introduction

Mechanical micro-machining is commonly used in the production of micro-components. Besides the geometric specification, there is a growing demand for textured or structured surfaces to provide a desired functionality [1]. Therefore the understanding of surface generation mechanisms and prediction of micro-topography is an essential step to make the production chain as effective and functional as possible.

In micro-milling, helical ball-end tools have been developed, due to their flexible abilities in production of sculptured surfaces. Round-nosed tools have a more complicated tool-workpiece engagement than cylindrical tools, which is recognizable by non-constant machining variables like cutting-depth a_p or uncut chip thickness h and comma-shaped chips. Therefore, even under ideal conditions, the kinematic surface topography for ball-ends is quite complex. In [2] the term pick-scallop and feed-scallop are introduced to describe the surface topography under ideal conditions. Both scallops are the result of the curvilinear shape of ball-ends and will not occur for cylindrical or insert tools. In [3], topography of face milled surfaces is simulated and verified by experiments.

This paper is organized in two parts, first we introduce the surface generation model, followed by some experimental verifications.

2. Surface generation model

Mechanically machined surfaces are the result of a highly complex material removal process and the first question that arises is on which scale the surface is to be simulated.

In macro-scale machining, surface simulation is widely used for virtual prototyping or tool path optimization. When surface topography becomes the main object of study, the degree of idealization may be reduced. This especially concerns tool sweeping and material removal. Swept volumes are used in terms of computer graphics to statically represent the space that is traversed by an object in motion. To study the global form of a workpiece, form deviation, or waviness, one option would be to occupy the swept volume of the tool by moving a simplified model of the tool, e.g. an implicit representation of the volume of revolution, along the tool path. Afterwards, this volume can be subtracted by a Boolean operation from the workpiece to get the machined surface.

To study micro-structures, the above method must be improved in two points. An obvious improvement is to uncouple translational from rotational motion by sweeping the cutting edge rather than the volume of rotation. Especially for rotating round-nosed tools this advancement is crucial. The Boolean material removal is an accepted idealization at micro-scale; it is equivalent to an ideal sharp cutting edge. At macro-scale the edge

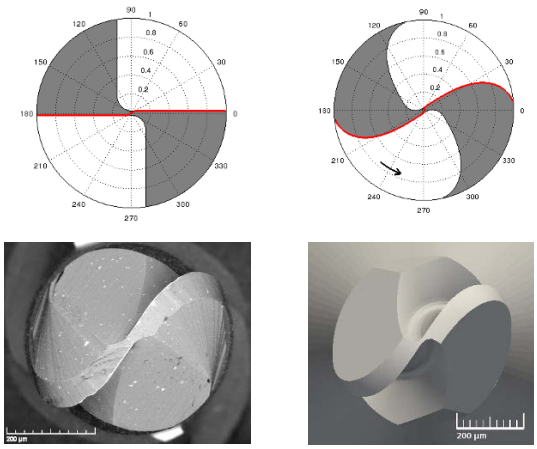

Fig. 1. top: crosssectional area and projected area, bottom: ball-end SEM micrograph (left), computer model (right)

radius of a cutting tool is insignificant small compared to the tool radius. It is a fact that the edge radius cannot be downscaled like other tool dimensions; this phenomenon is known to be a size effect in micro machining [4]. Therefore a modified material removal is used in the presented model, which is presented in the following subsections.

3. Tool geometry

The cutting edge geometry directly affects surface topography. Helical ball-end millers have mostly two curvilinear cutting edges, which are a result of the spheric tool tip and helix angle. Geometrically, they are built by the intersection line of flank face and rake face. One option for calculation is to project the cross-section area onto a sphere, taking the helix angle α into account, exemplarily shown in Fig. 1. For the simulation, a parametrisation of the first cutting edge is needed, it is formulated with tool length l and radius r. For small cutting depths (e.g. 15µm) the helical curvature of the active part of the cutting edge is hardly visible, so an idealisation for the y-component in (1), setting it to a small offset, is acceptable. We investigate this offset with the help of microscopic examination; Fig. 1 shows a SEM micrograp of a ball-end of radius 250µm.

$$(x, y, z, 1)^T = \varepsilon(\varphi) =$$
$$(r\cos\varphi, y(\varphi), r\sin\varphi - 1 + r)^T, \qquad \varphi \in [0, \pi/2]$$

Furthermore, it is important to note that the edge geometry changes during operation. The effect of wear is clearly visible in micrographs and due to the discrete nature of the model, simple to include by flattening the edge according to the width of wear mark.

4. Kinematic model

For the tool sweeping algorithm, we need a unique configuration of the tool in the coordinate system, which is given by 3 rotations and 3 translations. This is provided by the kinematic model, which takes process-defined kinematics, as well as positioning errors into account. Even in fields of precision machining, positioning errors can never be avoided entirely. To the contrary, the effect of a misaligned tool on the surface generation increases, as downscaling continues. Positioning errors are classified into static ones, e.g. tool run-out, which results if tool and spindle location are not precisely concentric, and dynamic ones, like vibrations or cutting forces.

The tool trajectories are composed by the rotational and translational motion of the tool. As proposed in [5], a concatenation of homogeneous matrices is used to formulate the tool trajectories, leading to the parameter to state operator

$$\Phi : P \to \Re^{4\times 4},$$

where P denotes the parameter space. The static part of Φ consists of the rotational and translational tool motion, furthermore a run-out is included by using a parallel axis offset $\rho = (\rho_x, \rho_y, 0)^T$.

In order to include dynamical changes into the generation of tool trajectories, we implemented a dynamic force model, which interacts with the process parameter cutting depth a_p and feed velocity v_f. Cutting force can be formulated as a function of a_p and v_f and gives the deflection of tool tip $\delta \sim F$. On the other hand a_p and v_f are functions of δ. This interaction leads to a system of ordinary differential equations, described detailed in [5].

5. Material removal

At macro scale, usually an ideally sharp cutting edge is assumed. Realizing that the cutting edge is built by a cylindric shell, the material removal mechanism becomes more complicated. It has been known for a long time that a threshold for the undeformed chip thickness exists, below which chip formation is disturbed or impossible [6]. For round nosed tools this is not only critical when

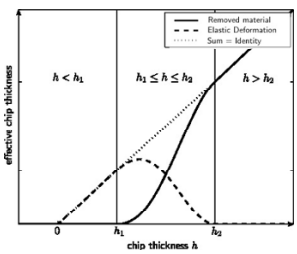

Fig. 2. Truncation of chip thickness

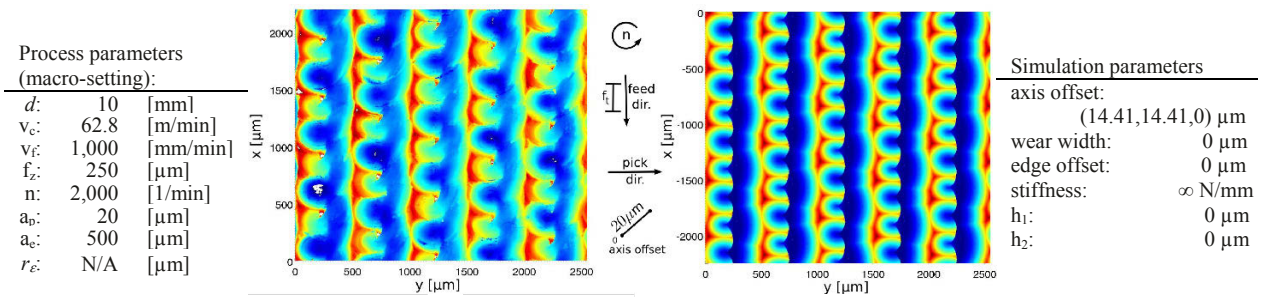

Fig. 3. Process parameters for the macro setting, resulting experimental and simulated surface.

small cutting depths are used. Surface topography is affected by the minimum chip thickness for arbitrary cutting depths, caused by the complex tool-workpiece engagement for ball-ends. The chip thickness h takes values in $[0,h_{max}]$, depending on the location of the cutting edge and will always go below the minimum chip thickness on a small part of the cutting edge. Therefore, the minimum chip thickness is an important factor for the topography of ball-end machined surfaces.

It has been established to divide the chip formation in micro-scale machining into three parts, compare [7]. Below the minimum chip thickness, material is elastically deformed, no material is removed. When undeformed chip thickness is approximately equal to the minimum chip thickness, material is both deformed and removed. At significantly higher chip thickness compared to the minimum chip thickness deformation still exists, but is negligible compared to the material removed.

To model the effect of minimum chip thickness for surface generation, we apply a truncated chip thickness to the material removal procedure. To avoid abrupt scallops, we use a continuous truncation; modeled with help of the function $f(h)$, see Fig. 2. The truncation function is demarcated by two points $h_1 < h_{min} < h_2$ into the three schematic chip formation sections:

For $h < h_1$ pure elastic material deformation followed by complete recovery is assumed. In this case no material will be removed. In middle section $h_1 \le h \le h_2$ both elastic recovery and material removal take place. This interval represents the critical phase $h \approx h_{min}$, where chip formation is unstable. Rake angle will be negative and chips are sheared off the material. For $h > h_2$, ideal chip formation takes place and deformation is reduced to an insignificant value.

6. Numerical results and experimental verification

The surface model describes in the last section has been implemented in MATLAB. The algorithm is similar to the Z-buffer method, commonly used in computer graphics. The essential modification is the concatenation of the truncation function.

Experimental verification was carried out on a precision milling machine tool (Ultrasonic 20 linear, Sauer GmbH). For first milling experiments common 2-fluted ball-end shaped uncoated HSS cutting tools with a diameter d of 10 mm were used in combination with aluminum alloy (AlMg3), which is known for good machineability. This setup should exclude as many influences as possible and show the true kinematic profile of the tool engagement. Uncut chip thickness is very high (f_z=250µm) compared to the cutting edge radius of an uncoated cutter. Furthermore, tool deflection is also negligible, because of the ratio between shank diameter and cutting forces. Cutting forces were recorded using a 3-axis piezo-dynamometer (MiniDyn 9256C2, Kistler Holding AG). After milling experiments were carried out, all machined surfaces were measured by an optical profilometer (Plµ 2300, Sensofar Technology GmbH).

After the macro test, applying a 10 mm cutter on aluminum, the experimental validation for micro milling of hardened steel was carried out on the same machine tool. For micro milling experiments 2-fluted ball-end shaped tungsten carbide cutting tools with a diameter d of 500 µm and TiAlN coating (VHMSK, Van Hoorn Hartmetaal BV) were used. A spray formed HSS Alloy (C1Cr8Mo2V0.4Al1, 67 HRC) was used as workpiece material. This Alloy is of great interest for micro cold forming tools, because of its outstanding mechanical

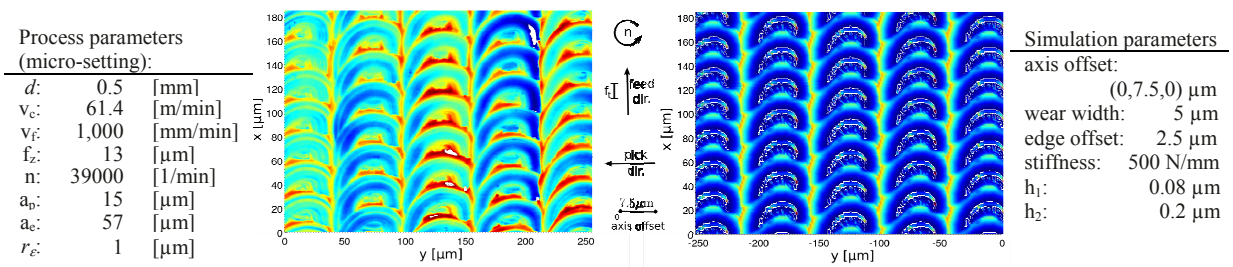

Fig. 4. Process parameters for the micro setting, resulting experimental and simulated surface.

properties and was also showing sufficient machinability in former tests [8].

Cutting conditions and the resulting surfaces of experiment and simulation for the macro and micro setting are presented in Fig. 3 and Fig. 4 respectively.

7. Discussion

To verify the pure kinematic surface generation, experiments at macro scale for up- and down-milling mode and an alternating combination of both are carried out. In all cases simulation and experiment can be identified with high visual conformity and the Abbott curves show a good agreement of high distribution. These results are achieved by choosing almost ideal simulation parameters, i.e. ideally sharp cutting edge in the sense of no truncation of chip thickness and ideal edge geometry. The run-out effect is too dominant to be neglected and is clearly visible in force signal. Absolute value and direction of the axis offset is determined by manual minimization of the error between measured and simulated surface.

In a next step the milling process is scaled down from d=10mm to d=0.5mm. The surface topography of the micro process can hardly be identified as a downscaled version of the macro-sized surface. The structure shows a complete different characteristic. In particular, the feed scallops are more or less symmetric along tool path and have a distance of the twice of feed per tooth, instead of feed per tooth. This means that cutting action is not even, anymore. In the simulation this effect is reproduced with the run-out in combination with the effect of minimum chip thickness. The demarcation points h_1 and h_2 are chosen the same as above by visual inspection. This technique may be extended to a new method for determination of the minimum chip thickness value. Mathematically this is a parameter identification problem. In general, the determination of minimum chip thickness is still challenging, influencing factors are complex and indirect methods are required [9].

8. Conclusion

Overall, this study shows that the presented surface generation model can control the basic mechanisms of surface generation and provides an accurate prediction of surface topography for macro-scaled processes. Taking the minimum chip thickness into account, the simulation is qualified to identify the significant surface structures in micro-sized ball-end milling, too. To meet the exact high distribution, further optimizations of the kinematic or material removal model are necessary.

Furthermore, the presented surface simulation has concrete potential for deeper mathematical investigations. Due to growing requirements in precision and functional performance, micro-cutting processes have become subject of mathematical optimization [10]. Surface generation is the last and most important step in modeling a cutting process and combines the results of all involved sub-models like force and vibration model.

Acknowledgments: The work presented in this article was supported by the German Foudation (DFG) within the SFB 747, subproject C2 and the grant SPP 1480 German Research Foundation (DFG).

References

[1] Bruzzone, A.A.G. ; Costa, H.L. ; Lonardo, P.M. ; Lucca, D.A. Advances in engineered surfaces for functional performance, CIRP Annals - Manufacturing Technology. 57(2008) 2 - p. 750-769 , 2008

[2] J.S.A Chen, Y.K. Huang, and M.S. Chen. A study of the surface scallop generating mechanism in the ball-end milling process. International Journal of Machine Tools and Manufacture , 45(9):10771084, 2005.

[3] M.A Arizmendi, J. Fernandez, L.N.L.d. Lacalle, A. Lamikiz, A. Gil, J.A. Sanchez, F.J. Campa, and F. Veiga. Model development for the prediction of surface topography generated by ball-end mills taking into account the tool parallel axis offset. experimental validation. CIRP Annals - Manufacturing Technology, 57(1):101104, 2008.

[4] F. Vollertsen. Categories of size effects. Product Eng, 4(2):377#383, 2008

[5] I. Piotrowska-Kurczewski, J. Vehmeyer. Simulation model for micromilling operations and surface generation. Advanced Materials Research, 223:849858, 2011.

[6] P. Stockinger. Die Bedeutung der Mindestspandicke in der spanabnehmenden Fertigung. Feinwerktechnick, 73 Heft 6:253256, 1969.

[7] A. Aramcharoen and P.T. Mativenga. Size effect and tool geometry in micromilling of tool steel. Precision Engineering, 33(4):402#407, 2009.

[8] Brinksmeier, E.; Riemer, O.; Twardy, S.: Surface Analysis of Micro Ball End Milled Cold Work Tool Steels. Proceedings of the 2nd Nanoman, International Conference on Nanomanufacturing, Tianjin (2010) #173.

[9] Mian A.J, Driver N., and Mativenga P.T: Estimation of minimum chip thickness in micro milling using acoustic emission, Proceedings of the Institution of Mechanical engineers, Part B: Journal of Engineering Manufacture, vol. 225 no. 9 1535-1551, doi: 10.1177/0954405411404801.

[10] Brandt, P. Maaß, I. Piotrowska-Kurczewski, S. Schiffler, O. Riemer, E. Brinksmeier: Mathematical methods for optimizing high precision cutting operations. To appear in the International Journal of Nanomanufacturing.

An investigation into abrasive water jet machining of TRIP sheet steels using Taguchi technique and regression models

J. Kechagias[1], I. Ntziantzias[2], N. Fountas[3], N.M. Vaxevanidis[3]
[1] Department of Mechanical Engineering, Technological Educational Institute of Larissa, Larissa GR 41110
[2] Department of Mechanical and Industrial Engineering, University of Thessaly, Volos 38334, Greece
[3] Department of Mechanical Engineering Educators, School of Pedagogical & Technological Education (ASPETE), N. Heraklion Attikis GR 14121, Greece

Abstract. An experimental investigation of abrasive water-jet machining (AWJM) of transformation induced plasticity (TRIP) multi-phase sheet steels using design of experiments was carried out. The quality characteristics selected for examination were the Kerf mean width and average surface roughness. The process parameters were the nozzle diameter, the stand-off distance and the traverse speed. For the design of experiments the Taguchi methodology was applied. Optimal process parameter values were identified and regression models were applied to the experimental results and were tested by using evaluation experiments. All the predictions are reasonable and compares well with the experimental values. The experimental design indicated that the nozzle diameter is the most important parameter that affects the mean Kerf width and surface roughness followed by the stand-off distance. The proposed methodology could be easily applied to different materials and initial conditions giving reliable predictions, resulting in process optimization and providing a possible way to avoid time- and money-consuming experiments.

Keywords: AWJM, Taguchi design, Kerf width, Surface roughness

1. Introduction

The AWJM belongs to the category of non-conventional material removal methods and it is used in industry to machine different materials ranging from soft, ductile to hard and brittle materials. This process does not produce dust, thermal defects or fire hazards. It is a preferable process for shaping composite materials and imparts almost no surface delamination, see [1].

The primary interests in TRIP sheet steel processing by AWJM are the Kerf shape (Kerf width and Kerf taper) and surface quality (surface roughness of cut), as well as burrs which may be formed at the jet exit (Figure 1). Kerf shape and quality in slotting sheet materials by AWJM and the resulting surface roughness have been studied in recent research works [2-4].

The innovation of the present work relies on the use of a hybrid modeling approach based on the Taguchi method and the regression analysis for the modeling of cutting surface quality characteristics in AWJM. The experiments were performed on TRIP 800 HR-FH steel sheets which were processed using AWJM with three different diameters of the nozzle (nozzle diameter), three different distance values between the nozzle and the sheet steel (stand-off distance) and three different traverse speeds (also known as cutting speed or travel speed).

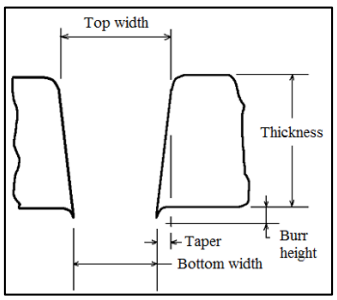

Fig. 1. Schematic representation of a typical cut in AWJM.

An L_9 (3^4) orthogonal array was used in order to reduce the experimental effort, following the Taguchi design of experiments [5]. Taguchi design uses an orthogonal matrix experiment for the parameter design of a process and exploits the orthogonality of the matrix in order to predict the performance of a quality characteristic according to parameter levels.

The selected quality characteristics (also known as performance measures) were the mean Kerf width (Kerf) and the arithmetic mean surface roughness (Ra). Analysis of means (ANOM) and analysis of variances (ANOVA) were applied on the experimental results and the best combination of parameter levels is obtained and the effect of each process parameter on the Kerf and Ra are revealed. Finally, interactions between the process parameters are examined and regression models are adopted and evaluated for Kerf and Ra parameters predictions.

2. Experimental design and procedures

Details concerning the experimental procedure and the materials are given elsewhere; see [6]; therefore only the main features are summarized below.

The TRIP steel tested was designated as TRIP 800 HR-FH. Specimens of materials were of square form (10x10 cm^2). Machining was performed on a SIELMAN HELLENIC HYDROJET industrial AWJM system. In each specimen a slot of 3 cm in length was cut. Each slot corresponds to different machining conditions. After processing, each specimen was separated in order to allow surface roughness measurements to be performed on the machined surface.

The pressure at which a water jet operates is about 400 MPa, which is sufficient to produce a jet velocity of 900 m/s. Such a high-velocity jet is able to cut materials such as ceramics, composites, rocks, metals etc [1].

Based on Taguchi design, the standard orthogonal array L_9 (3^4) has been selected in order to perform the matrix experiment [5]. Three levels for each factor were selected (Table 1). Following the L_9 (3^4) orthogonal array nine experiments were performed (Table 2). Columns 1, 2, and 3, are assigned to nozzle diameter (A, mm), stand-off distance (B, mm), and traverse speed (C, mm/min), respectively.

The performance measures were the arithmetic mean surface roughness (Ra, μm) and the mean Kerf width (Kerf, mm).

Ra measurements were performed with a Surtronic 3+ profilometer. As it is illustrated in Figure 1 the Kerf is of tapered form and to evaluate this characteristic, the semi-sum of the upper area width and the lower area width were measured by a stereoscope [7].

3. Experimental results and analysis

The Taguchi design is in fact a simple technique for optimizing the process parameters. The main parameters are located at different rows in a designed orthogonal array [5]. Thus, an appropriate number of statistically important experiments are conducted. Generally, the signal to noise (S/N) ratio (η, dB) represents the response of the data observed in the Taguchi design of experiments. Both, the arithmetic mean roughness, Ra and the mean Kerf width are characterized as 'the smaller the better' quality characteristics since lower values are desirable. The objective function for such quality characteristics is defined as follows [5]:

$$\eta = -10\log_{10}\left[\frac{1}{n}\sum_{i=1}^{n} y_i^2\right] \quad (1)$$

In Eq. (1) y_i is the observed data at the i^{th} trial and k is the number of trials [5]. By analyzing the observed data (S/N ratios), the effective parameters having an influence on the quality response can be seen and the optimal levels of the process parameters can be obtained.

Table 1. Parameter Design

Process Parameters		Units	Levels		
			1	2	3
A	nozzle diameter	mm	0.95	1.2	1.5
B	stand-off dist.	mm	20	64	96
C	traverse speed	mm/min	200	300	600
D	vacant	-	-	-	-

Table 2. Matrix experiment

	Proc. Parameters				Obj. Functions	
No	A	B	C	D	η_{Kerf} (dB)	η_{Ra} (dB)
1	0.95	20	200		0.19	-13.1
2	0.95	64	300		-1.25	-15.8
3	0.95	96	400		-0.68	-17.0
4	1.2	20	300		-1.40	-16.0
5	1.2	64	400		-1.22	-16.4
6	1.2	96	200		-3.21	-16.8
7	1.5	20	400		-2.829	-15.3
8	1.5	64	200		-3.528	-16.5
9	1.5	96	300		-3.862	-16.7
mean					-1.979	-15.9

According to the L_9 orthogonal array, nine experiments were performed with each experiment producing a 3 cm long slot in which the mean Kerf width and the average surface roughness (Ra) were measured. Then, each objective function η_{Kerf}, and η_{Ra} was calculated according to the negative logarithmic formula (Table 2):

$$\eta_{Kerf} = -10\log_{10}\left[Kerf^2\right]$$
$$\eta_{Ra} = -10\log_{10}\left[Ra^2\right] \quad (2)$$

For each of the three process parameters (A, B, and C) an average value, m_i for every level i, was calculated for each of the two performances measures (Table 3).

Based on the average values, ANOM diagrams (Fig. 2) were drawn indicating the impact of each factor level on the performance measures η_{Kerf} and η_{Ra} of the parts fabricated. Thus, based on the ANOM, one can derive the optimum combination of process variables, with respect to performance. The optimum level for a factor is the level that gives the maximum value of η.

Table 3. Mean parameter values

	η_{Kerf}			η_{Ra}		
	1	**2**	**3**	**1**	**2**	**3**
m_{Ai}	-0.58	-1.94	-3.40	-15.2	-16.3	-16.1
m_{Bj}	-1.34	-2.00	-2.58	-14.7	-16.2	-16.8
m_{Ck}	-2.18	-2.17	-1.57	-15.4	-16.1	-16.2

Table 4. ANOVA analysis

		Kerf			**Ra**		
Par.	**Deg. of Fr.**	**Sum of Sq.**	**Mean Sq.**	**%**	**Sum of Sq.**	**Mean Sq.**	**%**
A	2	11.9	5.98	74.7	1.99	0.99	17.1
B	2	2.3	1.15	14.4	6.64	3.32	56.9
C	2	0.72	0.36	4.5	1.07	0.53	9.2
Tot	8	16.0			11.6		
Er	2	1.01	0.50		1.95	0.97	

According to the ANOM diagrams mean Kerf width is affected mainly by nozzle diameter. On the other hand, the stand-off distance and nozzle diameter mostly affect the surface roughness Ra.

Moreover, it was evident that when the traverse speed increased, the mean Kerf width decreased and the surface roughness increased.

Taguchi design performs an analysis of variances (ANOVA) of the experimental results in order to evaluate the relative importance of the process parameters and error variances. The ANOVA analysis results can be seen in Table 4 for the mean Kerf width and surface roughness.

According to the ANOVA analysis the nozzle diameter affects the mean Kerf width and the surface roughness by about 75 % and 17 % respectively. The stand-off distance affects the surface roughness at most by approximately 57 %.

Interaction charts between nozzle diameter and standoff distance can be seen in Fig. 3 concerning Kerf and Ra, respectivelly.

4. Predictive modeling and evaluation

Assuming that: (i) the process parameters are continuous and controllable within the range of machining experiments, (ii) there are "synergistic" interactions between the process parameters as indicated by the interaction charts, (iii) the dominant parameter for the mean Kerf width variation is the nozzle diameter, (iv) the dominant parameters for the surface roughness variation are the stand-off distance and the nozzle diameter; the response regression model for each of the quality indicators can be expressed as follows:

$$y = b_1 + b_2A + b_3B + b_4C + b_5AB \pm e \quad (3)$$

In Eq. (3) y is the corresponding response of each objective function, bi, coefficients which should be determined and e is the error. Interaction terms are used due to 'synergistic' interactions between process parameters as it is evident from the plots in Fig. 3.

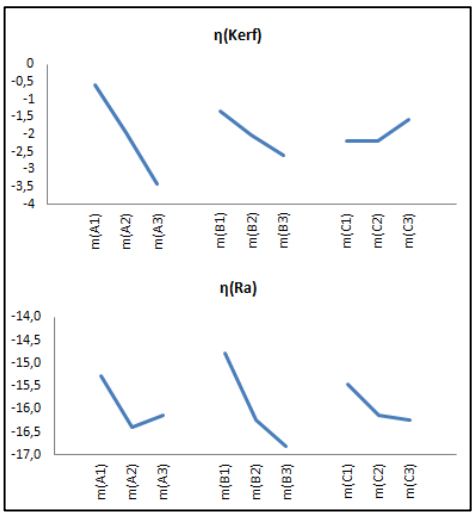

Fig. 2. ANOM diagrams

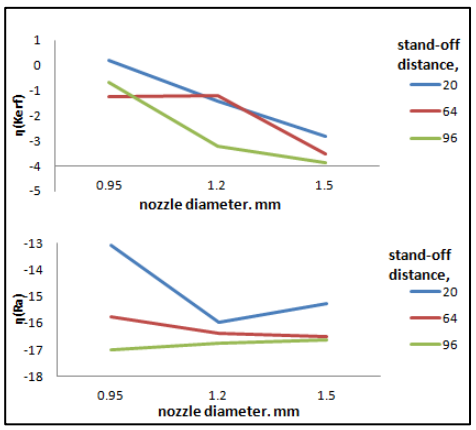

Fig. 3. Interaction charts

In general, Eq. (3) can be written in a matrix form as:

$$Y = bX + E \quad (4)$$

In Eq. (4), Y is the matrix of the measured values for the y response and X the matrix of process parameters and

their products. The matrices b and E consist of coefficients and errors, respectively. The solution of Eq. (4) can be obtained by a matrix approach [8].

$$b = (X^T X)^{-1} X^T Y \quad (5)$$

In Eq. (5) X^T is the transpose of matrix X and $(X^T X)^{-1}$ is the inverse of the matrix $(X^T X)$.

From the data listed in Table 2 and Equation (5), b_i coefficients for each objective function were calculated and then tabulated in Table 5.

Table 5. b_i coefficients

	b_1	b_2	b_3 ($x10^{-2}$)	b_4 ($x10^{-3}$)	b_5 ($x10^{-2}$)
η_{Kerf}	6.3	-7.2	-5.9	4.9	3.5
η_{Ra}	-8.5	-4.4	-8.8	-1.2	5

Three evaluation experiments were carried out in order to compare the actual valueswith the predicted ones given from Eq. (5). The results are presented in Table 6.

The proposed regression models can be used for the optimization of the cutting parameters during AWJM of TRIP 800 HR-FH steel sheets. This can be done by testing the behavior of the response variable (Kerf and Ra) under within a range of values of the nozzle diameter, the stand-off distance and the traverse speed (Fig. 4).

Table 6. Evaluation experiments

Exp. No	Kerf (mm)	Ra (μm)
A|B|C	Pred|Act|Dev%	Pred|Act|Dev%
0.95|20|300	0.95|0.87|9.4	4.96|5.3|-6.3
1.2|64|200	1.32|1.28|3.1	6.24|6.8|-8.2
1.5|96|400	1.43|1.51|-5.1	7.04|6.9|2.0

5. Conclusions

The mean Kerf width and the mean surface roughness (Ra) have been selected as the quality indicators for AWJM process multi-parameter optimization using Taguchi design.

The experimental design indicated that the nozzle diameter is one of the most important parameters that affect the mean Kerf width and surface roughness by 75% and 17% respectively. The stand-off distance was the second most important parameter within the experimental range tested and affects the mean Kerf width and surface roughness by 14%, and 57% respectively. Traverse speed also affect the mean Kerf width and surface roughness but by lower degree than the nozzle diameter and stand-off distance. The mean Kerf width decreases when nozzle diameter decreases or stand-off distance decreases. The surface roughness Ra decreases when distance decreases and/or nozzle diameter decreases stand-off.

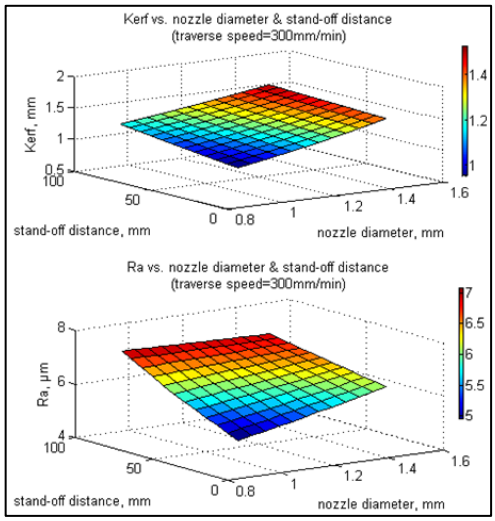

Fig. 4. Behaviour of the response variables

In addition, regression models were applied to the experimental results and three verification experiments were carried out in order to compare the measured (actual) and the predicted values. All the predictions are reasonable and close to the actual values.

Results obtained indicate that both the proposed approaches could be effectively used to predict the Kerf geometry and the surface roughness in AWJM, thus supporting the decision making during process planning.

References

[1] Momber AW, Kovacevic R (1997) Principles of abrasive waterjet machining. Springer.

[2] Gudimetla P, Wang J, Wong W (2002) Kerf formation analysis in the abrasive waterjet cutting of industrial ceramics. J Mater Process Tech 128:123-129.

[3] Hascalik A, Ulas C, Gurun H (2007) Effect of traverse speed on abrasive waterjet machining of Ti–6Al–4V alloy. Mater Design 28(6):1953-1957.

[4] Valicek J et al (2007) Experimental analysis of irregularities of metallic surfaces generated by abrasive waterjet. Int J Mach Tool Manuf 47(11):1786-1790.

[5] Phadke MS (1989) Quality Engineering using Robust Design. Prentice-Hall, Englewood Cliffs, NJ.

[6] Kechagias J, Petropoulos G, Vaxevanidis N (2011), "Application of Taguchi design for quality characterization of abrasive water jet machining of TRIP sheet steels", Int J Adv Manuf Tech, DOI 10.1007/s00170-011-3815-3.

[7] Petropoulos G, Tsolakis N, Vaxevanidis NM, Antoniadis A (2009) Topographic description of abrasive waterjet machined surfaces, Proceedings 2nd European Conference on Tribology (ECOTRIB 2009), Pisa, Italy, p.309-314.

[8] Box GEP, Hunter WG and Hunter JS (1978) Statistics for Experimenters. Wiley.

SelecTool: Software tool for the search and comparison of cutting tools depending on standard, geometric and cutting properties and user's criteria

Juan Arjona Montes[1], Joaquim Minguella i Canela[1], Joan Vivancos i Calvet[2]
[1]Fundació Privada Centre CIM
[2]Dept. d'Enginyeria Mecànica, Universitat Politècnica de Catalunya

Abstract. Sometimes it is difficult to choose one or several cutting tools for specific or general uses between the myriad of tools that exist today in the market. It is also necessary to spend lots of time analyzing costs and other important properties between the models that are available. To overcome this, there exist some software applications that might help, but normally with clearly commercial purposes that can distort the best selection. For this reason, trying to adopt a multilateral approach, it is not easy neither quick to gather partial or total information about a single tool searching it directly from the manufacturers website or massive *pdf* files. The study of the different manufacturer's catalogues reveals lots of common points by presenting the technical information required. The pair material-operation represents the basis of the data base structure with which the software application presented is developed. Despite the heterogeneity of the catalogues formats, all the properties presented are classified in only three groups: general, geometric and mechanistic properties; the later one depending on the pair material-operation selected. The data base can contain tool references of different manufacturers for materials and operations and it is totally upgradable by the user. *SelecTool* is developed to guide the user step by step to specify the search properties. A different range of values of selected properties will modify the results that appear on screen. An important aspect supported is that the user defines the exact hierarchy with which the application searches and shows the results. Finally, the application presented is able to compare graphically the selected tools and generate other type of files for further analysis.

Keywords: Software, data base, cutting tools, MS Excel, search, select, compare, graphical comparison, reports.

1. Introduction

From the point of view of the user, it represents a big deal to select the most appropriate cutting tools from several cutting tool manufacturers and thousands of tool models. Only the data search and comparison of a small group of them usually mean lots of dedication in energy and time. Besides, an inappropriate selection can imply a substantial delay and implicit costs.

Also, many manufacturers are interested in approaching their products to their regular and potential customers by using other strategies. Many of them have already not developed it yet and they continue offering their customer service as it was ten years ago.

Inspired by the *Kendu*'s software [1], developed by *Iketek* [2], *SelecTool* helps the user from the early stages of the cutting tool selection to the last ones. It establishes a formal communication channel between the manufacturers and the customers.

2. Design

The software's design and requirements are based on the *Kendu*'s software design and capabilities [1][2][3][4]. The previous software analysis has shown specific aspects to be implemented, improved and ignored.

2.1. Design specifications

The main aspects concerning the design specifications, the requirements and terms of usage of the program are explained as follows:

- The application is designed only for information and evaluation issues. It is highly recommended to ask the manufacturer before purchasing any tool.
- The data contained in the program is strictly based on the values presented by the manufacturer in the catalogues.
- *Selectool* offers information only about cutting tools. The information about other accessories is not included. However, the data base is designed to be upgradable and so to include further information related about new models, materials or operations.
- Roughing or finishing cutting conditions are not considered directly on the program. Default cutting properties are only for roughing operations.
- Due to the awkwardness relative to the interaction tool-workpiece, *SelecTool* does not enforce any particular criteria for workpiece geometry.

- The program is scalable; making it possible to integrate other functions and capabilities than the initial one. The program code permits the upgrade of the application interface and functions.
- In the database contained in the first release, there are only two materials supported: austhenitic stainless steel *AISI316* and *Ti6Al4V*-alloy. The operations available are side milling, slotting and *3D* surface milling.
- The application needs to be installed before being run on the computer. Because of the computer requirements, this program can run on a standard PC. *SelecTool* v1.0. is only for *Windows® OS x86* and *x64* available.
- In order to generate graphical comparisons and print reports, it is necessary to install *MS Excel® 2007* or later.

2.2. Parameters

There are some common tool parameters: material, operation and type (square-end mills, ball-end mills and other). The standard, geometrical and mechanistic parameters are shown in the table below (Table 1.):

Table 1. Available parameters on the first release (milling).

Standard	Geom. Solid	Geom. Indexed	Cutting props.
Model	***Model***	***Model***	***Model***
Manufac-turer	Diameter 1	Form	***Material***
Type 1	Radius	Radius	***Operation 1***
Type 2	Diameter 2	Teeth	***Operation 2***
Refrige-ration	Teeth	Width	Feed per tooth
Coating 1	Subjection	Height	Feed per revolution
Coating 2	Helix height	Deep	Cutting speed
Price	Total height	Rake angle	Feed
	Neck height	Clearance angle	Rpm
	Radius ε	Edge length	Chip flow
	Tolerance	Subjection	
	Helix angle	Subjection diameter	
		Chip breaker	

This application orders automatically the results by the same hierarchy specified by the user. The hierarchy itself is considered as an additional parameter in the program to present the results in the way the user asks for.

It is also possible that the user knows exactly which tool model has to use, nevertheless, he ignores, for example, on which material could this tool work properly. This software is able to gather all the information requested by the reference of the searched model and present it on the screen.

2.3. Software development platform

Microsoft Visual Studio® [4][5] has been used for the development of the software tool. The *T-SQL* (*Transact - Structured Query Language*) for the data base queries has been used [6]. The *Object Oriented Programming* (*OOP*) philosophy has been employed [8].

3. Design

The developed software searches and gathers all the information from a data base by executing *SQL* queries. The data base was implemented on *Microsoft Access® 2007* and its format is *mdb*.

The data base structure is based on a series of tables whose fields correspond to the above presented parameters: *General table* with common information, *Geometrical table* (2 tables) with geometrical information and *Material-Operation table* with cutting information. Figure 1 below presents the current structure.

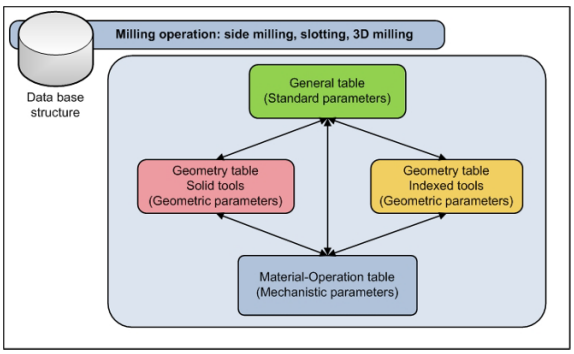

Fig. 1. Data base structure (milling).

The same data base structure is used to store information about drilling, turning, threading and other operations not available in this version yet [**9**]. Selected parameters on Table 1. mark ***identity fields*** on each data base table. New brand tool models information is processed from manufacturers' handbooks by a *MS Excel®* template to calculate exact cutting information. Later, this data is imported and added to the *MS Access®* database file. Database updates can be performed in a relative short time depending on the amount of new available tool models.

3.1. Application wizard

The task of searching tools is not a trivial one: it hides a big complexity in itself. The program has to deal with the previous experience of the user by comparing and purchasing tools [7].

In order to guide the user through the searching task, the application has a search wizard in which the user selects sequentially the parameters and its values with which to construct the appropiate *SQL* query.

3.2. User interface

The aspect of the user interface's controls is the common look of a standard application based on *Windows*®. The application's interface has been built to perform the visibility of the results giving the user a clear feedback [**7**]. Its central workspace is divided in two parts: numerical & graphical results (*left side*) and selected parameters and values information & options for graphic generation (*right side*). The different interface types *Graphic User Interface*, *Menu User Interface* and *Command User Interface* are combined for developing the software interface.

The main menu is localized above the screen. In the main menu, the complete amount of functions and options implemented in the program are ordered by common main menu elements: *File*, *Edit*, *View*, *Tools*, *Graphs*, *Windows* and *Help*. The status bar is fixed on the bottom. It gives real time feedback to the user related about the current status of the application.

All the employed interface elements are considered programming standard elements. In relation to the software's accessibility, text format and overall style keep constant and ease a comfortable reading of the results. For this version, there's no multilingual support. Hence, the interface is not customizable.

3.3. Graphics

The ability to generate graphic comparisons takes the difference within other software of the same kind. The software establishes communication with *MS Excel*® to build custom graphs [5]. Then it imports them via clipboard. Some presentation options, graphic designs and other *MS Excel*® graphical properties are available on this application.

3.4. Printing reports and file format

Sometimes dealing with big amounts of information on the screen can lead the user to confusion. Therefore this application includes a printing function based on *MS Excel*® [5].

It's possible to save the results in different file formats. Supported formats are given by *MS Excel*® itself [5], because the saving procedure is driven by this program: *xls*, *xlsx*, *txt* and etcetera. Saved files content selected parameters and specified values, all founded results, the last graphical comparison generated and the selected data to generate this last one.

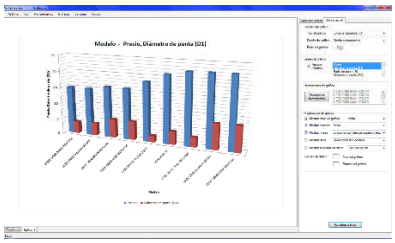

Fig. 2. Graph generation of *SelecTool* based on *MS Excel*®.

3.5. User's help

One of the most common problems on this kind of applications seems to be the lack of detailed information, examples and general user assistance. A clear and complete help form will answer the user the major part of the questions he/she has regardless of the degree of knowledge on the subject.

Furthermore, it is recommended that help is available through all the searching process so the user has full access to the help contents [9]. The overall content includes conceptual information for non-technical users.

Finally, some related links are exposed which leads the way for finding more useful information about the viewed topics.

3.6. Software update

The main feature to maintain and update is the data base inserting new models, modifying some values of existent models or deleting obsolete ones. By now, the application has the possibility of editing the data base manually. Nevertheless, it's possible to have a new release of it by simply downloading *SelecTool* from the *internet*.

Finally, the characteristics of a newer version could install updates automatically, correct and debug program exceptions, develop an own graphics engine, improve existing functions and create new ones.

4. Assessment and validation

In order to ensure the quality envisaged, *SelecTool* development process has been submitted to intensive testing, demonstrating the achievement of the major critical aspects.

Regarding the information database, the user has to choose from which database they want to get the cutting tool information. Database selection and-or modification is permitted at any time.

The user has different ways to proceed with the searching task: either by the selection wizard or by the main menu. In addition, at the beginning of the process, the user decides with which method wants to proceed: search by parameters (*default*) or by known model reference. It is possible to choose every combination and a

high range of values for the selected parameters. This aspect will obviously take to a large or a small results list. Finally, the user can specify the hierarchy or accept merely the default one (order of appearance of the parameters).

Example of tool search:

- Material: *AISI 316*
- Operation: *Milling*, *Side milling*
- Tool type: *flat-end mill*, *solid mill*
- Parameters: *Price* (0-85€), *Diameter 1* (0-16mm), *Radius* (0-8mm), *Teeth* (1-4)
- Hierarchy: *Price*, *Teeth*, *Diameter 1*, *Radius*.

The cutting tool selection steps are sequentially presented and the software permits to change the order of the parameter selection at any time. Nevertheless, it is recommended to fill all the required data before.

The search function takes proportional time to the length of the data base: a custom search in a *3000* cutting tool models data base finishes in less than *8 seconds*. Results (a total of *137 results*) are shown on screen in the same hierarchy order. The software's interface shows the results in a grid: rows are for tool models and columns for specified parameters. Number of results (rows) shown on screen is controlled by the user (*default:* all the results).

The graphical capabilities of *SelecTool* exploit the major part of *MS Excel*®'s graphical engine offering to the user different options by making custom comparisons: graph type, design (*default:* custom design) and style (*default:* style 2) are available options to be modified. Graph format can be modified by updating the current graph. It takes about *25 seconds* for every graphical generation or graphical update.

Import, export and zoom (25-800%) functions are already embedded in the application. This software could be used as a common picture viewer by importing any picture in standard image format: *bmp*, *jpg*, *png*, *tiff* and so on.

Report printing function is supported, but the printed results don't have an appropriate format to show them all.

The program gives real time feedback, accepts hotkeys and shortcuts for triggering its options and functions and help button keeps always visible and enabled.

User's help includes program functions' explanations and examples, related links and additional technical data related with the viewed topic and materials engineering. Help information is printable, but not multilingual.

5. Conclusion

Data base contents are appropriate for giving an overall view of the program's search performance; which has been constructed with the aim of being a trans-manufacturer complete portfolio. The application offers a big amount of parameters with which to complete the search task, different search methods and the chance to specify personal criteria. Elapsed search time is low and found results are coherent. Roughing and finishing cutting conditions must to be included in later versions.

The tool search shown before demonstrates an objective and custom tool searching method, always available and totally independent from any particular opinion. Unlike *Kendu*'s software [**1**], it avoids clearly some commercial issues by comparing tools from different manufacturers.

The use of *MS Excel*®'s graphics engine for graphical comparisons implies a quick development solution, but make the application rely in the dependency towards non-free software. Data transfer from the application to *MS Excel*® takes too much time and must to be reduced.

For this reason, in the first release, the printing reports function has not been completely developed, as it is envisaged to utilize a further implementation based on free software solutions. In any case, many different file formats are supported for further data manipulation with other applications.

Selectool interface demonstrates a clear appearance in relation to the presented numerical and graphical data. The selection tree indicates the user selected and non-selected parameters and values. The menu structure and right panels show any supported option or function in a logical order. By its simplicity, it promotes an intuitive and progressive learning.

The user's help form and included information is correct and very useful for experts and beginner users with technical and non-technical knowledge about material or manufacturing engineering.

Online support and update seem to be strictly necessary for newer releases of the program. This application could support scientific disclosure.

References

[1] http://www.kendu.es/ Kendu's company web site.
[2] http://www.iketek.com/ Iketek's company web site.
[3] E. Petroutsos; La Biblia de Visual Basic 2008; Ediciones Anaya Multimedia 2009.
[4] http://msdn.microsoft.com/en-us/vstudio/aa718325 MSDN - Microsoft support on Visual Studio®.
[5] B. "MrExcel" Jelen, T. Syrstad; Excel Macros y VBA, Edición revisada y actualizada 2010; Ediciones Anaya Multimedia, 2010.
[6] http://msdn.microsoft.com/en-us/library/ms189826%28v=sql.90%29.aspx MSDN – Microsoft support on T-SQL.
[7] http://www.w3.org/WAI/ - Web on standards on Accessibility
[8] I. Horton; Ivor Horton's Beginning C++: The Complete ISO/ANSI Compliant (Wrox Beginning Series); Third Edition, Appress, 2004.
[9] B. Boehm, C. Abts, A. Winsor Brown, S. Chulani, B. K. Clark, E. Horowitz, R. Madachy, D. J. Reifer, B. Steece; Software Cost Estimation with CoCoMo II; EngleWood Cliffs, Prentice Hall, 2000.

5-10

Computational fluid dynamics analysis for predicting the droplet size in MQL during grinding of super-alloy

Balan A.S.S, Vijayaraghavan L, Krishnamurthy. R
Department of Mechanical Engineering, IIT Madras Chennai, India 600036

Abstract. Increasing concerns for environmental and health hazard in processing lead a change from wet cutting to dry/near-dry cutting is highly recommended. In recent years, Minimum Quantity Lubrication (MQL) machining is regarded as a promising method for reducing machining cost by way of minimizing power,floor space and oil comsumption, while improving cutting performance; thus, it has been investigated vigorously. Very few investigations have been carried out on the influence of MQL parameters, such as oil flow rate and air pressure on droplet size and consequent perfomance.The present work aims to develop a simulation model to replicate the mist formation in MQL grinding using Fluent based Computational Fluid Dynamics (CFD) flow solver. The MQL parameters considered for the study are air pressure and the mass flow rate. Simulation of the atomization under turbulent conditions was done in Discrete Phase Model (DPM) owing to the fact that oil mass flow rates are very low and oil acts as a discrete medium in air. Droplet diameters were obtained under different inputs to find the optimum value of air pressure and mass flow rate of oil to achieve the desired results (lower cutting force and surface roughness) in MQL grinding of superalloy (Inconel 751). It is seen that medium size (around 16.3 μm) of droplet plays a sigificant role in improved performance by the way of reduction of cutting force and surface roughness.

Keywords: MQL, CFD, Droplet size, Surface roughness, cutting forces.

1. Introduction

Grinding operation, without using sufficient grinding, normally leads to thermal damages and dimensional inaccuracy on the workpiece surface. Hence methods of dry grinding have not yet been fully successful in industrial applications. Thus to avoid possible quench cracking (wet grinding) and thermal softening (dry grinding), an attractive alternative is the minimum quantity lubrication (MQL) grinding and it is referred as near dry grinding [1]. During MQL grinding, cutting fluid droplets with the gas jet dash against walls of the workpiece. When the droplets arrive at high-temperature zones, they absorb much heat and become oil vapour rapidly [2]. Tawakoli et al. [3] investigated the significance of the workpiece material hardness and grinding parameters in the MQL grinding process. Based on the results of their investigations, considerable improvement can be achieved by MQL grinding of hardened steel relative to dry grinding process. The boundary layer of air rotating with the grinding wheel can results in fluid starvation in the contact region. The boundary layer acts a barrier to fluid penetration and prevents fluid reaching the contact region and the fluid is deflected elsewhere. Such a situation is inefficient and wasteful. So the proper air supply pressure is needed for MQL grinding [4]. The main objective of this work is to simulate the atomization of oil mist using Computational Fluid Dynamics (CFD) model using Fluent 6.3 flow solver. The parameters varied being the air pressure and the mass flow rate. Simulation of the atomization under turbulent conditions was done in discrete phase model (DPM). Sauter Mean Diameter (SMD) is most widely used in these types of models where aerosol sprays are simulated. SMD is defined as the diameter of a spherical droplet which has same ratio of surface area/volume as that of the whole spray. A 2D numerical discrete phase simulation has been developed to study the droplet diameters under different inputs conditions to find the optimum value of air pressure and mass flow rate of oil to achieve the best results in MQL grinding of INCONEL 751 superalloy.

2. Experimentation

Straight surface grinding experiments were carried out on Inconel 751 super alloy with resin bonded diamond wheel. The schematic of the experimental setup is shown in Fig. 1. The details of machining parameters and the grinding wheel specification used in this present study are summarized in Table 1. In this MQL system, the compressed air (pressure) and lubricant flow rate can be adjusted separately and mixed in the special nozzle- (air atomizer) to make micro droplets of cutting oil jetting to the cutting zone by the compressed air.

Table 1 Experimental conditions

Parameters	Conditions
Grinding Machine	Tool and cutter grinder (schuette make)
Grinding wheel	D126 C75 (resin bonded Diamond wheel of 150 mm diameter; 13 mm width; grit size 126)
Wheel velocity (V_s)	2826 m/min
Work feed rate (V_w)	0.9 m/min
Depths of cut (a)	30 µm
MQL oil flow rate (Q)	60, 80 ,100 ml/hr
Air pressure(P)	2, 4 , 6 bar
MQL oil	Cimtech D14 MQL oil with viscosity =5 cst, and ρ= 1080 kg/m3

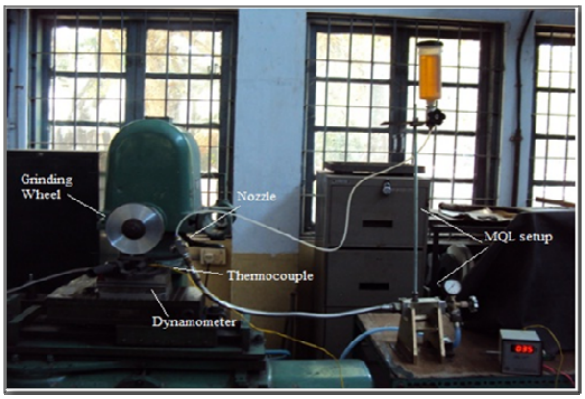

Fig. 1. Experimental Setup.

The workpiece was mounted on a three component piezoelectric dynamometer (Make: Kistler, Model: 9265A) in order to monitor both the tangential (F_x) and normal (F_z) components of grinding force. Temperature at the tool-work interface was measured using a k-type (Chromel / Alumel) thermocouple. . Surface finish of the machined surface was measured using a Talysurf CCI - Lite Non-contact 3D Profiler.

3. Experimentation

A 2D CFD simulations were performed with ANSYS FLUENT version 6.3. Air atomizer geometry was modeled and meshed using GAMBIT 2.3. Size functions were used to further reduce mesh size. The air phase and particle tracking were performed in steady state. The compressed air and oil (cutting fluid) were set as the primary and secondary phase, respectively. Throughout all simulations the Realizable $k-\varepsilon$ model and Discrete Phase model (DPM) were used for oil mist formation. FLUENT simulate the discrete second phase in a Lagrangian frame of reference. This second phase consists of spherical particles which may be taken to represent droplets of oil dispersed in the continuous phase. FLUENT computes the trajectories of the droplets by solving the time-averaged Navier-Stokes equations for air, while the oil droplets is solved by tracking a large number of droplets through the calculated flow field. A fundamental assumption made in this model is that the dispersed second phase occupies a low volume fraction, that perfectly fits the model of MQL in which the mass flow rates are of the order of micro liters. The governing equations for mass and momentum for the present model can be shown in tensor form as

$$\frac{\partial p}{\partial t}+\Delta(\rho\vec{v})=0 \tag{1}$$

$$\frac{\partial}{\partial t}+(\rho\vec{v})+\Delta(\rho\vec{v}\vec{v})=-\Delta p+\Delta(\bar{\bar{\tau}})+\rho\vec{g}+\vec{F} \tag{2}$$

4. Geometry and boundary conditions

According to the structure of nozzle and spray characteristic, the model of simulation was built in 2D for computational simplification. The boundary conditions for different regions were decided based on the constant inputs that were given for that particular region. Figure 2 shows different boundary conditions and geometry of the model.

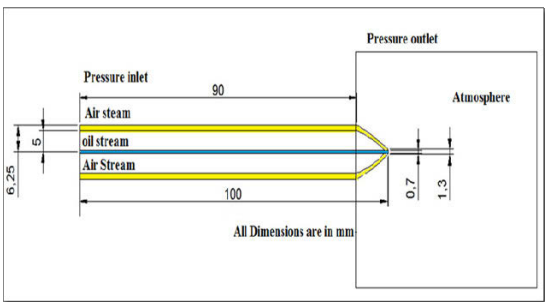

Fig. 2. Geometry and boundary conditions

The air stream input boundary was selected as 'pressure inlet' owing to the fact that air is supplied at constant pressure from that boundary. Similarly oil stream input and boundaries of wall were selected as mass flow inlet and pressure outlet respectively. Different domains such as air/oil streams, mixing area, nozzle outlet were separated using 'interior' boundary condition.

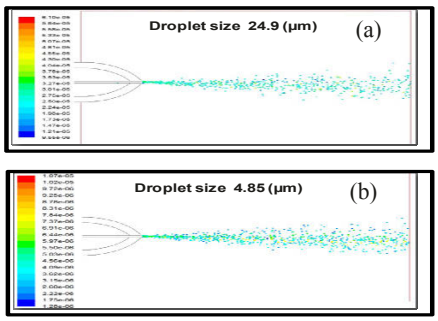

Fig. 3. Contours of (a) Maximum and (b) Minimum Droplet size

5. Results and discussion

5.1. MQL droplet size prediction

The three levels for the two input conditions (air pressure and mass flow rate) were used to create simulation results for all the possible combinations (full factorial experiment). The standoff distance is considered to be constant for all the case. Summary after post processing for DPM was obtained for all the simulations. Sauter Mean Diameter (SMD) was taken and tabulated in Table 2.

Table 2. SMD values for Simulated and experimental conditions

Pressure (bar)	Flow rate (ml/hr)	Simulated SMD (μm)	Experimental SMD (μm)
2	60	24.9	23.7
2	80	14.2	12.9
2	100	8.1	7
4	60	20	18.3
4	80	9.3	7.5
4	100	6.6	4
6	60	18.3	16.3
6	80	8.23	6.8
6	100	4.85	2

In two-phase (gas-liquid) jet of MQL, droplet characteristics are mostly affected by the primaryphase (compressed air). Increase in the air supply pressure and mass flow rate leads to a decrease in droplet size. Larger droplet size with high pressure can easily penetrate the boundary layer to lubricate the grinding zone effectively and this can be achieved when the oil mist velocity is substantially greater than the tangential velocity of the wheel. The maximum droplet size of (24.9μm) was found in the case of 2 bar air pressure and 60 ml/hr mass flow rate whereas, the minimum droplet size (4.85μm-Fig. 3) was found in the case of 6 bar air pressure and 100 ml/hr.

5.2. Experimental validation

The Malvern Analyzer (manufactured by Malvern Instruments, England) was used to measure the exact droplet size. The Setup of the Malvern Analyzer is shown in Fig. 4. It is rapid, nondestructive and requires no external calibration. The extremely fast, 10 KHz, data acquisition rate of the new system produces real-time particle size distributions with a 100 microsecond resolution.

Fig. 4. Malvern Analyzer (Malvern Instruments, England)

The Sauter Mean Diameter for different MQL conditions was measured and tabulated in table 1.2. The experiments were repeated to check the repeatability. The comparisons between numerical and experimental data of droplets were carried out and it is shown in Fig. 5. The numerically simulated values are matching with experimental values at lower and medium mass flow rate. At higher mass flow rate and air pressure of (4 & 6 bar), the predicted Sauter Mean Diameter is higher.

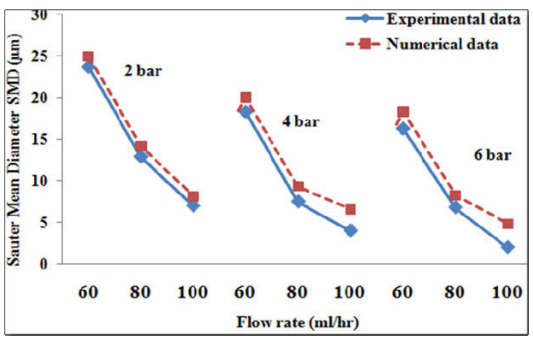

Fig. 5. Comparison of numerical vs. Experimental data

5.3. Effect of droplet diameter on grinding performance

Grinding experiments have been performed in different MQL oil flow rates and air pressures with maximum cutting velocity (V_s= 2826 m/min), feed rate (V_w=0.9m/min) and depth of cut (a=30 μm). Fig. 6 illustrates the significance of Droplet size on grinding force components, surface roughness and temperature. As the droplet size increases, there was a steep rise in the normal force and then tends to decrease gradually up to 16.3 μm droplet size and then increases drastically. The

same trend was observed with surface roughness. The diameter of an oil droplet has the most significant influence on the relative flight distance and is proportional to the square of the diameter, it is very difficult for a very small oil droplet to move freely in the air flow [5]. So it can easily changes its track away due to the cutting velocity and then leading to insufficinent lubrication condition with higher normal force and poor finish. Larger droplet with lower pressure also leads to insufficinent lubrication, owing to the fact that cannot be carried to the grinding zone because of its higher mass. Therefore medium size droplet with higher pressure can easily penetrate the boundary layer and provide effective lubrication, thereby reducing the normal force, temperature and surface roughness. This phenomenon occurs due to the reduction in the sliding friction of grinding and the adhesion of the chip on the rake face of the grit (loading). As the lubrication effect (film forming tendency) increases, the energy formation of the work material drops down (due to Rehbinder effect) facilitating elastic–plastic deformation under the cutting edge of the abrasive grain, resulting in reduction of cutting forces [6]. The function of the high cooling air is to flush away the chips from the cutting zone (flushing effect) and maintain a clean cutting edge, which in turn reduces the surface roughness. There is no variation in the tangential force between (7.5 -16.3 μm) droplet size because of effective lubrication. The temperature in the cutting zone decrease with decreasing droplet size. This is due to both the cooling and the lubrication effects of the fluid provided by MQL, as lubrication reduces the cutting forces and cutting energy, while convection heat transfer and/or boiling carries away some of the heat from the cutting zone. From the results it is clearly seen that the droplets ranging from (7.5 -16.3 μm) gives effective lubrication, while grinding of Inconel 751 superalloy.

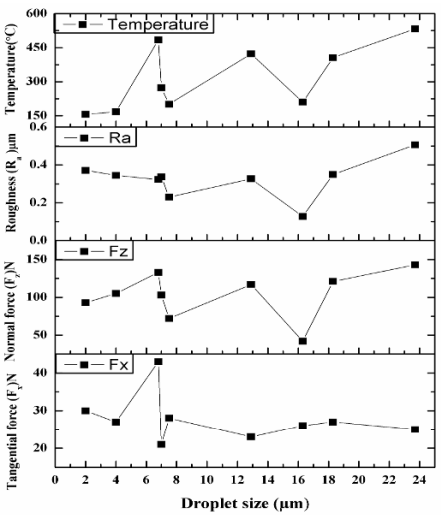

Fig. 6. Effect of droplet size on Cutting force, Surface roughness and Temperature

6. Conclusions

The potential of the numerical modeling combined with the experimental results is used as a powerful tool to obtain a better understanding of the phenomena observed during the MQL grinding of Inconel 751 alloy and to analyze the influence of droplet size on grinding performance. The significant findings derived from this work are summarized below.

- Droplet size plays a key role in MQL grinding. Medium droplet sizes with higher pressure can easily penetrate the boundary layer to lubricate the grinding zone effectively.
- The numerically simulated values are matching with experimental values at lower and medium mass flow rate at various air pressure.
- Effective transportation of the droplets to the grinding zone, enhance boundary lubrication environment that develops around the wheel-work interface, which enhances to better grinding performance.
- The droplets ranging from (7.5 -16.3 μm) give effective lubrication that reduces normal force, and surface roughness values.

Acknowledgements: Authors want to express their sincere gratitude to Tamal Mukherjee, Application Specialist, Malvern - Aimil Application Lab for providing the Malvern Analyzer used in this work.

References

[1] Malkin S (2008) Grinding Technology, Theory and Applications of Machining with Abrasives, second ed., Industrial Press Inc.

[2] Silva R, Bianchi EC, Fusse RY, Catai RE, Franca TV, Aguiar PR, (2007) Analysis of surface integrity for minimum quantity lubricant–MQL in grinding , International Journal of Machine Tools & Manufacturing,47;412–418.

[3] Tawakoli T, Hadad MJ, Sadeghi MH, Daneshi A, Stockert S, Rasifard A,(2009) An experimental investigation of the effects of workpiece and grinding parameters on minimum quantity lubrication–MQL grinding, International Journal of Machine Tools & Manufacturing,49;924–932.

[4] Wu1 H, Morgan MN, and Lin B, (2009), Investigation of the Grinding Wheel Air Boundary Layer Flow, Advanced Materials Research,76-78;113-118.

[5] Brinksmeier E, Heinzel C, Wittmann M, 1999, Friction cooling and lubrication in grinding, CIRP Annuals. Manufacturing Technology, 48; 581–598.

[6] Obikawa T, Asano Y and Kamata Y, (2009), Computer fluid dynamics analysis for efficient spraying of oil mist in finish-turning of Inconel 718, International Journal of Machine Tools & Manufacture, 49; 971–978.

5-11

Cryogenic CNC machining of individualised packaging

V.G. Dhokia[1], A.Nassehi[1], S.A.Wolf[1,2] and S.T.Newman[1]
[1] Department of Mechanical Engineering, University of Bath, UK, BA2 7AY
[2] WZL, RWTH Aachen, Manfred-Weck Haus, 52056 Aachen, Germany

Abstract. With the continuing growth in the high value product manufacturing sector there is a need to provide new ways to store and transport high value precision parts without damage and contamination. Traditional packaging is produced from foams and elastomers using forming techniques. This provides difficulty for producing individualised packaging solutions as individual moulds and forming tools would be required. In addition present solutions do not provide adequate packaging as they can cause damage to the part in some cases. This paper explores the design and manufacture of precision machined individualised neoprene foam packaging using cryogenic CNC machining technology. Cryogenic CNC machining is discussed and an example case study is presented showing the viability and efficacy of the proposed design and manufacturing method.

Keywords: Cryogenic, CNC, Packaging

1. Introduction

Packaging is a major issue for a variety of different industrial and consumer based products. The fundamental aim is to prevent damage and part contamination during storage and transportation. Current methods primarily consist of forming technologies such as thermoforming to produce the required geometrically accurate packaging. For lower value products, simple, cut to fit foam inserts, polystyrene, and bubble wrap packaging is used and this can in a number of cases prove to be inadequate. Producing specific packaging using current methods is difficult as individual moulds are required, which subsequently leads to increased cost and manufacturing process chain. Figure 1 shows an example of a soft foam package.

Fig. 1. Soft material packaging example for mass produced parts

Correct packaging is vital, particularly if parts are being sent to customers as replacement or as a consignment of 'bits' for onsite assembly. It is also useful when parts need to be transported for further processing. In addition, as these types of parts are often expensive, packaging takes on added significance, not only for product security against damage, but also from a business perspective. A well-packaged part is likely to procure added enhancement to the product, thus increasing its customer appeal and value. For example, perfume packaging can represent 22% of the manufacturer's gross costs and can contribute up to 40% of the value of the product [1]. It is not merely the case that a product or part should be stored or transported in adequate standardised packaging, particular if the part being packaged is of high value.

A process being pioneered at the University of Bath is that of direct cryogenic CNC machining of soft polymers [2, 3]. Using this process it becomes possible to produce product specific packaging that can be directly machined from different materials depending on the end application and on the amount of part protection required. This paper illustrates the concept through a case study for design and manufacture of individualized packaging for specialist bicycle parts.

2. Cryogenic CNC machining of elastomers

The concept of soft elastomeric material machining is based on the need to remove the moulding process, which can be expensive and does not allow for constant design change and inhibits customised and individualised design [4, 5]. Direct CNC machining of polymers provides the ability to change designs instantaneously emphasizing the realistic opportunity to produce individualised product packaging. However the major challenge of machining polymers and soft elastomeric materials is the inability to conventionally impart a sufficient chip bending moment, which can result in significant deformation, tearing and burning of the material. Figure 2 presents example images of different machining conditions for soft

materials. The first image is captured from dry machining and it is clear to see the tearing and serration marks imparted on the material. The second image illustrates a chip sample from cryogenic machining of neoprene foam and it is clear to see the clean-cut edges and full chip formation, indicating a significantly improved machined part and surface.

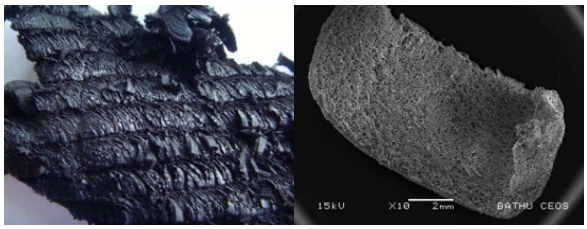

Fig. 2. Surface from dry machined rubber and a fully formed chip from cryogenically machined neoprene

The cryogenic CNC machining facility [2] has been designed to machine a range of soft elastomer materials, which include, neoprene foam and ethylene vinyl acetate (EVA). The major aim of the cryogenic CNC machining process is to freeze a soft material to below its glass transition temperature (T_g) value and then to directly machine it using standard conventional CNC machine tools and tooling. The T_g is the temperature at which a material shows similarities to that of a glass type structure. Only after this temperature has been achieved and is maintained can the material be successfully machined. Each material has its own T_g value, which is determined using dynamic mechanical thermal analysis methods (DMTA) [6]. Machining above this temperature can lead to deformed features and material tearing as illustrated in Fig. 2 leading to inferior parts, products and potentially reduced tool life.

The cryogenic CNC machining facility consists of a cryogenic fixture designed to securely clamp a test part sample, an 18mm diameter vacuum jacketed piping that feeds directly from a 180-litre high pressure Dewar into a custom designed fixture and a multi nozzle spray jet unit. The temperature of the fixture is monitored using a series of low temperature thermal probes. The material block is securely located inside the fixture and is cooled directly using liquid nitrogen (LN_2), with the use of the spray jet unit. The spray jet unit activates using a timer mechanism, so as to regulate the amount of LN_2 used during a given machining cycle. Fig. 3 provides a schematic of the cryogenic machining setup.

The developed cryogenic CNC machining facility is designed to be retrofitted to any type of vertical machining centre. The control unit for controlling the rate of flow of LN_2 at any given time in the machining process is totally independent of the machine tool and was developed as part of another study [4]. This is a timer-based system that uses the time taken to achieve the material specific T_g and the time taken to maintain this T_g as the input factors.

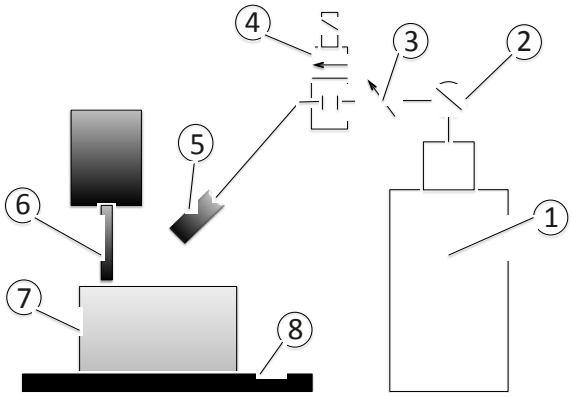

Fig. 3. Schematic setup for cryogenic machining, 1-Liquid nitrogen Dewar, 2- pressure gauge, 3- gate valve, 4- solenoid on/off valve, 5- specially designed nozzle, 6- cutting tool, 7- workpiece, 8- machine table

3. Individualised packaging design

There are different types of packaging solutions that can be used depending on the part / product required to be packaged, transported and or stored. Mass produced products typically tend to use thermoformed packaging manufactured using specifically designed mould tools and soft low-density, impact attenuating materials. The following Fig. 4 illustrates an example of the current method for mass produced packaging.

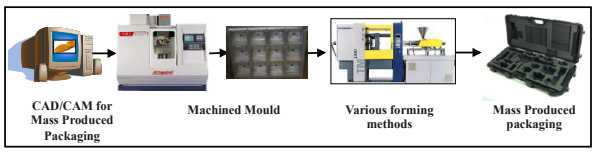

Fig. 4. Mass produced packaging

The design of individualised packaging requires a totally new approach. In order to produce the correct packaging geometry a CAD representation of the part is required. This can be either obtained from the CAD part file or from using scanning reverse engineering techniques to produce an accurate 3D digital representation of the part features and geometry. Using the CAD part, fully individual male type negative moulds of the part can be replicated. In addition, these computer-generated designs can then be altered, adjusted and manipulated to increase packaging support for the part and part numbers corresponding to the part can be engraved directly into the material.

Using the generated packaging design moulds CAM techniques can be used to generate the machine specific CNC code. The Cryogenic CNC machining process can then be used to freeze the material and machine the required packaging from a variety of different soft materials, which depend on the end application and on the amount of material support required for the part.

4. Methodology

The methodology for designing and manufacturing of a fully individual product packaging solution consists of using scanning technology to capture the part geometrical information and then using the developed cryogenic CNC machining technology to produce the required packaging. The methodology used for the individualised packaging is shown in Fig. 5 through an IDEF0 representation. The three main areas for producing a fully individualized soft material package consist of scanning, designing and CNC machining. The scanning output is a point cloud of the part data, which can be meshed together. The output of the design phase is the mould packaging design and the output from the third phase is the individualised packaging solution.

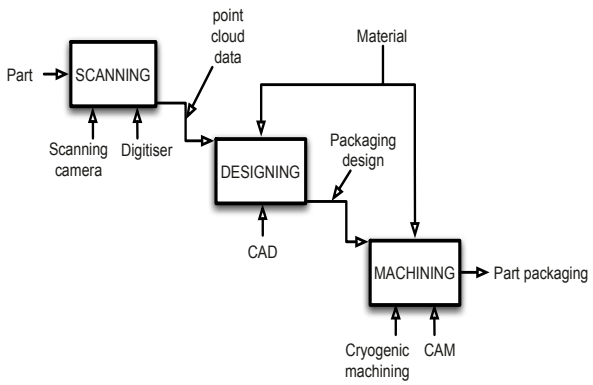

Fig. 5. IDEF0 representation of the methodology

4.1. Case study and results

In order to demonstrate the efficacy of the developed cryogenic CNC machining process and the individualised packaging design a case study example was developed and tested for a high value product.

Moulten Bicycles based in the UK are a company that specialize in hand made custom bicycles retailing in the price range of £9000 to £14000 [7]. A handle bar holder was chosen as the case study example, as this part requires safe damage free transportation around the production site for different manufacturing and finishing operations. In addition, this part is often sent to the customer directly as part of a consignment of bits to be assembled by the customer or as a replacement part. Fig. 6 illustrates an example of the bicycle and handle bar holder that is used as the case study example.

The process for designing of the product specific packaging first begins with capturing of the part data digitally. The handle bar holder is scanned using a 3D laser-stripe non-contact scanner to capture the complete geometry of the part in the form of a digitised point cloud. The part requires two scans, which are then meshed together. The density of the point cloud is controlled so as not to capture large amounts of redundant points, which would increase the processing and design time. The orientation of the part throughout the scanning process is critical in order to capture all the necessary data. Anomalous data, captured from the scanning, such as background points can be filtered out and removed in the design process. The point cloud data is converted into curves and surfaces and this provides a functional CAD model with which to design the part packaging around. Fig. 7 shows the scanned part and the final CAD model of the part.

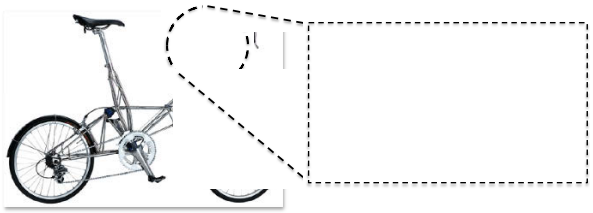

Fig. 6. The Moulten bicycle and the case study part

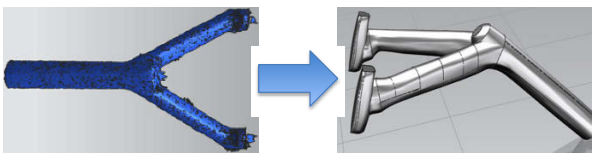

Fig. 7. Digitised part and full CAD part

The part packaging solution is then designed and in this case a sandwich type configuration is used in order to encapsulate the part in the central sections. This provides full part protection. For this particular case study the part is located centrally so as the degree of impact resistance is consistent around the part. Also, as the part has two additional assembly items, these are positioned within the complete handle bar holder packaging solution. Figure 8 illustrates an example of the designed packaging.

Fig. 8. The CAD packaging design

Using the cryogenic CNC machining facility and the correct material dependent machining parameters each segment of the package is machined. Tooling is selected based on the geometry, required feature size and generated process plans. The machining strategies are also devised based on the material properties and the complexity of the part.

Figure 9 depicts the finished neoprene foam packaging solution for the Moulten Bicycle handle bar.

Fig. 9. The final machine packaging

5. Conclusions

This paper has illustrated and demonstrated a totally new process for rapidly machining elastomeric material on conventional CNC machine tools using liquid nitrogen freezing technology. The concept of individualised packaging is discussed and an example case study is presented and machined using the cryogenic CNC machining process. Using this type of design and manufacturing process it makes it increasingly cost effective and efficient to produce high quality precision machined packaging for bespoke and high value products and parts.

References

[1] Poor packaging design adding to industry footprint. http://envirowise.wrap.org.uk. [Web page] 2011 31/01/2012].

[2] Dhokia V.G., Newman S.T., Crabtree P. and Ansell M.P., (2011), Adiabatic shear band formation as a result of cryogenic CNC machining of elastomers. Proceedings of the Institution of Mechanical Engineers Part B-Journal of Engineering Manufacture. 225(B9): 1482-1492.

[3] Dhokia V. G., Newman S. T., Crabtree P. and Ansell M. P., (2010), A methodology for the determination of foamed polymer contraction rates as a result of cryogenic CNC machining. Robotics and Computer-Integrated Manufacturing. 26(6): 665-670.

[4] Dhokia V.G., Newman S.T., Crabtree P. and M.P. Ansell, (2011), A process control system for cryogenic CNC elastomer machining. Robotics and Computer-Integrated Manufacturing. 27(4): 779-784.

[5] Dhokia V.G., Crabtree P., Newman S.T., M.P. Ansell and R.D. Allen. (2009), Rapid craft CNC machining of personalsied orthotic insoles for medical and sporting applications. in Asia-Pacific Conference on Sports Technology. Hawaii, USA.

[6] Herzog B., Gardner DJ., Lopez-Anido R. and Goodell B., (2005), Glass-transition temperature based on dynamic mechanical thermal analysis techniques as an indicator of the adhesive performance of vinyl ester resin. Journal of Applied Polymer Science. 97: 2221-2229.

[7] Company Moulten Bicycle. [cited 2012 20/01/2012]; Available from: http://www.moultenbicycles.co.uk.

5-12

Modeling and simulation of shot peening process

X J Zhang [1], J B Wang [1], A Levers [2] and K K B Hon [3]
[1] School of Mechanical Engineering, Northwestern Polytechnical University, Xi'an, Shaanxi 710072, China
[2] School of Applied Sciences, Cranfield University, Cranfield, Bedfordshire MK43 0AL, UK
[3] School of Engineering, University of Liverpool, Liverpool L69 3GH, UK,

Abstract. Shot peening is a widely used mechanical surface processing method for fatigue strength enhancement. It is a complex process as multiple nonlinear factors are involved. In this paper, a novel method is presented to model and simulate shot peening process in 3D system. Workpieces and tools were modelled in 3D system to simulate the dynamic characteristics of the shot peening process. A vectorial routing method was introduced to define the movement of nozzles in 3D space. Shot peening impacts over the surface of the specimen was simulated with a segmented field function. The deformation of specimen was simulated instantaneously with a combined analytical/numerical method by dividing the shot peened area of the specimen into segments according to the segmented field function of coverage. Verification of simulation results by shot peening experiments showed that this approach could facilitate process design and predict operational behaviours.

Keywords: modeling, simulation, shot peening

1. Introduction

Shot peening is a widely used mechanical surface processing method in forming of large scale thin component for its fatigue strength enhancement and low cost. However, it is difficult to model and simulate the shot peening process because the final state of the workpiece is the summative result of a large amount of elasto-plastic impacts on the surface.

Numerical methods have been used effectively for modeling and simulation of shot peening process. A direct way is to simulate the impacts against the workpiece surface one by one incrementally.

Meguid et al. [1] modeled and simulated the single and twin spherical indentations using the finite element (FE) method. Majzoobi et al. [2] obtained the compressive residual stress profiles introduced in the shot peening process by modeling and simulating multiple shot impacts on a target plate at different velocities.

However, it is impossible to model and simulate the shot impacts over the whole surface of a large scale thin workpiece because very fine mesh is required which makes the numerical model too large in size to be solved efficiently.

Indirect methods, i.e. equivalent loads of the shot impact action on the target show efficiency at reducing the problem size of the numerical models of the shot peening process.

Wang [3] applied pre-stresses and pre-strains to layers of the static finite element model to reduce the problem size. Gardiner and Platts [4] proposed to simulate the action of the residual stresses on large surface areas by imposing some level of prestress on the part. Levers and Prior [5] simulated the effect of peening on large flexible panels by applying varying thermal load to section points through the thickness. Homer and VanLuchene [6] introduced equivalent stretching and bending loads to element nodes to simulate the shot peening effect on the shot peened structures with the FE method.

In this paper, a novel combined analytical/numerical method of modeling and simulation of single-sided shot peening process in 3D space is investigated. An analytical loading model is built based on the concept of linear density of indentations. An equivalent loading method is proposed by scheduling the shot peening process with vectorial routing method and dividing the routes into segmented strips. FE models are built to simulate the deformation of large scale thin component in 3D space based on narrow strip shot peening experiments.

2. Models of shot peening routes and coverage

2.1. Vectorial shot peening routing method

In a typical system for shot peening large scale thin components, the workpiece mounted on the fixture of the shot peening machine moves relatively to the nozzles in 3D space. The projection of the relative motion path of the nozzles on the plane of the workpiece forms a series of routes which indicates the shot peening routes of the

process. Therefore, the shot peening routes can be defined with a series of data sets $\boldsymbol{A}^i$ as follows:

$$\boldsymbol{A}^i = \left(\vec{\boldsymbol{Q}}^i, \vec{\boldsymbol{Q}}^{i+1}, \overrightarrow{\boldsymbol{Vec}}^i, v^i, sta^i\right) \tag{1}$$

where $\boldsymbol{A}^i$ defines the i^{th} data set of the shot peening routes; $\vec{\boldsymbol{Q}}^i$ and $\vec{\boldsymbol{Q}}^{i+1}$, define the starting point and terminal point of the relative motion; $\overrightarrow{\boldsymbol{Vec}}^i$ is a unit vector indicating the direction of the relative motion; v^i is a scalar that defines the relative speed of the motion; and sta^i is a status variable indicating whether there is a shot flow or not: if $sta^i = 0$, there is no shot flow; else if $sta^i = 1$, there is a shot flow.

Consequently, the shot peening routes of the process for a workpiece in a simulation system are defined by a series of vectorial data sets $\boldsymbol{A}^i$.

2.2. Segmented field function model of coverage

Assuming the nozzles are perpendicular to the surface of the workpiece, the relationship between the width of the shot peened strip and the parameters of the nozzle can be formulated as,

$$r_c = kr_n + kd_n \tan\alpha \tag{2}$$

where r_c is the width of the shot peening strip, k is the number of nozzles, r_n the radius of the nozzle, d_n the distance of the outlet of nozzle to the surface of the shot peened surface, and α the scattering angle of shot flow.

Assuming the distribution of the shot peened indentations is uniform, when the shot flow is given, i.e. the number of shots from the nozzle per minute, the number of indentations covered by unit length in the shot peened area, namely, linear density of indentations is given in equation. 3:

$$c_l = \sqrt{1/\left[r_c\left(v/f_s + \xi\right)\right]} \tag{3}$$

where c_l is the linear density of indentations, ξ a compensational factor for saturated shot peening condition.

The linear density of shots on the i^{th} segment of the shot peening routes can be given by a segmented field function as

$$c_l(x,y) = c_l^i\left(x_{Q^i}, y_{Q^i}\right) = 10^4\sqrt{6f_s^i/\left(\pi\rho v_n^i r_c^i d^3\right)} \tag{4}$$

when,

$$(x,y) = \left(x_{Q^i}, y_{Q^i}\right) + \lambda^i\overrightarrow{\boldsymbol{Vec}}^i + \eta^i\overrightarrow{\boldsymbol{Vec}}^i \cdot \begin{bmatrix} 0 & 1 \\ -1 & 0 \end{bmatrix} \tag{5-1}$$

$$\lambda^i \in \left[0 \left\|\vec{\boldsymbol{Q}}^{i+1} - \vec{\boldsymbol{Q}}^i\right\|\right],\ \eta^i \in \left[-r_c/2, r_c/2\right] \tag{5-2}$$

where f_s^i is the flow of shots on the i^{th} segment of the shot peening route, v_n^i the speed of nozzles, r_c^i the width of the shot peened strip.

3. Combined analytical/numerical method

3.1. Analytical representation of shot peening loads

Assuming a cylindrical coordinate system $o\rho z$ on the cross section of an indentation, the bending moment $\bar{M}$ introduced by the compressive residual stresses to a line with a depth of δ can be expressed approximately as

$$\bar{M} = \int_{-W/2}^{W/2}\int_0^T \sigma_\rho\left(\delta - z\right)\mathrm{d}l\mathrm{d}z \tag{6}$$

Consider an array of indentations distributed along a line AB in the shot peened area, the bending moment to introduced by the residual stresses of the indentations covered by the line AB can be formulated as follows

$$M \cong n\bar{M} \tag{7}$$

where n is the equivalent number of the indentations cut across by the line AB.

3.2. Finite element simulation of shot peening

Analytical equivalent bending loads were first determined with narrow strip single-sided shot peening experiments and then applied in the FE models.

2024T351 aluminum alloy specimens, with sizes of 0.40m(length)*0.20m(width)*0.008m (thickness), were used in the experiments with a narrow shot peened strip covering along the symmetrical line of each specimen as depicted in Fig. 1. The specimens were shot peened on a pneumatic shot peening machine with five different feed rates: 0.5m/min, 1.0m/min, 2.0 m/min, 3.0 m/min, 5.0 m/min, and 8.0 m/min while the other shot peening parameters were kept at: shot peening distance 0.30m, shot peening air pressure 0.40MPa, shot flow 6kg/min, and shot type ASH660.

The equivalent bending moment for the action of the indentations on the shot peened specimen is calculated through the following formula

$$M^* \cong D^* l/r \tag{8}$$

where D^* is the equivalent rotational inertia corresponding to the loading moment applied to the specimen in FE model as shown in Fig. 2.

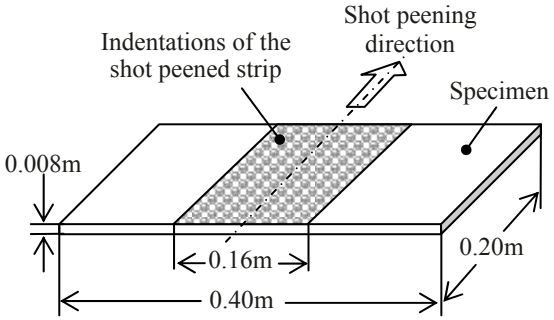

Fig. 1. Schematic diagram of narrow strip shot peening of the specimen

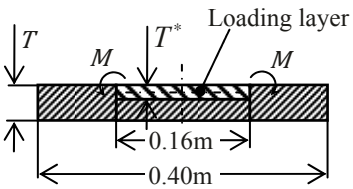

Fig. 2. Cross section of loading layer and the specimen in FE model. The loading layer corresponds to the compressive layer, which deforms the specimen, of the shot peened strip of the specimen.

Two different FE models of the shot peening process are built with Abaqus/Standard procedure: a verification model and a process model. Linear quadrilateral shell element S4 with five integration points in thickness is adopted in both models.

The verification FE model, the cross section of which is shown in Fig. 2, is built to verify the validity of the modeling method. The thickness of the loading layer T^* is assigned 0.002m for the model, and the equivalent bending moments applied to the edges of the loading layer in the lateral direction are calculated with Eq. (8) as 717.70 Nm, 584.49 Nm, 490.01 Nm, 452.30 Nm, 408.91 Nm, and 248.95 Nm corresponding to the respective feed rates.

The process FE model is built to simulate the deformation of the shot peened workpiece in 3D space. The shot peening pattern of the FE model corresponding to the defined shot peening routes is shown in Fig. 3. Equivalent bending moments corresponding to various feed rates of the shot peening routes are applied to the FE model via loading layer along the shot peened strips. Three cross section lines U_1U_2, U_3U_4, and U_5U_6 as illustrated in Fig. 3, are deployed to examine the deformation of the workpiece in the simulation.

The material of the specimens and the workpiece is aluminum alloy 2024T351 with Young's modulus $6.8\text{x}10^{10}$Pa, Poisson's ratio 0.3, and mass density $2.8\text{x}10^{3}$Kg/m^3.

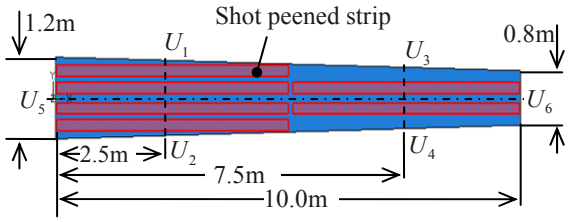

Fig. 3. Shot peening pattern of the FE model of the workpiece

4. Results and discussion

4.1. Verification experiments

The bending radii of the shot peened specimens in experiments and simulation are plotted against the feed rate as shown in Fig. 4. The maximum tolerance of the radii obtained from simulation compared with those obtained from experiments is no more than -11.4%.

4.2. Simulation of large scale thin workpiece

The deformed shape of the workpiece in 3D space under the action of the shot peening strips is given schematically in Fig. 5 with a contoured distribution of Von Mises stresses of the shot peened surface. The distribution of the stresses indicates that while higher lever stresses are introduced in the area of the shot peened strips, lower lever stresses or deformation are resulted in the non-shot-peened area because of the radial action of the residual stresses introduced by shot peening.

The deflection radius of the cross section curve U_1U_2 and U_3U_4 are plotted against the normalized point position measured from U_1 and U_3 respectively as shown in Fig. 6.

The distribution of the deflection radius along the cross section curves U_1U_2 and U_3U_4 shows that the shot peening strips deform the workpiece mainly at the shot peened area although related deformation is introduced in the surrounding non-shot-peened area.

Deflection in the longitudinal direction along the mid-cross section curve U_5U_6 is observed as well with a value of 338.44mm and an arc length of 71.04mm. The distribution of deflection radius is plotted against the normalized point position along the curve U_5U_6 measured from U_5 as given in Fig. 7.

Figure 7 shows that the deflection radius along the longitudinal mid-cross section curve U_5U_6 are generally more than 10 times larger than those along the lateral curves that covered by the shot peened strips. The reason is that the non-shot-peened area, which reduces the linear density of shot peened indentations n/l as defined in Eq. (11), resists the bending deformation of the workpiece in the longitudinal direction.

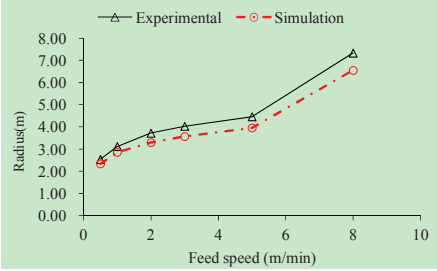

Fig. 4. Bending radius of the specimens versus feed speed.

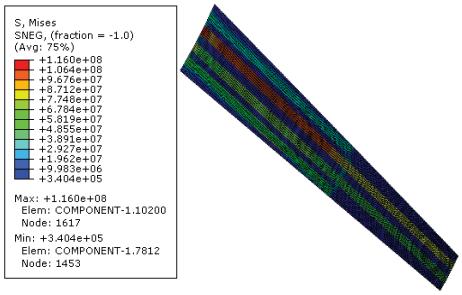

Fig. 5. Deformed workpiece in 3D space

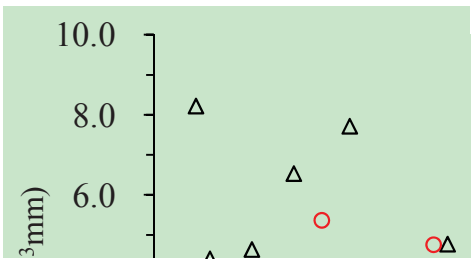

Fig. 6. Deflection radius versus normalized point positon along cross section curve U_1U_2 and U_3U_4.

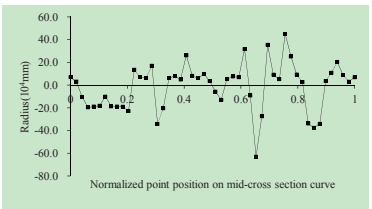

Fig. 7. Deflection radius versus normalized point positon along mid-cross section curve U_5U_6

4.3. Time efficiency

The problem size of the FE model of the workpiece shown in Fig. 3 is 14709 4-node shell elements with 15856 nodes, which took a total CPU time of 753.30 seconds and a memory of 114 Mbytes to solve the problem on a personal computer with an Intel Core Duo CPU of 2.4GHz. Therefore, it is a time-efficient way of simulating the shot peening process with the analytical/numerical method.

5. Conclusions

A novel analytical/numerical method of modeling and simulation of single-sided shot peening process is proposed by combining analytical formulation of bending moment based on the concept of linear denstiy of shot-impact indentations and applying bending loads via loading layer strips. The main conclusions are summarised as; Vectorial shot peening routing method defines the feed rates of each segment of shot peening route, which provides auxiliary information for the design of shot peening strips. Segmented shot peened strips covered with uniform distribution of impacted indentations forms an equivalent uniform bending moment applied to the edges of the strips under small deformation condition. The combined analytical/numerical method is demonstrated as time efficient in modeling and simulation of the deformation of sigle-sided shot peened large scale thin workpiece.

References

[1] Meguid, S., Shuagal, G., Stranart, J. and Daly, J. 1999. Three-dimensional dynamic finite element analysis of shot-peening induced residual stresses. Finite Elements in Analysis and Design, 31:179-191.

[2] Majzoobi, G., Azizi, R. and Alavi Nia, A. 2005. A three-dimensional simulation of shot peening process using multiple shot impacts. Jour. Materials Processing Technology, 164-165:1226-1234.

[3] Wang, T. 2003. Numerical simulation and optimisation for shot peen forming processes. PhD Thesis, University of Cambridge.

[4] Gardnier, D. and Platts, M. 1999 Towards peen forming process optimisation. ICSP-7. Warsaw, Poland.

[5] Levers, A. and Prior, A. 1998. Finite element analysis of shot peening. Jour. Materials Processing Technology, 80-81:304-308.

[6] Homer, S.E. and Van Luchene, R.D. 1991. Aircraft Wing Skin Contouring by Shot Peening. Jour. Materials shaping Technology, 9/2:90-101.

5-13

Evaluation of tool performance and hole quality when drilling C355 aluminium alloy using diamond coated and PCD drills

R. Rattanakit[1], S.L. Soo[1], D.K. Aspinwall[1], B. Haffner[2], Z. Zhang[3], D. Arnold[4], P. Harden[5]
[1] Machining Research Group, School of Mechanical Engineering, University of Birmingham, Edgbaston, Birmingham, B15 2TT, UK
[2] Doncasters Sterling, Colliery Lane, Exhall, Coventry, CV7 9NW, UK
[3] Doncasters Group Ltd., Millenium Court, First Avenue, Burton-upon-Trent, Centrum 100, DE14 2WH, UK
[4] MAPAL Ltd., Old Leicester Road, Swift Park, Rugby, CV21 1DZ, UK
[5] Element Six Ltd., Shannon Airport, Shannon, Co. Clare, Ireland

Abstract. The paper details experimental work to investigate the influence of tool material/coating (uncoated carbide, chemical vapour deposited (CVD) diamond coated carbide and polycrystalline diamond (PCD)) and cutting speed (130 and 260m/min) on drill wear, cutting forces/torque and hole quality/integrity, when drilling 4.8mm diameter blind holes in cast, heat treated C355 aluminium alloy (~ 4.7% Si content). Tool flank wear after ~1680 holes was up to ~6 times higher with uncoated carbide (WC) drills compared to PCD, while thrust forces correspondingly showed a two-fold increase with the former at a cutting speed of 260m/min. Hole surface roughness produced using PCD drills did not exceed ~0.3µm Ra for all conditions tested, while it varied between 0.6 – 1.8µm Ra along the length of the hole when employing uncoated and coated WC tools, due to scoring and smearing of the workpiece. Hole roundness was below 7µm in all trials assessed. Hole cross sectional micrographs showed no significant damage or deformation of the material microstructure, with the exception of some minor pitting on surfaces produced using the uncoated WC drills.

Keywords: Drilling, CVD diamond, PCD, aluminium alloy

1. Introduction

Aluminium alloys are widely used in industry not least because of their exceptional strength-to-weight ratio, the tensile strength and density of a typical heat-treatable cast material (LM16 equivalent) being 240MPa and 2.71g/cm^3 respectively [1, 2]. Silicon is added to Al alloys to further improve casting ability and strength while minimising shrinkage during solidification and thermal expansion [2]. The presence of Si however can significantly reduce tool life during machining due to its abrasive properties [3], whilst the softer Al phase has a tendency to adhere to the surface of tools and form a built-up edge (BUE) especially at low cutting speeds, leading to poor component quality [4].

High-speed steel (HSS) and uncoated tungsten carbide (WC) tools have traditionally been utilised with cutting fluid for the machining of Al alloys [5], while low-friction coatings such as diamond-like carbon (DLC) and molybdenum disulphide (MoS2) based products, have been successfully used to minimise BUE and workpiece material adhesion when drilling Al-Si alloys under dry conditions or using minimum quantity lubrication (MQL) [6, 7]. Since their introduction in the early 1970's, polycrystalline diamond (PCD) products and more recently thin/thick film chemical vapour deposited diamond (CVD diamond) tools, have seen increased application in the automotive and aerospace industries. The significant advantages of PCD compared to standard WC cutters when machining non-ferrous materials have been well documented [8], and include significantly higher tool life, superior workpiece surface finish, reduced tool changing and increased productivity. Although less commonly employed, thick film CVD diamond (500µm thick) tooling has been shown to match or exceed the performance of PCD and WC when turning abrasive materials such as 20% SiC reinforced Al metal matrix composites and hypereutectic Al-Si alloys [9, 10]. Edge preparation costs aside, thick film CVD diamond generally results in longer tool life compared to the thin-film variant (≤ 30µm thick), despite the former being prone to chipping from the deposition process induced residual stresses which can weaken the cutting edge [11].

The drilling of blind holes is a key operation in high volume production of aluminium compressor impellers for automotive turbocharger assemblies, prior to finish reaming. The following work was undertaken to investigate the influence of tool material/coating and cutting speed on drill wear, cutting forces/torque and hole quality/integrity when drilling 4.8mm diameter blind holes in cast C355 aluminium alloy.

2. Experimental work

The C355 aluminium alloy blocks containing ~4.7% Si were produced by die casting and heat treated to give a bulk hardness of 140HV. Individual test pieces measuring 340x180x30 mm were used for mainstream tool wear/life trials while smaller samples of 20x30x180 mm were prepared for force measurement, hole roundness, cylindricity, surface roughness, microhardness and microstructure assessment. Uncoated fine grain WC (K30F with 10% Co binder) tools were benchmarked against multi-layer CVD diamond coated products (~8µm thick applied on an indentical WC substrate) and two different brazed PCD grades, which involved a unimodal (CTB010; 10µm average grain size) as well as a mixed/multimodal (CTM302; 2-30µm grain size) formulation. The uncoated and CVD diamond coated twist drills were 3 flute with helix and point angles of 15° and 150° respectively whilst the PCD tools had 2 straight flutes (0° helix) and a corresponding 130° point angle.

Blind hole (4.8mm diameter) drilling tests to a depth of 28mm were performed on a Matsuura FX-5 high speed machining centre involving 2 variable factors of tool material (4 levels) and cutting speed (2 levels), see Table 1. Feed rate was kept constant at 0.1mm/rev while tool overhang was typically ~36mm with corresponding runout of <0.01mm. All tests were performed in a flood environment (3bar, 25l/min) using a water based emulsion containing mineral oil at a concentration of 7-10%. Tool life criterion was either 1680 holes (840 holes per block) or a maximum flank wear (VB_{Bmax}) of 0.3mm.

Response measures were recorded following the first hole and at intervals of 280 holes thereafter. Tool wear was measured with an optical microscope while thrust forces and torque were recorded using a four-component drilling dynamometer fitted with a bespoke workpiece fixture and connected to charge amplifiers. Mean hole diameter was evaluated at the top, middle and bottom locations with a digital indicator attached to a Diatest split ball probe (0.001mm resolution). Hole roundness and cylindricity measurements were performed on a Talyrond 300 unit, each with a total of 15 profiles.

Table 1. Test matrix and variable factors

Test No.	Tool material/coating	Cutting speed, m/min (rpm)
1	Uncoated WC	130 (8,500)
2	Uncoated WC	260 (17,000)
3	CVD diamond coating	130 (8,500)
4	CVD diamond coating	260 (17,000)
5	PCD CTB010	130 (8,500)
6	PCD CTB010	260 (17,000)
7	PCD CTM302	130 (8,500)
8	PCD CTM302	260 (17,000)

Drilled hole surface roughness (Ra) was assessed with a Form Talysurf 120L having a 2µm radius diamond stylus using a 0.8mm cut-off and 4.0mm evaluation length. Measurements were taken at ~2mm and 25mm from the hole entry and averaged. Cross-sectioned specimens (using wire EDM down the hole centreline) were cold mounted in an epoxy resin mixture followed by grinding and polishing prior to the measurement of microhardness depth profiles, which was carried out on a Mitutoyo HM 124 tester. These were performed on the last hole of each test with a Knoop diamond indenter (25g load) at a depth of ~12mm from hole entry. The polished samples were subsequently etched in Keller's reagent to enable optical investigation of microstructure and surface/subsurface damage. No trial replications were performed due to limited tool availability and cost constraints.

3. Results and discussion

Figure 1 shows optical micrographs of drill edges in the new and worn condition for each trial. Significant adhesion of workpiece material and BUE was evident on the flank and chisel edges of uncoated drills irrespective of cutting speed. In contrast, this was not observed when employing CVD diamond coated tools, although peeling of the coating layer occurred after hole 282 when operating at the higher cutting speed, which led to premature termination of the test. Similarly, no signs of material adhesion or BUE was visible on any of the PCD blanks, but there was accumulated material on the carbide body/chisel edge of the tools.

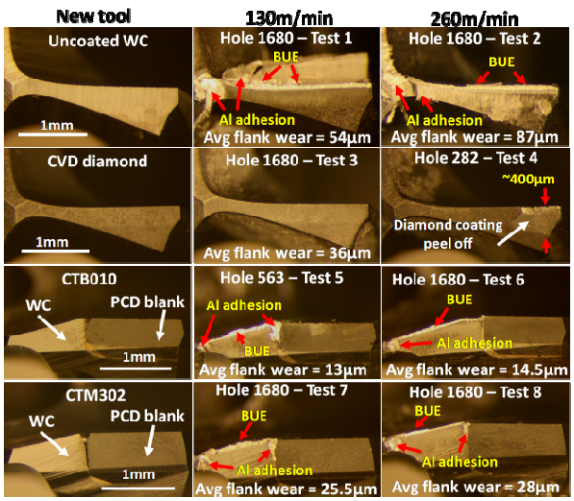

Fig. 1. Micrographs of drills in new and worn condition

The drill in Test 5 suffered catastrophic breakage due to a malfunction in the tool changer during the experiment and hence the test had to halted after 563 holes. The flank wear progression of each tool over the test duration is detailed in Fig. 2. In general, the PCD drills showed the lowest wear rate, with the CTB010 grade (Test 6)

having a VB_{Bmax} of only 14.5µm after 1680 holes. Conversely, wear on the uncoated WC drills at low (Test 1) and high (Test 2) cutting speeds was 55µm and 87µm respectively at test cessation (~4 and ~6 times higher respectively).

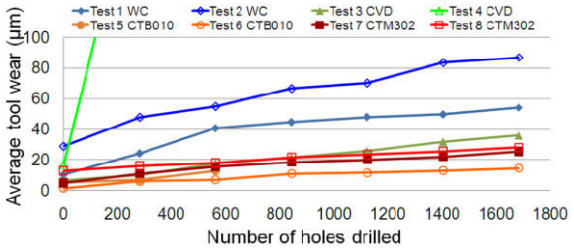

Fig. 2. Drill flank wear curves

Similar results were recorded for thrust force data, where a significant reduction was observed when employing PCD drills. Despite a straight fluted geometry, the PCD products (Test 5 to Test 8) generated ~70 to ~125% lower average thrust forces compared with uncoated and CVD diamond coated twist drills (Test 1 to Test 4) under equivalent machining conditions, see Fig. 3. Additionally, forces in the former remained stable throughout the trials. Although not shown here, torque values generally showed an increasing trend with the number of holes drilled, due to tool wear progression. A number of tests also exhibited high initial torque levels (Tests 2, 3, 4 & 8), which was possibly due to Al material adhering on drill corners at trial commencement.

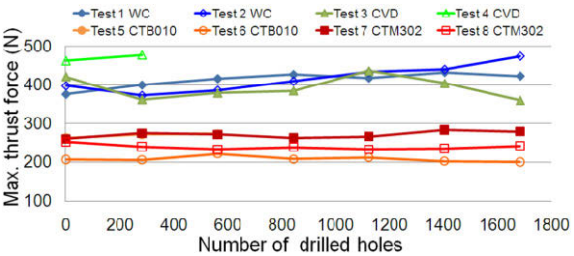

Fig. 3. Maximum thrust forces

Hole diameter in general decreased as cutting progressed due to tool wear, see Fig. 4. All holes produced with the CVD diamond coated drills were oversized, which was a result of the coating thickness. Although initially oversized by 4-10µm, the diameter of holes machined with uncoated WC tools steadily decreased by ~15µm at the end of the trial. Despite being undersized, holes drilled with PCD tools showed minimal diametral variation over the entire experiment.

Hole roundness and cylindricity results are presented in Fig. 5. The average out of roundness did not exceed 7µm and was comparable for each of the different tool materials evaluated. In terms of cylindricity, the mean deviation was marginally higher when using PCD drills, although this did not exceed 22µm. This was most likely due to the difficulty in chip/swarf evacuation as a result of the straight fluted tool geometry. In addition, cylindricity tended to improve when operating at lower cutting speed.

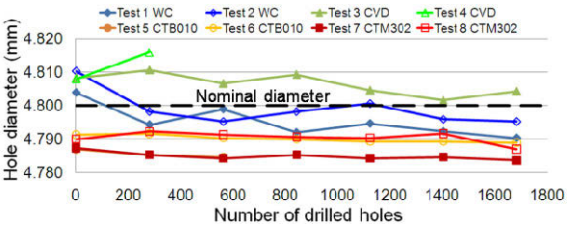

Fig. 4. Hole diameter

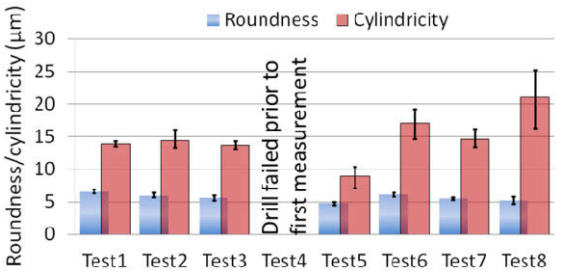

Fig. 5. Hole roundness and cylindricity

Surface roughness near the hole entry was generally lower compared to the bottom location, see Fig. 6 and 7 respectively, most probably due to the increased difficulty of swarf evacuation and possible tool vibration as drilling depth increased [12]. In general, carbide drills produced holes with the poorest surface finish particularly towards the exit position, which reflects the greater tool wear rate and high levels of BUE as evident from previous tool micrographs. The PCD drills generated the lowest surface roughness irrespective of cutting speed, which was below 0.3µm Ra even after 1680 holes and consistent over the entire hole length.

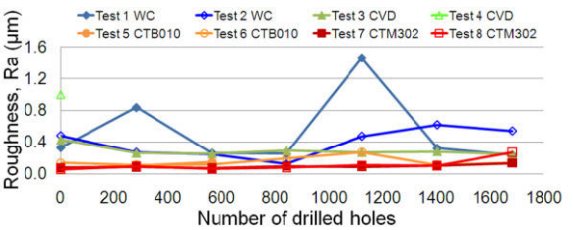

Fig. 6. Hole surface roughness near entry location

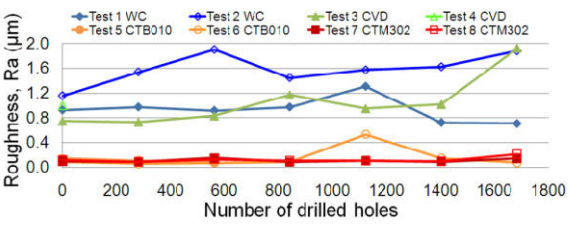

Fig. 7. Hole surface roughness near exit location

Other factors which compromised Ra was the formation of 'scuff' marks similar to that illustrated in Fig. 8(a), which were caused by ploughing/re-deposited material, and the occasional presence of workpiece defects (inclusions, voids, etc.) as shown in Fig. 8(b). This was probably the reason for the unusual peaks/spikes in the surface roughness profiles observed in Tests 1 and 6.

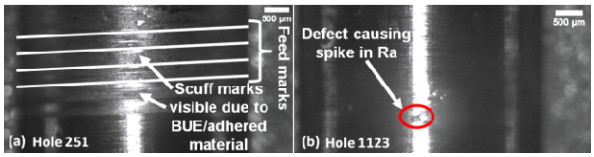

Fig. 8. Hole cross section from; (a) Test 1-entry, (b) Test 6-exit

Figure 9 shows workpiece microhardness results from trials after 1680 holes (Tests 1-3, 6-8). A hardened region up to a maximum of 169HV (~21% above bulk hardness) and extending to a depth of ~100µm from the machined surface was observed in the majority of specimens analysed. No major variation in hardness was detected with changes in drill speed. Investigation of corresponding cross-sectional micrographs detailing drilled hole surface/subsurfaces, see Fig. 10, showed no obvious evidence of microcracks, surface damage or microstructural alterations, irrespective of tool condition. Minor pitting however was seen in the last and first holes from Tests 1 and 2 (uncoated WC tools) respectively.

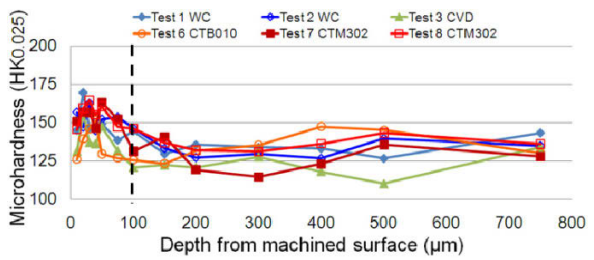

Fig. 9. Microhardness depth profiles at hole 1680

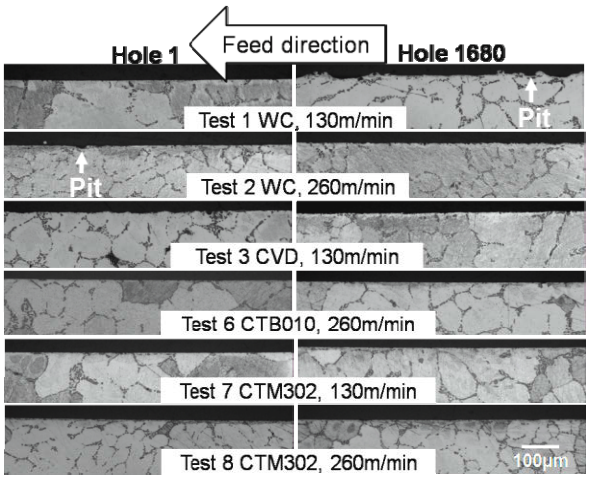

Fig. 10. Cross-sectional micrographs of hole microstructure

4. Conclusions

Substantial amounts of workpiece adhesion and BUE were present on the uncoated WC drills, which led to comparatively high thrust forces (up to ~500N). In contrast, evidence of adhered material on the CVD diamond and PCD tool surfaces was minimal. While the CVD diamond coating generally increased drill life compared to uncoated tools, the relatively poor bonding between the coating and substrate led to peeling/delamination at the higher cutting speed level. A hardened region measuring up to ~29HV above the workpiece bulk hardness to a depth of ~100µm was typically recorded in tests which achieved 1680 holes. Sample hole cross-sectional assessment of microstructure revealed no microcracks or microstructural alterations. While small surface pits were observed in trials using the uncoated WC tools, such flaws would easily be removed by any subsequent finishing/reaming operation.

References

[1] Bauccio M, (1993) ASM Metals Reference Book. ASM International
[2] Polmear I, (2006) Light alloys: From traditional alloys to nanocrystals. Butterworth Heinemann
[3] Roy P, Sarangi SK, Ghosh A, Chattopadhyay AK, (2009) Machinability study of pure aluminium and Al-12% Si alloys against uncoated and coated carbide inserts. Int J Refract Met Hard Mater27(3):535-544
[4] Yousefi R, Ichida Y, (2000) A study on ultra-high-speed cutting of aluminium alloy: Formation of welded metal on the secondary cutting edge of the tool and its effects on the quality of finished surface. Precis Eng 24(4): 371-376
[5] Smith GT, (2008) Cutting tool technology. Springer
[6] Bhowmick S, Alpas AT, (2008) Minimum quantity lubrication drilling of aluminium-silicon alloys in water using diamond-like carbon coated drills. Int J Mach Tools Manuf 48(12-13):1429-1443
[7] Wain N, Thomas NR, Hickman S, Wallbank J, Teer DG, (2005) Performance of low-friction coatings in the dry drilling of automotive Al-Si alloys. Surf Coat Technol 200(5-6):1885-1892
[8] Jennings M, Clark I, (1995) PCD in the automotive industry. Ind Diamond Rev 55(2):51-53
[9] Sussmann RS, Brandon JR, Collins JL, Whitehead AJ, (2001) A review of the industrial applications of CVD diamond. Ind Diamond Rev 61(4):271-280.
[10] Uhlmann E, Friemel J, Brucher M, (2001) Machining of hypereutectic aluminium-silicon alloy. Ind Diamond Rev 61(4):260-265
[11] Kanda K, Takehana S, Yoshida S, Watanabe R, Takano S, Ando H, Shimakura F, (1995) Application of diamond-coated cutting tools. Surf Coat Technol 73(1-2):115-120
[12] El-Khabeery MM, Saleh SM, Ramadan MR, (1991) Some observations of surface integrity of deep drilling holes. Wear 142(2):331-349.

5-14

Real-time monitoring, control and optimization of CO_2 laser cutting of mild steel plates

E. Fallahi Sichani, J. De Keuster, J.-P. Kruth and J. R. Duflou
Dept. of Mechanical Engineering, Katholieke Universitieit Leuven, Celestijnenlaan 300 B, B-3001 Heverlee (Leuven), Belgium

Abstract. This paper presents a real-time monitoring and control system for oxygen-assisted CO_2 laser cutting of thick plates of mild steel. The proposed system consists of two subsystems, namely a process monitoring and a control and optimization module. The process monitoring module evaluates the cut quality based on a set of sensing parameters, derived from analysis of data provided from two optical sensors (photodiodes and a NIRcamera). These sensing parameters are chosen to be well correlated with different quality characteristics of the cut surface. An overview of the most suitable set of sensing parameters and how they correlate with different quality deteriorations are mentioned as well as the reasons for these correlations. The real-time control and optimization module is implemented as an expert system. It compares the sensing parameters with predefined thresholds and diagnoses the quality defect. Furthermore the system modifies the cutting parameters based on the predefined set of rules corresponding to the identified quality defect. The obtained results prove the effectiveness of the system in terms of increased autonomy, productivity, and efficiency of the process, as well as elimination of the need for manual quality control and the possibility to automatically generate quality reports.

Keywords: laser cutting, monitoring, adaptive control, optimization

1. Introduction

In the case of cutting thick plates, the very narrow process window of CO_2 laser cutting necessitates using a real-time monitoring and adaptive control system which is not commercially available so far. As state of the art prior to the reported contribution, the following efforts can be referred to.

Jorgensen [1] used a Si photodiode and a CCD camera to monitor the laser cutting process. The mean value and the variance of the photodiode signal proved to correlate well with dross formation and the roughness of the cut surface, respectively. As for the CCD camera, the mean pixel value of the recorded images proved to correlate well with dross formation, whereas the variance could be correlated to the roughness of the cut surface. Furthermore, based on the images, the cut kerf width could also be measured. Authors [2] have reported on successful performance of a photodiode-based monitoring and control system being capable of detecting and correcting typical quality deteriorations in cutting thick plates of mild steel. Chatwin et al. [3-5] developed a knowledge-based adaptive control system for laser cutting, based on a photodiode and a CCD-camera that monitors the spark cone ejecting from the bottom of the plate. A photodiode was used to measure the temperature/irradiance, emitted by the cut front. Reportedly a bad cut quality was typically characterized by a larger, more diffuse spark cone. Decker et al. [6] developed a collinear photodiode set-up using a partially transmitting mirror. The presented results are in agreement to those of Jorgensen. Kaplan et al. [7] measured the thermal radiations emitted from the cutting front using a selective ZnSe mirror and Si photodiode. The roughness proved to be proportional to the detected striation period. The occurrence of burning defects could be detected by a quality factor combining the mean and variance of the photodiode signal.

Poprawe et al. [8, 9] developed a universal coaxial process control system, a modular system that can be equipped with different sensors, like CCD-cameras and photodiodes, for monitoring different laser manufacturing processes. The major advantage of the photodiode-based monitoring system is high monitoring frequencies thanks to the very short response time and relatively fast signal processing techniques. The main advantage of camera-based monitoring systems is the capability of providing spatial information which offers more insight into the process.

2. Experimental setup

The setup used for the experiments reported in this paper was a 2D laser cutting machine with flying optics architecture, a 6 kW CO_2 laser source ($M^2 = 4.24$) and a Fanuc controller. A monitoring direction coaxial with the laser beam was chosen. As shown in Fig. 1, the optical setup consists of:

- a dichroic mirror transmitting the laser beam and reflecting the NIR process emission towards the camera setup
- a diaphragm and a focusing lens to focus the process radiation
- a beam-splitter folding mirror to assure optimal process light transmittal to reflect a part of the process radiation towards the camera and to transmit the remainder towards a photodiode sensor (not shown on Fig. 1).

Taking the melt temperature of mild steel and the laws of Planck and Wien into account, it can be calculated that the peak wavelength of the process emission spectrum is around 1.7 µm. Therefore a NIR camera with an InGaAs detector was chosen.

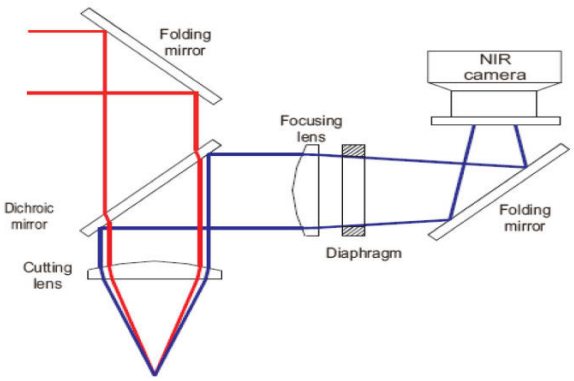

Fig. 1. Optical setup for the NIR camera monitoring system

3. Quality criteria and sensing parameters

In compliance with relevant standards [10-12], the following cut quality characteristics were selected for monitoring purposes:

- dross attachment: quantified by the height of the dross (resolidified material) roughness: quantified by R_z , measured by a non-contact profilometer at a height as specified in [10, 11]
- drag of the striations: quantified as the distance between the start and the end point of the striation, orthogonally projected to the plate surface (measured by optical microscope)
- burning defects: quantified as the average number of burning defects per unit length
- squareness of the cut edge: quantified as per [10], measured by a tactile probe
- kerf width

Figure 2 shows NIR images recorded during the laser flame cutting of ST52-3 15 mm at cutting speeds 100-120% of the standard value. Offline analysis of the cut surface revealed that the drag of the striations and the dross attachment are directly proportional to the cutting speed. In NIR images, this is clearly visible as a significant enlargement of the central hot zone, particularly along the cutting direction. This can be attributed to the elongation and slightly higher location of the process front which is the result of depleted energy input per unit length.

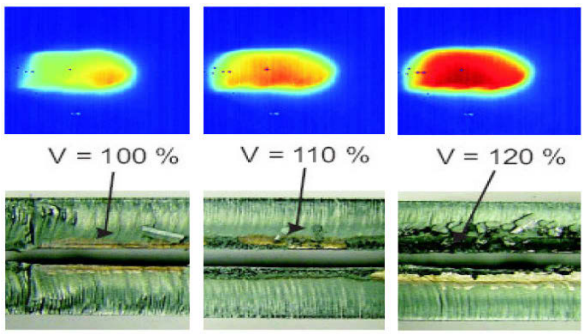

Fig. 2. NIR images vs. cut quality for laser flame cutting 15 mm thick ST52-3 with increasing speed

At low cutting speeds (e.g. 60-100% of the standard speed), the drag of the striations decreases and no dross attachment was observed. However the roughness, number of burning defects and cut kerf width all increase. In the NIR images captured while cutting at moderately low speed, the process zone appears less elongated and with a low intensity (as illustrated in the image corresponding to V=80% in Fig. 3). This is the result of the surplus energy per unit length, leading to a straighter and steeper process front and thus easier melt removal. When the cutting speed is further reduced, the width of the tail of the process front increases and varies significantly (as illustrated in the image corresponding to V=60% in Fig. 3). Such an image is suggestive of localized increases of kerf width (burning defect) because of a too high energy input per unit length.

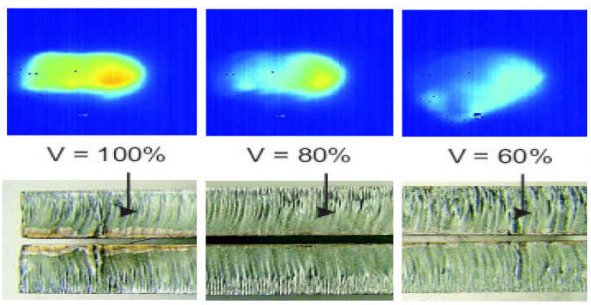

Fig. 3. NIR images vs. cut quality for laser flame cutting 15 mm thick ST52-3 with decreasing speed

The kerf width was determined based on the calculation of the intensity gradient of the NIR images (Fig. 4). This

method is computationally expensive and is therefore not implementable in a high-frequency monitoring algorithm.

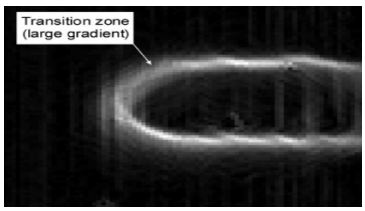

Fig. 4. Kerf width indicated by the transition zone between solid and molten material

No sensing parameter could be identified that correlates to the squareness of the cut edge because of the view point of the camera. Table 1 offers an overview of sensing parameters correlated with different cut quality aspects in terms of Arbituary Digital Units (ADU).

4. Adaptive control and optimization

The adaptive control was implemented as a rule-based expert system. During the real-time monitoring, the values of different sensing parameters are compared with well-chosen threshold values and a predefined quality class is assigned to the current cut quality.

- Quality class 0: acceptable cut quality;
- Quality class 1: too high drag of the striations, indicating a high risk of dross formation;
- Quality class 2: presence of burning defects, therefor increasing the roughness of the cut edge;
- Quality class 3: combination of Quality class 1 and 2 ,typical for preheated workpieces;
- Quality class 4: loss of cut.

The rule-based expert system associates each quality class with a quantitative corrective strategy. based on which cutting parameters are overwritten in real time to salvage that specific quality deterioration. For a detailed explanation on the corrective strategy corresponding to each quality class see [13].

The performance of the adaptive control and optimization algorithms was evaluated on different material/thickness combinations. Fig. 5 shows the real-time alteration of the process parameters during a linear cut in HARDOX-400 25mm starting from standard process settings. While the cut quality remained acceptable, the optimization resulted in approximately 21% increase of cutting speed (i.e. 168 mm/min) due to an increase of the duty cycle and the gas pressure.

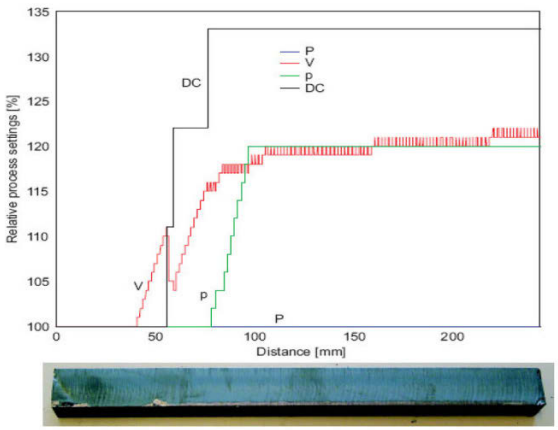

Fig. 5. Control and optimisation of linear cutting of HARDOX-400 25 mm starting from standard process settings

Figure 6 illustrates the real-time alteration of the process parameters during a linear cut in ST52-3 15 mm, starting with a cutting velocity 20% higher than the standard value. It can be noted that at the outset of the cut, the shortage of energy input per unit length was sensed by the control and optimization system and therefore the velocity and the duty cycle were drastically changed in order to correct the cut quality.

A typical problem in laser cutting of complex contours is the heat accumulation at sharp corners. This preheating effect drastically increases the oxidation rate. The performance of the control and optimisation system was verified during cutting of complex contours including all possible geometrical features: linear segments, smoothly curved segments, corner segments including both obtuse and sharp angles (Fig. 8).

In this test the outer contour was cut before the inner one. This unusual cutting sequence was opted to create the worst case scenario with respect to heat accumulation by prohibiting the heat removal from the central zone of the workpiece. Fig. 7 shows the real-time evolution of the

Table 1. Overview of identified sensing parameters

Quality criterion	Sensing parameter(s)
Dross attachment	Length of the hot process zone (ADU > 3000), Area of the hot process zone (ADU > 3000)
Roughness	Variation of the width of the global process zone (ADU > 1000)
Drag of striations	Length of the hot process zone (ADU > 3000), Area of the hot process zone (ADU > 3000)
Burning defects	Variation of the width of the global process zone (ADU > 1000)
Kerf width	Calculation based on the intensity gradient of the NIR image

process parameters during cutting of the above-mentioned part. Fig. 8 compares the resultant cut quality with and without the real-time control and optimization system.

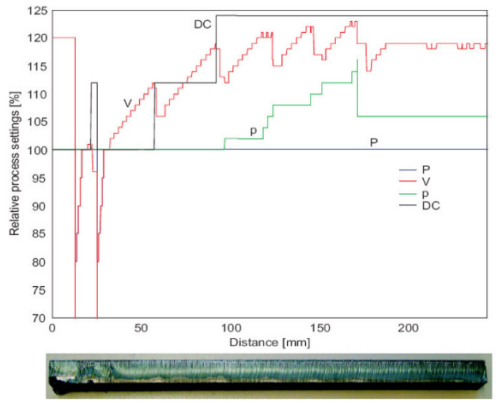

Fig. 6. Control and optimisation of linear cutting of ST52-3 15 mm, starting from V=120 % of $V_{standard}$

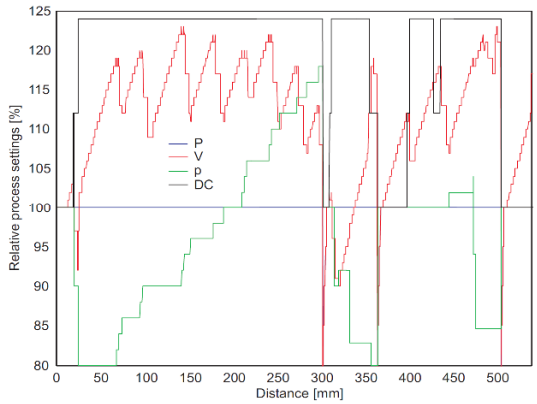

Fig. 7. The performance of the control and optimisation system for a complex workpiece

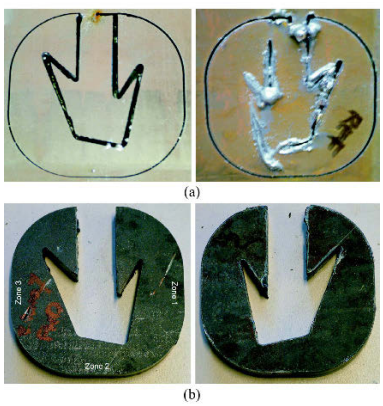

Fig. 8. Top and bottom view of the complex workpiece, (a) without the control and optimization system; (b) with the control and optimization system

5. Conclusion

The developed NIR-camera-based monitoring system is capable of sensing the main quality parameters in CO_2 flame laser cutting. Dross attachment, roughness, drag of striations and the occurrence of burning defects can be monitored in real time; whilst the kerf width can be calculated at a sufficiently high sample frequency. The developed real-time monitoring system was linked with a rule-based adaptive control system for automatic process quality assurance. The functional performance of this control system was illustrated by means of a series of tests on different material/thickness/geometry combinations.

References

[1] Jorgensen H. , PhD thesis, Technical University of Denmark, Lyngby, Denmark, 1990
[2] De Keuster J., Duflou J. R., Kruth J.-P., in Proceedings of the LANE 2007, Vol. 2, 979-992, 1999
[3] Huang M.Y. and Chatwin C.R., Optics and Lasers in Engineering 21, 273-295, 1994
[4] Huang M.Y. and Chatwin C.R., Lasers in Engineering 3, 125-140, 1994
[5] Lim S.Y. and Chatwin C.R., Lasers in Engineering 3, 99-112, 1994
[6] Decker I., Heyn H., Martinen D., and Wohlfahrt H., in Proceedings of the SPIE, volume 3097, 29-37, 1997
[7] Kaplan A.F.H., Wangler O., and Schuöcker D., Lasers in Engineering 6, 103-126, 1997
[8] Poprawe R. and Konig W., in Annals of the CIRP 50, 137-140, 2001
[9] Abels P., Kaierle S., Kratschz C., Poprawe R., and Schulz W., in Proceedings of the ICALEO 1999, Vol. 87, E99-108, 1999
[10] ISO 9013: Thermal cutting - Classification of thermal cuts – Geometrical product specification and quality tolerances
[11] VDI 2906: Blatt 8, Quality of cut faces of (sheet) metal parts after cutting, blanking, trimming or piercing - Laser cutting
[12] DIN 2310: Thermal cutting - Part 30: Classification of thermal cuts, principles of process, quality and dimensional tolerances
[13] Fallahi Sichani E., De Keuster J., Kruth J.-P., Duflou J. R. Physics Procedia, Volume 5, Part 2, 2010, Pages 483-492.

5-15

The stress-strained state of ceramic tools with coating

Grigoriev[1] S., Kuzin[1] V., Burton[2] D., Batako[2] A. D.
[1] Moscow State Technological University «Stankin», Vadkovsky per. 3a, Russia.
[2] Liverpool John Moores University, Byrom Street, Liverpool , L3 3AF, UK.

Abstract. This paper presents some fundamental investigations into the physical laws that govern the wear of coated ceramic tools. A mathematical model of a stress-strained state of ceramic tools with coating has been developed to analyze this process in details. This mathematical model is built on the finite elements method that is based on multi-dimensional theories of heat transfer and elasticity. In this work, the developed model uses the solutions of two-dimensional heat conductivity and elasticity to predict the wear of coated ceramic tools in stress-strained state. Results of the simulated stress-strained state of ceramic tools with coating are presented. A new generation of coating for ceramic tools have been developed using of these results.

Keywords: Ceramic Tools, Coating, Stress-Strained State, Mathematical Model.

1. Introduction

The ceramics is a very promising tool material. Ceramic tools considerably intensify production processes and improve product precision and quality [1]. However, such tools are of limited applicability on account of their poor reliability.

Effective method of improving of ceramic tools is the application of functional coatings. The composite nature of such an arrangement, allows to combine exploiting efficiently the properties of the internal bulk ceramic material and the coating. Functionality of these coatings consists of the following; the coating eradicates technological defects at the surface layer of the tools. The dense structure of a coating increases the resistance of the ceramic tool to the formation of cracks. Layers of coating become a barrier for the growth of cracks generated from the inside bulk of ceramic material.

However, operating experience of ceramic tools shows that coatings from various refractory materials do not always affect the operational characteristics. This is because coated tools become a complex system «ceramics – coating» in which each component has its own physical mechanical and thermal properties. An unfavourable combination of these elements can lead to the formation of localized high stresses at the upper layer of ceramics and to the generation of cracks. Therefore, the identification of the relationship of the coating properties with a stress-strained state of the surface layer of ceramic tools is an actual scientific task. This article is devoted to the solution of this task.

2. The Mathematical model

The stress-strained state of various structures may be effectively studied by the finite element method, which is well adapted to machine calculations. It produces a complete picture of the stress-strained state of complex structures, with high precision, and the results are presented in useful form, including graphical display. This method is used in the present work.

A mathematical model was developed to study the stress-strained state of coated ceramic tools. At model creation it was assumed that the flat problem is considered; no plastic deformation occurs at the cutting edge of the tool; the structure of ceramics and coating is the faultless so there are neither pores nor cracks.

Initially, a micro-structure model of a coated ceramic plate was developed [2]. The algorithm of realization of this approach is given in Fig. 1 (a). The cutting plate is presented as a repeating elementary fragment of coated ceramic plate consisting of structural elements of ceramics (grain, inter-grain phase and matrix); the coating and the workpiece material. This allows using the heterogeneous properties of the ceramic and the workpiece materials in the model. Then on the basis of the allocated elementary fragment of coated ceramic plate the calculation scheme was generated. It is presented in the form of a design [Fig. 1 (b)]. This design consists of a single grain having ellipse form with semi-major axis (a) and semi-minor axis (b). This grain is closed up in a matrix through inter-grain phase of a thickness δ_f.

The free surface of the grain, inter-grain phase and matrix is covered by N layers of coating with a thickness d_j, where $j = 1, 2..., N$. The elements of this design is characterised by the following properties: density ρ, modulus of elasticity $E(T)$, thermal conductivity $\lambda(T)$,

heat capacity $c_p(T)$, linear expansion α and Poisson ratio μ.

The following scheme of loading of coated ceramic plate is developed. Figure 1 (b) shows the schematic complex loading approach implemented in this model. The external contour of layer N is subjected to the action of time-dependent point forces F_i inclined at angles β_i, to the y axis; distributed forces P_1 and P_2; and heat fluxes Q_1 and Q_2. In the calculations, we take account of the convective heat losses with heat-transfer coefficients h at the sections of the contour with no heat flux.

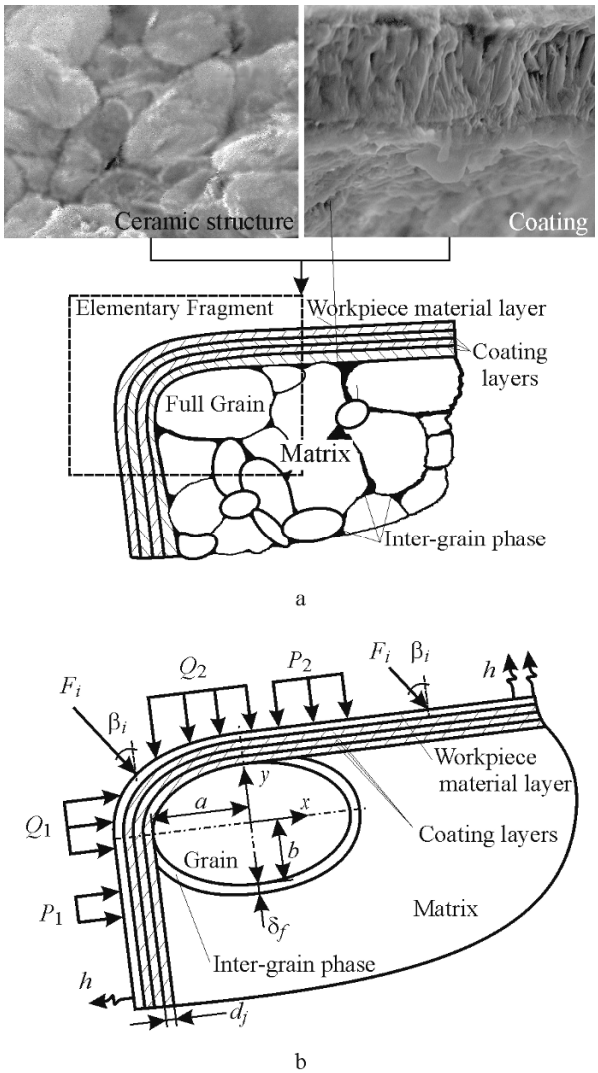

Fig. 1. Micro-structure model of a coated ceramic plate

The mathematical model of the stress-strained state of coated ceramic plate is based on the solutions of two dimensional problems of thermal conductivity and elasticity. Finite element method is used to implement algorithms to solve stationary and non-stationary problems of thermo-elasticity. The algorithms are realized as an automated system of computing the thermo-strength calculations of ceramic plates [3].

The calculation scheme shown in Fig. 2 was used for identification of the relationship of the coating properties with a stress-strained state of the surface layer of ceramic plate. Silicon nitride (Si_3N_4) plate coated with different refractory material was used in this study. The workpiece material was chromium steel (X32CrMoV12-28). The following loads were used: $F_1 = F_2 = 0.01$ N; $\beta_1 = \beta_2 = 45^o$; $P_1 = P_2 = 1 \cdot 10^8$ Pa; $Q_1 = Q_2 = 1.4 \cdot 10^8$ W/m^2 and $h = 1 \cdot 10^5$ W/m$^2 \cdot$K.

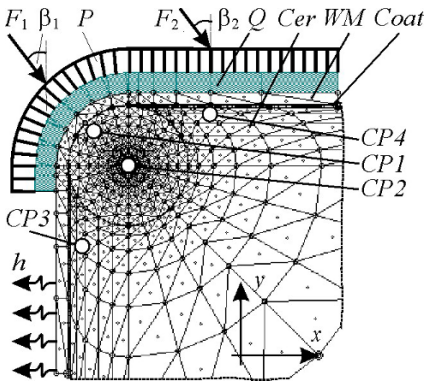

Fig. 2. Calculation scheme for modelling (a = b = 50 μm)

The control points *CP 1 – CP4* were used for an analysis of calculations. These control points mean fixed four finite elements of reseaching design. In Fig. 2 the following abbreviations are used: *"Cer"* is the ceramics, *WM* is the workpiece material and "*Coat*" is the coating.

3. Results and discussion

The results of calculation of temperatures taken at the control points are given in Table 1, where the first row shows the temperatures of the ceramic plate without coating. It is observed from this table that coatings have a drastic effect on the thermal state of the ceramic plate. The temperature in the plate with the coatings of various refractory materials varies in the range of 25%. Plates with TiB_2 coating have the lowest temperature whereas *BN* coating give the highest values. TiB_2, *TiN*, *WC*, *BeO*, Mo_2C and *TiC* coating provide the reduction in temperature comparing plates without coating. However, the other types of coating including Al_2O_3 increase the temperatures. With plates made of Si_3N_4, the *TiN* coating gave 8% reduction in temperatures whereas *TiC* achieved only 1%.

Different refractory materials of coating practically do not influence the character of a temperature field of Si_3N_4 plates. The minimum changes of parities between temperatures in different control points for different ceramic plates testify this.

From the obtained results, the relationship of the thermal conductivity of the coating and the thermal state of the plate was derived. The temperature (*T)* at the control points *(CP1-CP4)* can be expressed as follows:

$$T^1 = 1489.9\ \lambda_{coat}^{-0,0474};\ T^2 = 986,8\ \lambda_{coat}^{-0,0429},$$

$$T^3 = 443,78\ \lambda_{coat}^{-0,034};\ T^4 = 968,4\ \lambda_{coat}^{-0,0428}$$

Table 1. Temperatures at control points on the plate

Coating	Temperatures, T,° C			
	CP1	*CP2*	*CP3*	*CP4*
No coat	1240	836	391	822
TiB_2	1103	762	378	762
TiN	1145	789	387	791
WC	1181	810	392	810
BeO	1219	809	364	780
Mo_2C	1222	829	393	821
TiC	1235	843	392	831
SiC	1309	875	393	847
TaC	1315	878	400	858
MgO	1340	898	415	882
Y_2O_3	1340	898	415	882
Al_2O_3	1347	893	400	867
AlN	1355	899	404	875
ZrO_2	1358	908	418	893
BN	1368	908	408	886

Table 2 gives the results obtained in studying the effect of coating the stresses in a silicon nitride plate. It is seen that the coatings have a direct influence on the stresses. The stress intensity at the control points is increased up to 20 times in coated plate.

Table 2. Stresses at control points on the plate

Coating	Stress intensity σ_i, MIIa			
	CP1	*CP2*	*CP3*	*CP4*
No coat	275	45	641	600
WC	237	45	477	510
TiB_2	239	28	496	600
TiN	240	17	585	590
Mo_2C	240	32	595	540
TiC	264	55	590	520
BeO	270	46	601	632
TaC	322	91	584	485
SiC	405	114	551	520
MgO	600	296	693	201
Y_2O_3	600	296	693	201
AlN	646	177	590	488
BN	1231	252	423	419
Al_2O_3	2236	459	660	580
ZrO_2	2272	1137	746	1047

The lowest intensity is obtained with *WC* coating and the highest was recorded with the ZrO_2. It was found that coating with *WC*, TiB_2, *TiN*, Mo_2C, *TiC* and *BeO* on Si_3N_4 plate reduce the stresses in the surface layer of ceramic plate whereas the other coatings simply increase the stress level.

It is observed that *TiN* and *TiC* reduced the intensity of stresses at the check point CP1 by 15 and 5% respectively compared to uncoated plate. However the study of an average stress intensity shows that *TiC* has some advantages over the *TiN* with Si_3N_4 plate. Coating with Al_2O_3 considerably increases stress intensity σ_i at all control points at the surface layer.

The variation of the coating thickness δ_{coat} does not provide a linear effect on the thermal state of the Si_3N_4 cutting tips. It was fond that, with the increase of the coating thickness, the temperature at check point *CP1*, *CP2* and *CP4* decreases but at *CP3* the temperature increases. The effect of the coating thickness on the temperature was derived as follows:

$$T^1 = -\ 11.143\ \delta_{coat} + 1324.1;\ T^2 = -\ 5.6939\ \delta_{coat} + 883.27;$$

$$T^3 = 1.602\ \delta_{coat} + 389.26\ ;\ T^4 = -\ 5.3367\ \delta_{coat} + 868.91.$$

Also we investigated influence of different properties of a coating on a stress-strained state of the surface layer of ceramic plate. The coating used in these experiments was *TiC* with the thickness δ_{coat} = 5 μm. In this study a series of experiments were conducted where one parameter was varied from minimum to maximum for different refractory materials used in this work. For example, the coefficient of thermal conductivity varied between 2.4 and 150 W/m·K when investigating its effect on temperatures and stresses in the plate. Other parameters kept constant (identified *TiC*).

Special attention was paid on influence of coefficient of thermal conductivity of coating on a stress-strained state of ceramic plate. This experiment was carried out with λ_{coat} =2.4 ÷ 50 W/m.K. From the obtained results, it was identified that increasing the thermal conductivity up to 150 W/m.K led to the decrease of temperature at all control points by 1.25~1.63 times. Here, the following dependence of the temperature on the coating thermal conductivity was derived, i.e.

$$T^1 = -\ 3.53\lambda_{coat} + 1385.6;\ T^2 = -\ 2.07\lambda_{coat} + 922.2;$$

$$T^3 = -\ 0.56\lambda_{coat} + 417.4;\ T^4 = -\ 1.89\lambda_{coat} + 905.2.$$

The influence of coating thermal conductivity on the stresses in the ceramic inserts is not conclusive. However, the increase of coating thermal conductivity from 2.4 to150 W/m.K reduces the stress intensity in the tools at the control point *CP1-CP3* but it considerably increases the intensity of stresses at *CP4* which situated at a midpoint of the action of the loads. Here using plate of Si_3N_4 with a *TiC* coating the stress intensity was expressed as function of coating thermal conductivity at respective control points:

$$\sigma_i^1 = -0.11\lambda_{coat} + 268.9;\ \sigma_i^2 = -0.13\lambda_{coat} + 60.8;$$

$$\sigma_i^3 = -0.93\lambda_{coat} + 614.9;\ \sigma_i^4 = 1.65\lambda_{coat} + 463.9.$$

The effect of thermal expansion of the coating (α_{coat}) on the stresses in the ceramic plate was investigated by varying the coefficient in the range of $\alpha_{coat} = 1 \div 15 \cdot 10^{-6}$m/mK. It was found that this effect depends on the location of the control points relative to the heat flux.

Therefore, with the increase in the coating thermal expansion α_{coat} the stress intensity in control point *CP1* and *CP2* decreases, however the stress intensity increases at *CP3* where there is heat convection into the environment and at *CP4* which is closer the heat source. The effect of thermal expansion was defined as follows at respective points:

$$\sigma_i^1 = -2.36\alpha_{coat} + 286.5;\ \sigma_i^2 = -4.07\alpha_{coat} + 89.8;$$

$$\sigma_i^3 = 19.93\alpha_{coat} + 433.9;\ \sigma_i^4 = 1.29\alpha_{coat} + 510.4.$$

The modulus of elasticity of the coatings E_{coat} had great extent effect on the performance of the ceramic plate. Using values in the range of 150 up to 900 GPa, it was established that the modulus of elasticity considerably affected the stress state of the ceramic plate for any kind of external loads. Under applied forces P and F, the increase of the modulus of elasticity E_{coat} leads to a decrease in the stress intensity at all four control points. This effect on the stress intensity has been established in the following dependency for each control point:

$$\sigma_i^1 = -0.068\ E_{coat} + 350.9;\ \sigma_i^2 = -0.017\ E_{coat} + 169.5;$$

$$\sigma_i^3 = -0.026\ E_{coat} + 139.8;\ \sigma_i^4 = -0.095\ E_{coat} + 537.6.$$

However under complex mixed loading, with the increase of the modulus of elasticity E_{coat} the intensity of stress decreases at control points *CP1*, *CP2* and *CP4*, but at the point *CP3* the stress intensity increases. The following relationship expresses this effect at respective points:

$$\sigma_i^1 = -0.085\ E_{coat} + 304.9;\ \sigma_i^2 = -0.057\ E_{coat} + 85.1;$$

$$\sigma_i^3 = 0.044\ E_{coat} + 565.4;\ \sigma_i^4 = -0.14\ E_{coat} + 589.7.$$

Poisson ratio μ_{coat} of the coating had no noticeable effect on the stress in the ceramic plate. However, under force loading only, increasing μ_{coat} from 0.1 to 0.3 an increase in the stress intensity less than 1% was recorded at the point *CP1*. Under complex mixed leads, increasing Poisson ratio leads to some minor decrease of stress intensity at *CP4*.

The effect of the specific heat capacity of the coating (c_{pcoat}) on the stress in the ceramic plate was studied. The values of c_{pcoat}, covered the range from 0.3 up to 1.4 kJ/kg.K. Therefore it is concluded that the specific heat capacity of the coating had no effect on the stresses in coated ceramic plate. Similarly, by varying the density of the coating (ρ_{coat}) from 2 to 16 kg/m^3 no effect was identified. Thus there is no dependency of the stresses in coated ceramic plate on the density of the coatings.

4. Conclusion

A systematic approach to the investigation into a stress-strained state of coated ceramic tools has been presented. The developed mathematical model allowed to study the effect of various properties of the refractory materials on the temperature and stress intensity response of a coating ceramic plate under the complex mixed loads. A new generation of coating for ceramic tools have been developed using of these results.

References

[1] Grigor'ev S.N., Kuzin V.V. Prospects for tools with ceramic cutting plates in modern metal working // Glass and Ceramics, 2011, Vol. 68, No. 7-8, pp. 253-257.

[2] Kuzin V.V. Microstructural model of ceramic cutting plate // Russian Engin. Research, 2011, Vol. 31, No. 5, pp. 479-483.

[3] Grigor'ev S.N., Myachenkov V.I., Kyzin V.V. Automated thermal-strength calculations of ceramic cutting plates // Russian Engineering Research, 2011, Vol. 31, No. 11, pp. 1060-1066.

Vibration assisted surface grinding of mild and hardened steel: Performance of a novel vibrating jig design

V. Tsiakoumis and A.D. Batako
Liverpool John Moores University, Byrom Street, L3 3AF.

Abstract. One of the most significant processes in the manufacturing sector is grinding due to its high precision and accuracy. Nowadays, the demand for higher quality products and new technologies has been increased. The importance of grinding lies in the fact that it stands in the final stages of a component's manufacturing chain and therefore, the possibility of errors must be at the lowest levels. In the current work a novel method of vibration-assisted surface grinding of mild and hardened steel using aluminium oxide grinding wheels is examined. Specifically, the design concept along with the static and dynamic characteristics of a simplified vibrating jig is presented. Its purpose was to accommodate and oscillate the workpiece during surface grinding in order to improve the performance of the process in terms of achieving lower grinding forces and thus lower grinding power consumption along with lower material surface roughness values. Two grinding wheels and three workpiece materials with different properties have been ground during conventional and vibration-assisted surface grinding methods and the results are compared. The benefits of this non-conventional, advanced grinding process are clearly shown.

Keywords: vibration, grinding, forces, surface roughness, oscillating jig.

1. Introduction

Grinding accounts for 20-25% of the total expenditure on machining processes in industrialized countries. However, finishing grinding is usually found to be more costly than other processes per unit volume of material removal [1]. Therefore, the accuracy and efficiency of this process is one of the main concerns. Many researchers attempted to develop new techniques in order to improve the performance of the process. One of them was to apply ultrasonic vibrations to the wheel in order to reduce frictional effects due to interrupted contact and consequently reduce the cutting forces during grinding of monocrystal silicon [2] and soft steel [3] workpiece materials. Ultrasonic assisted machining attracted a number of researchers who achieved remarkable results in terms of lower forces and high values of surface quality [4 and 5]. The majority of these works focus on the application of ultrasonic vibration of the tool and not the workpiece. The approach of the present study is completely different to the ultrasonics. Low frequency vibrations are induced to the workpiece material via a piezoelectric actuator.

A limited number of papers have been published following the principle of low frequency vibrations. In one of these works a piezo-table that consisted of a parallelogram frame and a piezo-electric actuator was used for vibration-assisted grinding of ceramics. The vibration frequency was 200 Hz with 10μm displacement amplitude and applied in a direction coinciding with the wheel spindle axis. The superimposed vibration produced a reduction in both, normal (*Fn*) and tangential (*Ft*) force as well as better surface quality [6]. In another study low values of surface roughness were achieved during low frequency (up to 114 Hz) vibration-assisted grinding of silicon samples where vibrations were applied to the workpiece in three directions but not simultaneously [7]. However, in both studies the vibrating mechanisms were complex and the ground materials were not steel.

The aim of the present study is to design, fabricate and test a jig that can accommodate and vibrate the workpiece during shallow surface grinding of mild and hardened steel. The direction of vibration would coincide with the work-speed (*Vw*). A simplified vibrating jig was introduced to the process which could be used to oscillate the workpiece at its resonance frequency. The reason for selecting this frequency band was that the system could oscillate at high amplitudes with low voltage input. The wheel workpiece system was in compression in order to avoid any hammering process that would lead to rapid wear of the grinding wheel. In order to achieve that, according to vibro-impact theory the following condition must be met [8]:

$$2\pi\alpha f < Vw \quad (1)$$

Where α is the displacement amplitude of vibration and f the applied vibration frequency.

2. Machine tool frequency response

Firstly, the dynamic characteristics of the machine tool were identified. The purpose was to obtain the spindle response in dynamic loading conditions and to identify its resonance frequencies. These results were obtained with a sweep-sine test where a piezoelectric actuator was used to excite the spindle unit at rising frequencies while a displacement sensor measured the deflection at any time. The target was to avoid the spindle's natural frequency while excite the vibrating jig in order to avoid any resonance phenomena.

The data were recorded using a National Instrument data acquisition system (DAQ) and all the devices were calibrated before use. Fig. 1 depicts the frequency response of the spindle unit of the grinding machine used in this work.

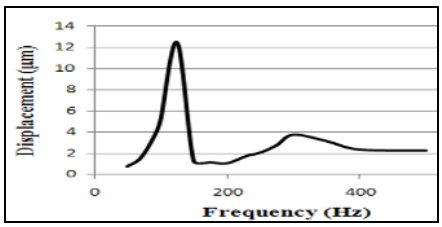

Fig. 1. Spindle unit amplitude-frequency response

The natural frequency of the spindle unit was found to be at 125 Hz with a second peak at around 300 Hz. Therefore, the vibrating jig was designed in such a manner that its natural frequency, and thus the excitation frequency, does not match the natural frequency of the spindle unit.

3. Vibrating Jig

The design concept of the vibrating jig was based on the following specifications:

- Be driven at its resonant frequency (notch of the spindle unit natural frequency).
- Not being very stiff.
- Be subjected to modifications (allow for different stiffness).
- Be simple and adaptable to any machine tool.

After a number of different designs the most appropriate one for this specific application was selected and used for the main volume of experimental work. Figure 2 illustrates the design aspects of a two flat springs vibrating jig.

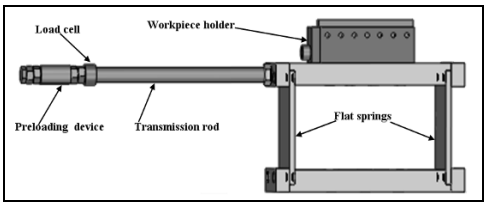

Fig. 2. Two-flat springs vibrating jig.

A piezoelectric actuator was used to vibrate the jig-workpiece and it was connected to the mechanism through a steel connecting rod. At the end of the rod a special arrangement was developed in order to preload the piezoelectric actuator as required by the manufacturer. The actuator was placed outside the working environment in order to avoid any interaction with grinding swarf and debris. In order to identify the frequency response of the vibrating jig the impact test method was employed. During the impact test the jig was impacted with an impulse at one end while at the other end an accelerometer was recording the magnitude of the acceleration and the results were illustrated in Labview software using a FFT. Its natural frequency was found to be at 275 Hz.

4. Experiment

Figure 3 depicts the actual experimental configuration along with all the necessary devices.

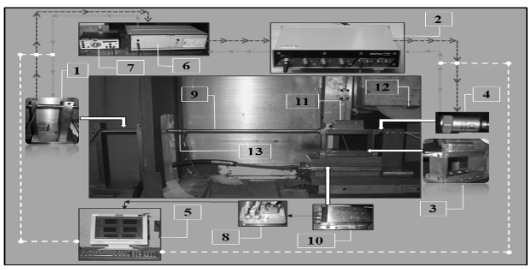

Fig. 3. Experimental Configuration [9].

A series of grinding tests were conducted using the Abwood Series 5025 conventional surface grinding machine. The function generator (7) sets the sine wave, its amplitude and frequency then sends the signal to the power amplifier (6) which drives the piezo-actuator (1). The piezo-actuator drives the oscillating rig (3) through the transmission rod (9) which has a preloading mechanism and a load cell (13). The rig is mounted on the dynamometer (10) connected to the charge amplifier (8) linked to the data acquisition system (5). The workpiece (11) sits on the rig which is driven in translation and vibratory motion under the grinding wheel (12). The closed loop control system (2) and the accelerometer (4) were used to control the amplitude of oscillation as opposed to open loop which is mainly used

by most researchers. However the work using closed loop control will be presented in future publication when investigating the effect of frequency on the process [9].

4.1. Experimental Parameters

Two wheels and three workpiece materials were put into test during conventional and vibration-assisted surface grinding. Specific normal and tangential forces, as well as surface roughness, were measured at the end of each trial. The first wheel was an medium grain - medium grade semifriable with coarse to open structure Al_2O_3 (454A 601 L 7G V 3), and the second one was an Al_2O_3 Altos long grain friable wheel with 54% porosity and high aspect ratio. The workpiece materials were Mild steel (BS970 080440, HRB 90.1), hardened En31 steel (BS534 A99, HRC 64.5), and M2 toolsteel (BS BM2, HRC 62). All the grinding experiments were conducted in dry environment in order to understand the effect of superimposed vibration on the process. The overall grinding and vibration parameters are as follows:

- Wheelspeed: 30 m/s
- Workspeed: 50 mm/s
- Vibration frequency: 275 Hz
- Vibration amplitude: 15 μm (Peak)
- Depth of cut: 15 μm

5. Grinding and results

The overall results of all wheels and workpiece materials are presented next.

5.1. Grinding Trials with 454A 601 L 7G V 3 Wheel

In the first set of results the performance of medium grain-medium grade grinding wheel is presented for all three workpiece materials. The graphs in Fig. 4 and 5 show the variation of forces during conventional and vibration-assisted grinding whereas Fig 6 depicts the difference of surface roughness between the two methods.

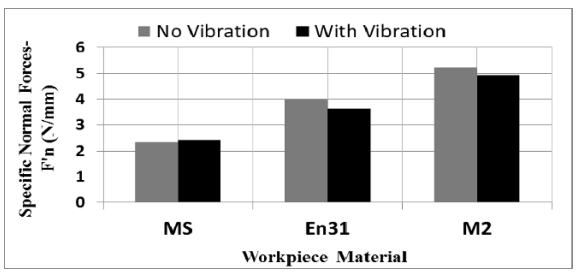

Fig. 4. Specific normal forces for 454A 601 L 7G V 3 wheel.

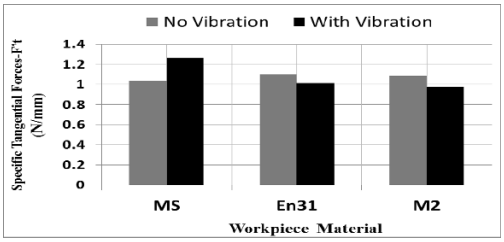

Fig. 5. Specific tangential forces for 454A 601 L 7G V 3 wheel.

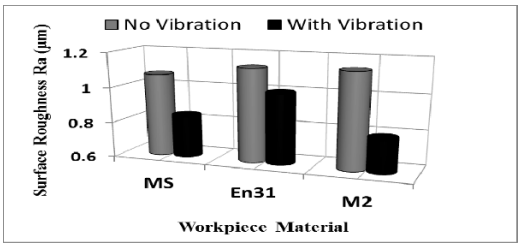

Fig. 6. Surface roughness for 454A 601 L 7G V 3 wheel.

According to the graphs in Fig. 4 and 5 vibration assisted grinding performed very well using a medium grain wheel to grind hard materials. The applied vibration provided a reduction of 10% for En31 normal forces whereas a similar reduction was achieved for M2 tool steel material. However, observation from the mild steel cutting forces shows an increase with the medium grain wheel along with the application of vibration. The reason is that soft materials require harder grade wheels with coarse grain sizes. In this case the wheel clogged easier and resulted in higher forces. Better surface finish, 30.7% for M2 tool steel. In this case the wheel is semi-friable which means that it can produce high surface quality along with high stock removal. In friable wheels the abrasive grains break easier by the impact and generate the self-sharpening process during grinding. The vibration led to a better surface finish in all of workpiece materials due to the induced lapping process.

5.2. Grinding Trials with Altos Wheel

The use of the porous grinding wheel and the applied vibration led to the reduction of cutting grinding forces. An overall reduction in cutting forces is observed. A better performance is seen when machining hardened materials, i.e. 23.6% reduction in tangential forces while grinding M2 hardened steel. However, mild steel did not respond well with the application of vibration as no significant reduction was observed in this test. This may be explained by the ductility and the ability of the material to deform elastically to great extent without actual fracture. The high friability of the wheel causes

fast and easy fracture of its grains. This type of wheels performs better with hard steel.

The results of surface roughness in Fig. 8 are not conclusive, however it points to a fact that the surface finish depended more on the wheel surface structure rather than the process. Therefore, surface roughness did not vary and only a 7.6% improvement was observed with the En31 and a smaller decrease in surface roughness for mild steel. High porous wheels with very open structures perform much better in wet grinding applications as they allow better insertion of the coolant and lubricant through their pores. Thus, there is a faster and more efficient delivery of the coolant lubricant to the grinding zone.

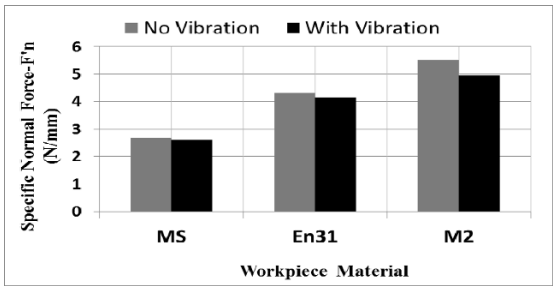

Fig. 7. Specific normal forces Altos wheel.

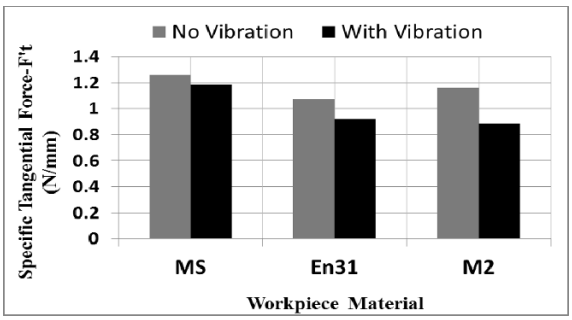

Fig. 8. Specific tangential forces Altos wheel

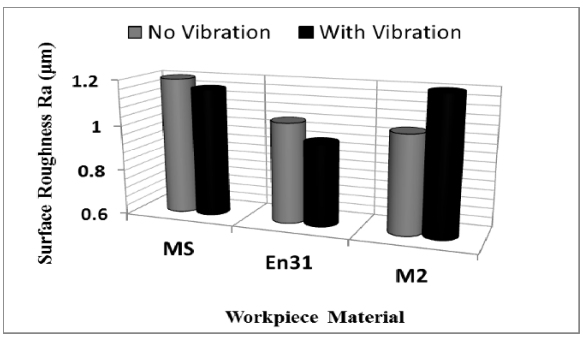

Fig. 9. Surface roughness for Altos wheel

6. Conclusions

The superimposition of vibration into a surface grinding process was achieved using a simplified vibrating jig. A complete study of the frequency response of the machine tool and the vibrating jig was undertaken. Three different materials and two grinding wheels were investigated in terms of process performance in conventional and vibration-assisted grinding. One of the key findings is that the induced vibration improved the performance of the process in terms of workpiece surface quality and the decrease the grinding forces, which was marginal in some cases. Another finding was that the nature and properties of the abrasive wheels play a vital role in specific applications. Grain size, hardness and structure of the wheel should be taken into account. Regardless of the combination wheel and the workpiece, the application of vibration secured some advantages over conventional grinding. Also these findings open a scope to apply this technique to improve fluid delivery in cases such as High Efficiency Deep Grinding.

References

[1] Malkin, S. (1989) 'Grinding Technology-Theory and Applications of Machining with Abrasives' Ellis Horwood, Chichester.

[2] Liang, Z., Wu, Y., Wanga, X., Zhao, W. (2010) 'A new two-dimensional ultrasonic assisted grinding (2D-UAG) method and its fundamental performance in monocrystal silicon machining' International Journal of Machine Tools & Manufacture, v50 issue 8 pp728–736.

[3] Tawakoli, T. & Azarhoushang, B. (2008) 'Influence of ultrasonic vibrations on dry grinding of soft steel' International Journal of Machine Tools & Manufacture, v48 pp1585– 1591.

[4] Babitsky, V.I., Kalashnikov, A.N., Meadows, A., Wijesundara, A.A.H.P. (2003) 'Ultrasonically assisted turning of aviation materials' Journal of Materials Processing Technology v132 pp157–167.

[5] Moriwaki, T. & Shamoto, E., (1991) 'Ultraprecision Diamond Turning of Stainless Steel by Applying Ultrasonic Vibration' Kobe University Japan vol.40 No.1

[6] Zhang, B., Hu, Z., Luo, H., Deng, Z. (2006) 'Vibration-Assisted Grinding – Piezotable Design and Fabrication' Nanotechnology and Precision Engineering Vol.4 No.4 pp283-289.

[7] Zhong, Z. W., Yang, H. B. (2004) 'Development of a vibration Device for Grinding with Microvibration.' Materials and Manufacturing Processes 19:6, pp: 1121-1132

[8] Babitsky, V.I., Kalashnikov, A.N., Meadows, A., Wijesundara, A.A.H.P. (2003) 'Ultrasonically assisted turning of aviation materials' Journal of Materials Processing Technology v132 pp157–167

[9] Batako, A.D.L & Tsiakoumis, V. "A simplified Innovative Method of Vibration-Assisted Grinding of Hardened Steel: Fixture/Machine Tool Response and Process Performance" International Journal of Machine Tools & Manufacture. IJMACTOOL-S-11-00812-1.

5-17

Investigation on the effect of cutting parameters on heat partition into multilayer coated tools in HSM

M. Fahad, P.T. Mativenga, M.A. Sheikh
School of Mechanical, Aerospace and Civil Engineering, The University of Manchester, M13 9PL, UK

Abstract. The determination of thermal loads and their distribution during dry or high speed machining can be important in predicting cutting tool performance. In this study, thermal aspects during high speed turning of AISI/SAE 4140 with commercially available coated (TiN, TiCN and Al_2O_3) tools with different coating schemes are investigated. High speed machining was conducted over a wide range of cutting velocities between 314 and 879 m/min. In addition finite element modelling was carried out to evaluate heat load distribution into the cutting tool. The work shows that the tool-chip contact conditions and coating layer deposition schemes are imperative in controlling the heat distribution into the cutting tool.

Keywords: Multilayer coated tools, heat partition, finite element modelling, high speed machining, tool-chip contact, sticking and sliding.

1. Introduction

During machining a large part of the power consumed is converted into heat [1] and the flow of heat into the cutting tool during machining is a critical issue which leads to thermally activated wear mechanism and hence premature tool failure [2]. To overcome the problems which arise in high speed machining (HSM), new tool materials and coating materials/compounds have been and are being developed and deposited on cutting tools to improve tool performance. The use of these thin, hard and sometimes thermally insulating coatings can reduce heat partition into the cutting tool [2, 3].

It is widely accepted that heat generation during machining and its distribution into the cutting tool depends such as cutting forces, tool-chip contact length, chip compression ratio and thermo-physical properties of the cutting tool material [4]. The focus of this article is to study and establish the effect of different cutting parameters/factors on heat partition into the cutting tool. This was conducted by turning AISI/SAE 4140 workpiece with multilayer coated tools. Evaluation of heat partition into the cutting tools was carried out by using experimental data along with finite element modeling (FEM).

2. Evaluation of heat partition into the cutting tool

Evaluation of heat partition into the cutting tool insert was conducted using cutting test data and finite element (FE) transient thermal analysis using commercial code Abaqus/Standard 6.10-1. The modeled inserts were carbide with geometry TCMT 16T308 (restricted contact length groove type). The insert and tool holder were modelled in a CAD software and imported into the FE software. Temperature dependent thermal properties [5] were assigned to each part of the coating tool system (i.e. coatings, shim seat and cutting tool holder). A four-node tetrahedral heat transfer element DC3D4 was used for the whole assembly of the coated tool system. A single element for each layer of coating was modelled because it was found to result in the least element aspect ratio distortion. Initial temperature and the far end surface of the tool holder were set at room temperature (25 ^{o}C on the day). Convective heat transfer coefficient for the entire model, except for the tool-chip contact area, was specified as h = 20 W/m^2 ^{o}C [6]. All parts of the cutting tool system i.e. coated insert, the shim seat and the tool holder were assumed to be in perfect contact. A constant heat flux was considered in the width of cut direction.

Thermal load q_{st} applied on the tool-chip contact length was calculated using experimental data using equation 1,

$$q_{st} = \tau_{sh} V_{ch} \quad (1)$$

where, τ_{sh} and V_{ch} are shear stress and chip flow velocity respectively. The shear stress was evaluted from the friction force along the rake face normalised over the contact area. Due to the presence of both plastic (sticking) and elastic (sliding) regions along the tool-chip contact length, a uniform thermal load was applied in the sticking zone and a non-uniform scheme (linearly decreasing to zero) in the sliding zone. This scheme has been used by other reseachers before [3, 7, 8].

Initially 100% of the calculated heat flux (from equation 1) was applied on the tool chip contact area in the FE model for the same duration as the machining

contact time. The applied heat flux was successively reduced after each simulation until the minimum acceptable difference was achieved between simulated and experimental temperatures on preselected paths (i.e. Path-1 and Path-2) on the rake face of cutting insert as shown in Fig. 1. The percentage of heat flux at which the FE and experimentally measured temperatures were matched, was considered as the percentage of the heat entering the cutting tool.

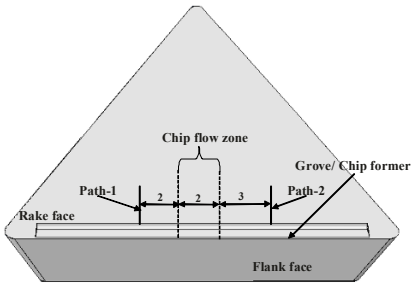

Fig. 1. Temperature measurement locations

3. Cutting tests and results

Nearly orthogonal (with 91° approach angle) dry (without coolant) turning tests were conducted on a semi automated Dean Smith and Grace Lathe machine between the cutting speeds of 314 m/min and 879 m/min. The feedrate and the width of cut were kept constant at 0.16 mm/rev and 2 mm, respectively. A tube of AISI/SAE 4140 (a low carbon high tensile strength alloy steel) with 2 mm thickness and external diameter of 200 mm was used as the workpiece material. Commercially available CVD deposited cutting tool inserts, coated in series and functionally graded, from Iscar (TS-1), SECO (TS-II) and Sandvik Coromant (TG) with ISO specification TCMT 16T308 (restricted contact length groove type) were used. Coating specifications and the thickness values measured using SEM are given in Table 1.

Temperature measurements were obtained by using an infrared thermal imaging camera, FLIR CAM SC3000 equipped with ThermaCAM Researcher package. Emissivity values in the range of 0.4 to 0.65 for Al_2O_3 and 0.2 to 0.3 for TiN [5] were used for the calibration of the camera during the cutting tests.

Table 1. Average thickness values of coatings deposited

Coatings	TS-I (µm)	TS-II (µm)	TG (µm)	
			Rake face	Flank face
TiN	2.5	-	-	2
Al_2O_3	4.5	10	7	7
TiCN	8.2	8	7	7

Cutting forces were measured using a Kistler three-component piezoelectric dynamometer type 9263 along with data acquisition software. Figure 2 shows the variation of cutting forces with cutting velocity. It can be seen that as the cutting velocity increases, cutting forces decrease for all three cutting tool inserts.

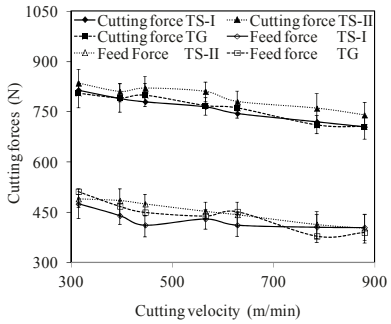

Fig. 2. Variation of cutting forces with cutting velocity for TS-I, TS-II and TG tools

Figure 3 shows the variation of tool-chip contact area on the rake face with cutting velocity which was measured using SEM. TS-I insert has the lowest tool-chip contact area in the entire range of the cutting velocity (i.e. from 314 - 879 m/min). The percentage reduction in the contact area between cutting speed of 314 m/min and 879 m/min for TS-I, TS-II and TG tools is 25%, 31% and 36% respectively.

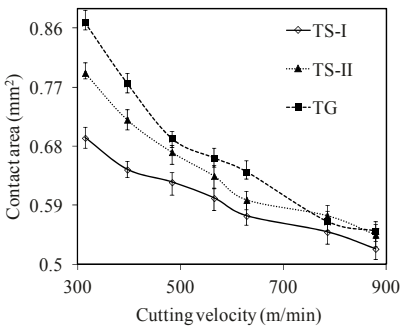

Fig. 3. Variation of tool chip contact area with the cutting velocity

Further investigations were carried out within the contact length to distinguish between sticking and sliding zones. SEM-Energy-Dispersive X-ray Analysis (EDXA) was conducted to evaluate the percentage of Fe (iron) concentration on the tool-chip contact length (Table 2).

Figure 4 shows the variation of heat partition into the cutting tool inserts with cutting velocity. It can be noted that heat fraction flowing into the cutting tool inserts decreases as the cutting speed increases. A reduction in thermal conductivity of Al_2O_3 coating for higher cutting velocities gives a lower heat partition into the cutting tool in case of TS-II and TG. The reduction in heat partition from cutting speed 314 m/min to 879 m/min for TS-I, TS-II and TG inserts is 61%, 68% and 63%, respectively.

Table 2. Percentage of sticking (St) and sliding (Sl)

Cutting velocity (m/min)	TS-I		TS-2		TG	
	St (%)	Sl (%)	St (%)	Sl (%)	St (%)	Sl (%)
314	60	40	55	45	54	46
395	58	42	52	48	51	49
446	55	45	50	50	47	43
565	51	49	48	52	45	55
628	44	56	40	60	38	62
785	40	60	35	65	34	66
879	35	65	29	71	25	75

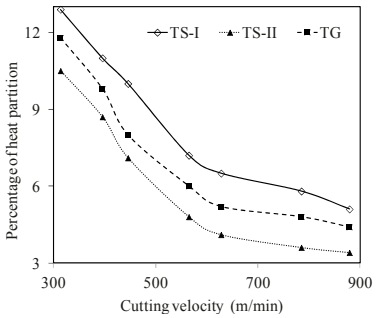

Fig. 4. Variation of heat partition into the cutting tools with cutting velocities

4. Discussion

Figures 5 (a), (b), (c) show the correlation coefficient between heat partition into the cutting tool and cutting parameters; compression ratio, cutting force, feed force and tool-chip contact length. It can be noted that the correlation coefficient (*R*) of heat partition is above 90% for chip compression ratio and above 88% for cutting forces for all three inserts. The correlation coefficients between heat partition and chip compression ratio and cutting force suggest that heat distribution into the cutting tool is directly related to these two parameters. Thinner chips produce lower chip loads on the tool rake face and in turn reduces the real tool-chip contact area as compared to the apparent area of contact between the tool and the chip. According to Trent, reduction in the real area of contact gives rise to sliding contact between the chip and the tool rake face [1].

Figure 6 shows a decrease in tool-chip contact length as the chip compression ratio decreases. The lighter chips at higher temperatures curl-up and depart early from the tool rake face hence give smaller contact area. From Fig. 5 it is clear that the correlation between the feed force and heat partition is above 88%. This can be attributed to the coefficient of friction between the chip and the tool rake face. Lower value of coefficient of friction gives lower feed forces and hence lowers heat partition into the cutting tool. This coefficient of friction was calculated from cutting forces, for a 0^O rake angle tool, it is simply the ratio between feed forces and cutting forces. It can be noted from Fig. 7 that in case of TS-II and TG inserts, the reduction in the coefficient of friction is 9% and 14% respectively from cutting speed of 314 m/min to 879 m/min

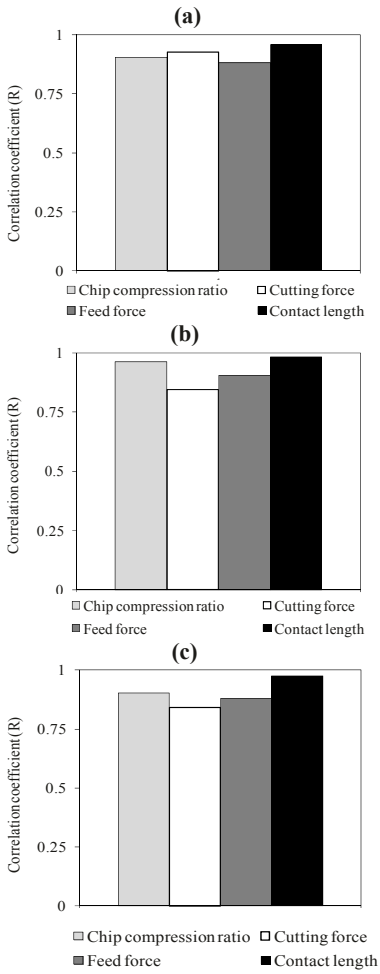

Fig. 5. Correlation coefficient of cutting parameters with heat partition of (a) TS-I (b) TS-II (c) TG cutting tools

The coefficient of friction in case of TS-I at cutting speed of 314 m/min is lower than the other two inserts (i.e. TS-II and TG), this is due to the excellent tibological properties of TiN at lower temperatures. But as the cutting speed increases no significant reduction is observed which is only 1.7% from cutting speed of 314 m/min to 879 m/min. This is due to TiN poor thermal and chemical stability and higher surface roughness at elevated temperatures [9]. Moreover, the poor chemical stability of TiN at higher temperatures allows the chip material to stick on the rake face [5]. This, in turn, allows the uniform shear stress distribution to prevail within the contact area and hence leads to higher heat partition into the cutting tool. A significant reduction in the coefficient

of friction for TS-II and TG cutting tools is due to the presence of Al_2O_3 top layer. Al_2O_3 has a self-lubricating ability at higher temperatures [10].

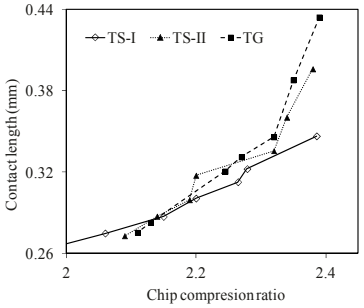

Fig. 6 Variation of tool-chip contact length with chip compression ratio

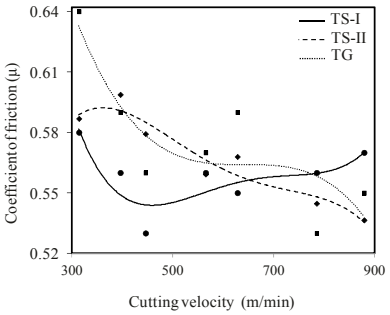

Fig. 7 Variation of coefficient of friction with cutting velocity

It can be noticed from Fig.5 (a), (b) and (c) that the highest correlation coefficient is for the contact length. Therefore, it can be argued that heat partition into the cutting tool is significantly sensitive to contact length. A larger contact area increases the heat distribution into the cutting tool and vice versa [11]. On the contrary, it can be argued from Fig. 3 that despite the contact area in case of TS-I insert being the lowest, the heat partition is highest (Fig. 4) as compared to other cutting inserts (TS-II and TG). The reason for higher heat partition in case of TS-I is the larger length of sticking contact as compared to the other two inserts (Table 2). The lower heat partition in case of TS-II and TG is attributed to smaller sticking zone. Smaller sticking zone is favourable up to some extent but if reduced further, it shifts the higher temperatures to a narrow zone near the cutting edge and leads to premature tool failure [5].

It can be argued that the heat partition into the TS-I tools is the highest due to the presence of TiN top coating. But in case of TS-II and TG tools, all the parameters discussed earlier i.e. tool chip contact, sticking and sliding contact regions are comparable, especially at higher velocities. Heat partition is lower for TS-II insert for all cutting velocities. This could be due to the 10 μm layer of Al_2O_3 and cumulative thickness (18 μm) of multilayers ($TiCN/Al_2O_3$) compared to 7 μm fo Al_2O_3 and cumulative thickness of 14 μm ($TiCN/Al_2O_3$ on rake face) for the TG insert.

5. Conclusions

In this study the presence of TiN as a top layer in TS-I inserts produced a smaller tool-chip contact length as compared to Al_2O_3 (in inserts TS-II and TG). However, due to the larger sticking zone in case of TS-I the amount of heat transfer was higher. Therefore, it can be concluded that, although, the tool-chip contact length is an important process parameter to heat partition into the cutting tool, a lower contact length does not guarantee lower heat partition. The size of the seizure zone is a critical consideration. This implies that the selection of top coating for a cutting tool insert is crucial for efficient HSM.

References

[1] Trent EM, Wright P, (2000) Metal cutting. Fourth Edition, Butterworth-Hwineman, Boston, MA. 85.

[2] Fahad M, Mativenga PT, Sheikh M A, (2011) Finite element methods in manufacturing process. Chap.2: ISTE Wiley, London, 45.

[3] Akbar F, Mativenga PT, Sheikh MA, (2009) On the heat partition properties of (Ti,Al)N compared with TiN coating in high-speed machining. Proceedings of the Institution of Mechanical Engineers, Part B: Journal of Engineering Manufacture, 223(4): 363-375.

[4] Akbar F, (2009) An investigation of heat partition in high speed machining using uncoated and coated tools. PhD Thesis, School of Mechanical, Aerospace and Civil Engineering, The University of Manchester.

[5] Fahad M, Mativenga PT, Sheikh MA, (2011) A comparative study of multilayer and functionally graded coated tools in high-speed machining. International Journal of Advance Manufacturing Technology,DOI 10.1007/s00170-011-3780-x.

[6] Yen YC, Jain A, Chigurupati P, Wu WT, Altan T, (2004) Computer simulation of orthogonal cutting using a tool with multiple coatings. Machining Science and Technology, 8(2): 305-326.

[7] Tay AE, Stevenson MG, Davis DG, (1974) Using the Finite Element method to determine temperature distribution in orthogonal machining. Proceedings of Institution of Mechanical Engineers, 188(55): 627-638.

[8] Wright PK, Mccormick SP, Miller TR, (1980) Effect of rake face design on cutting tool temperature distributions. Transaction of ASME, Journal of Engineering for Industry, (102):123-128.

[9] Wilson S, Alpas AT, (2000) Tribo-layer formation during sliding wear of TiN coatings, Wear, 245(1-2):223-229.

[10] Xiao H, Yin J, Senda T, (2008) Wear mechanism and self lubrication of engineering ceramics at elevated temperatures. Key Engineering Materials, (368-372):1092-1095.

[11] Abukhshim NA, Mativenga PT, Sheikh MA, (2005), Investigation of heat partition in high speed turning of high strength alloy steel. International Journal of Machine Tools and Manufacture, 45(15):1687-1695.

5-18

Effect of key process variables on effectiveness of minimum quantity lubrication in high speed machining

I. H Mulyadi and P.T. Mativenga
School of Mechanical, Aerospace and Civil Engineering, The University of Manchester, Manchester, M13 9PL, UK

Abstract. A great concern about environmental impacts of manufacture as well as the need to reduce cost and cycle times raises interest in dry high speed machining (HSM). Many researchers have reported the feasibility of using minimum quantity lubricants (MQL) in HSM. However, the selection of optimum cutting parameters for MQL application has not received a systematic study. In this paper, the existing knowledge on near dry machining is critically reviewed and this then leads into an experimental evaluation of key process variables. Taguchi experimental design was used to define the dominant process parameters and the optimum setting for minimising tool wear and machined surface roughness. The results show that the selection of MQL quantity is the most dominant factor in improving wear performance and the use of lower cutting speeds and higher chip thickness to cutting edge radius ratio (more efficient cutting) leads to better wear performance when machining tool steel. This can be a strategy for roughing operations. The use of feed per tooth lower than the tool edge radius can help in improving surface finish in finishing operations. The work is an important industrial guide for near dry milling processes and in identifying key areas for process improvement.

Keywords: High speed machining, minimum quantity lubrication, key process variables

1. Introduction

Cutting fluids play a significant role in cutting processes. They have two main objectives. Firstly, cooling down cutting tools, so that tool temperature can be reduced to a certain level, helps minimise thermally activated wear. Secondly, lubricating the contact areas where the friction occurs. These contact areas are the tool-chip interface and tool-workpiece interface. In addition, cutting fluids help by flushing off the chips from the machining zones. However, extensive use of cutting fluids has a negative impact on the environment and human health [1,2]. Machado and Wallbank [3] did a series of cutting tests using a small quantity of cutting fluids. The authors concluded that the machining processes only require a certain amount of cutting fluid quantity depending on the process.

A method that could be employed to mitigate the impact of using cutting fluid is dry machining [4]. For processes such as the intermittent milling process (cyclic cutting hence heating and cooling), dry machining is a promising candidate. Viera et al [5] compared dry machining and wet machining during face milling of H640 steel and reported that dry milling provided the best performance in terms of reducing tool wear and improving surface finish. The effectiveness of cutting fluid when machining at high cutting speed was questioned.

In high speed machining (HSM), working at higher cutting speed leads to increased thermal loads during the cutting process. Consequently, this increases interface temperature and decreases tool life [6]. Sometimes introducing flood coolant leads to thermal shock and hence the interest in machining dry or with minimum cutting fluids. This is particularly interesting to develop dry high speed machining for difficult-to-cut materials [7] where traditionally copious amounts of cutting fluids are used. It has been noted that, more process development is required to achieve widespread use of dry machining in industry [8].

Minimum quantity lubrication (MQL), also known as Near Dry Machining (NDM) can be a favourable machining technology [9, 10, 11]. However, there are contradicting results regarding the application of MQL in machining. For example, Rahman et al [9] reported that MQL was suitable only for low cutting speeds, yet, while, using cutting fluids of different viscosity, Liao et al reported that MQL was beneficial for both high and low cutting speed regimes [11]. In addition, several studies have investigated the use of MQL method [12-18]. Unfortunately, most research on MQL was focused on the benefits and feasibility of this technology [19] and not on performance optimization.

The aim of this study is to identify the significance of key process variables in MQL performance and fill the knowledge gap regarding optimum settings for machining with MQL.

2. Experimental details

The optimisation of cutting variables in MQL application was done for H13 tool steel. In high speed milling the practice is to use lighter cuts and higher table feeds. The use of lower depth of cut and feed per tooth implies that the size effect in relation to the tool edge radius needs to be considered. In this work the depth and feed per tooth are converted into a size effect ratio by relating them to the tool edge radius. Selection of the cutting parameters level was adapted to suit the high speed milling requirements. The volumetric flow rate levels for MQL parameter were selected according to a preliminary test which was done to quantify volumetric output of the supply system on the Mikron HSM 400 machine tool. The MQL was ECOLUB 2032 and this was delivered at 4 bar pressure through 2 nozzles at 45 degrees to the tool feed direction. Taguchi L_9 orthogonal array was selected as an experimental design. The factors and their levels considered are shown in Table 1. Taguchi design has been recognised in engineering and industry research for providing the optimum settings of control parameters [20].

Table 1. Factors and their levels for Taguchi L_9 orthogonal array

Parameters		Level		
Cutting speed (Vc), m/min	A	225	300	400
Feed per tooth-tool edge radius (Rf)	B	0.81	1.13	1.45
Depth of cut-tool edge radius (Rap)	C	1.37	1.82	2.42
Flow-rate (Q), ml/h	D	16.8	22.4	29.9

A down milling, end milling operation was performed to cut a H13 workpiece material on a Mikron HSM 400 milling machine. Test was performed using a tool diameter of 8 mm, mounted with rectangular TiAlN PVD coating tool inserts (IC928) manufactured by ISCAR. The edge radius of the inserts was evaluated to be 62 µm. Every set of experiments were repeated twice.

Surface roughness was measured using a Taylor Hobson Surtronic 3+ Talysurf surface roughness tester. The cut-off length and the evaluation length were set to 0.8 mm and 4mm, respectively. Furthermore, the images of flank wear land and rake face were captured using a Leyca Microscope. Subsequently, the magnitude of flank wear and contact length were measured by using an image processing software, Axio Vision release 4.8. The average flank wear and contact length were calculated from the data taken by 15 lines of measurement on the flank wear land of each worn insert.

3. Results and discussions

3.1. Importance of key process variables on tool life

Table 2 shows the experimental plan, while the results for flank wear and the signal-to-noise ratio (S/N) are shown in Fig. 1.

Table 2. Experimental Design and average flank wear response

Vc (m/min)	Rf	Rap	Q (ml/h)	VB_ average (µm)
225	0.81	1.37	16.80	64
225	1.13	1.82	22.40	63
225	**1.45**	**2.42**	**29.90**	**58**
300	0.81	1.82	29.90	63
300	1.13	2.42	16.80	65
300	1.45	1.37	22.40	67
400	0.81	2.42	22.40	68
400	1.13	1.37	29.90	60
400	1.45	1.82	16.80	61

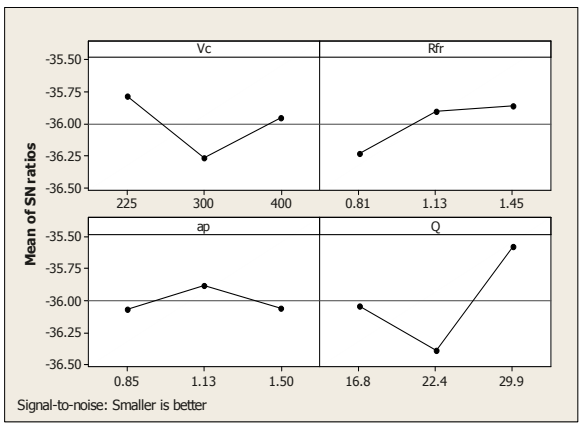

Fig. 1. S/N Ratio analysis for average flank wear

The results in Table 2 and Fig. 1 show that a low cutting speed (225 m/min), high feed per tooth to tool edge radius (Rf=1.45), moderate depth of cut-tool edge radius (Ra_p=1.82) and a high volumetric flow rate of cutting fluid (29.9 ml/h) gave the least flank wear. The low cutting speed is associated with lower cutting temperatures and hence lower average flank wear. This supports previous reports on the performance of MQL over a range of cutting speeds [9, 16, 18]. The higher feed to tool edge radius ratio implies a more positive rake angle and more efficient chip formation process.

In terms of reducing flank wear, the results of ANOVA analysis (Table 3) show that volumetric flow rates have the highest contribution (60%) followed by cutting speed (21%), feed-tool edge radius ratio (15%)

and depth of cut–tool edge radius ratio (of 5%). This dominance of MQL reflects the fact that the lubricant reduces friction hence lowering cutting tool temperature and promoting longer tool life.

Table 3. ANOVA analysis result for average tool wear

Source	Df	SS	MS	F	Cont.(%)	P
Vc	2	37.8	18.88	2017	21%	1E-12
Rfr	2	26.1	13.07	1396	15%	6E-12
Rap	2	8.2	4.11	439	5%	1E-09
Q	2	107.1	53.57	5723	60%	0.000
Error	9	0.1	0.01		0%	1.000
Total	17	179.35	89.64		100.00%	

Moreover, a subsequent analysis was carried out to predict the possible minimum average flank wear that can be achieved by the suggested optimal setting. By utilizing the statistical software MINITAB 15.03, it was found out that the minimum value of average flank wear was 56.60 µm. The result is similar to the statistical prediction calculation that was done manually by using 95% of confidence level. A confirmation test was performed and the actual minimum value of average flank wear at this optimum setting was measured to be 50 µm. Therefore, compared to the initial experiments, there was a 13.8 % decrease in flank wear gained by applying the optimum setting that was predicted by the Taguchi methods.

3.2 Importance of key process variables on surface roughness

Surface roughness is one of the important indicators for quality in a machining process. In this present investigation, the measured values are shown in Table 4 and the S/N ratio is shown in Fig. 2. Both sets of data show that a combination of moderate cutting speed, low feed-tool edge radius ratio, low depth of cut-tool edge radius ratio and low volumetric flow rate contributes to better-machined surface finish.

In finishing operations, in order to produce superior surface finish, the quantity of cutting fluid is less critical as indicated in the ANOVA analysis results given in Table 5. This supports Da Silva and Wallbank [21] who concluded that only small amount of lubricant is required to remove adhering broken off BUE out of the machined surface. The ANOVA analysis result shows that controlling feed-tool edge radius ratio followed by cutting speed and depth of cut-tool edge radius ratio is the hierarchy for improving the surface finish. The need for a low ratio of feed per tooth to the tool edge radius supports the improvement in surface finish that is obtained at a trade off between shearing and ploughing based cutting modes. This is also associated with the polishing effect.

Table 4. Experimental Data of surface roughness response

Vc (m/min)	Feed Ratio	Rap	Q (ml/h)	Ra_average (µm)
225	0.81	1.37	16.80	0.232
225	1.13	1.82	16.80	0.363
225	1.45	2.42	16.80	0.491
300	0.81	1.82	29.90	0.223
300	1.13	2.42	16.80	0.310
300	1.45	1.37	22.40	0.329
400	0.81	2.42	22.40	0.379
400	1.13	1.37	29.90	0.353
400	1.45	1.82	16.8	0.453

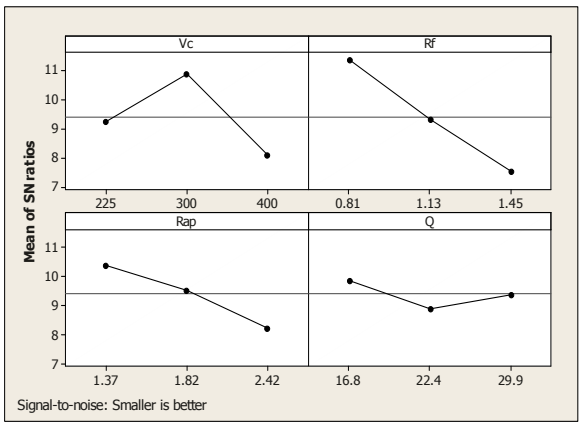

Fig. 2. S/N Ratio analysis of surface roughness response

Table 5. ANOVA analysis result for surface roughness

Source	Df	SS	MS	F	Cont.(%)	P
Vc	2	0.04	0.02	6.3	24%	0.019
Rf	2	0.07	0.03	11.2	42%	0.004
Rap	2	0.02	0.01	4.1	15%	0.055
Q	2	0.00	0.00	0.4	2%	0.666
Error	9	0.03	0.00		17%	
Total	17	0.15	0.07		100.00%	

Similarly, the predicted minimum surface finish was 0.157 µm Ra and the confirmation cutting test result was 0.150 µm Ra. Thus, comparing between the best results from the initial experiment and predicted optimum setting, a 33% improvement in surface finish can be obtained.

4. Conclusions

The motivation for this study was to establish optimum cutting conditions for the effective machining of tool steel under MQL conditions. It can be concluded that;

The rate of flank wear in MQL machining is significantly sensitive to the quantity of MQL. This is more dominant compared to the impact on tool wear of cutting variables of cutting speed, feed per tool and depth of cut. In this study, the highest quantity of MQL gave the lowest wear rate. Where surface finish is a constraint for example, in finishing passes when using MQL, the ratio of feed per tooth to tool-edge radius is the dominant factor to be manipulated in order to significant reduce surface roughness. This is so, when compared to changing cutting speeds or depth of cut-tool edge radius ratio or quantity of MQL. A strategy for MQL machining of tool steel is to undertake roughing passes at higher feed per tooth and moderate cutting speeds using the maximum quantity of MQL. The finishing pass operation can use the lowest feed per tool in order to exploit the size effect for improving surface roughness. It is possible to obtain sub-micro surface roughness of 0.150 μm Ra when machining tool steel. The fact that the optimum MQL quantity reported in the study was at the highest level tested suggests that there could be tool wear reduction benefits for setting MQL flow rate at values more than 29.9 ml/hour.

References

[1] P.M. Chazal, Pollution of modern metalworking fluids containing biocides by pathogenic bacteria in France: Re-examination of chemical treatments accuracy, European Journal of Epidemiology 11 (1995) 1-7.

[2] I. A. Greaves, et al., Respiratory health OF automobile workers exposed TO metal-working fluid aerosols: Respiratory symptoms, American Journal of Industrial Medicine 32 (1997) 450–459.

[3] A.R. Machado, and J. Wallbank, , The Effect of Extremely Low Lubricant Volumes In Machining, Wear 210 (1997) 76-82.

[4] G. Byrne, and E. Scholta, Environmentally clean machining processes-A strategic approach, CIRP Annals-Manufacturing Technology 42 (1) (1993) 471-474.

[5] J.M. Viera, et al., Performance of cutting fluids during face milling steels, Journal of Materials Processing Technology 116 (2001) 244-251.

[6] N. Narutaki, et al., High-speed machining of Inconel 718 with ceramic tools, CIRP Annals-Manufacturing Technology 42 (1) 1993 103-106.

[7] H. Schulz, and T. Moriwaki, High–speed machining, Annals of the ClRP 41 (1992) 637-643.

[8] P.S. Sreejit, and B.K.A. Ngoi, Dry machining: Machining of the future, Journal of Materials Processing Technology 101 (2000) 287-291.

[9] M. Rahman M, et al., Experimental evaluation on the effect of minimal quantities of lubricant in milling. International Journal of Machine Tools and Manufacture 42 (2002) 539–547.

[10] M.C. Kang, et al., Effect of the minimum quantity lubrication in high-speed end-milling of AISI D2 cold-worked die steel (62 HRc) by coated carbide tools. Surface and Coating Technology 202 (2008) 5621-5624.

[11] Y.S. Liao, et al., Feasibility study of the minimum quantity lubrication in high speed end milling of NAK 80 hardened steel by coated carbide tool, International Journal of Machine Tools and Manufacture 47 (2007) 1667-1676.

[12] Cheng-Hsien Wu and Chih-Hsien Chien, Influence of lubrication type and process conditions on milling performance, Proc. IMechE Part B: J. Engineering Manufacture 221 (2007) 835-843.

[13] P.W. Marksberry, and I.S. Jawahir, A comprehensive tool-wear/tool-life performance model in the evaluation of NDM (near dry machining) for sustainable manufacturing, International Journal Machine Tools and Manufacture 48 (2008) 878–886.

[14] T. Ueda, et al., Effect of oil mist on tool temperature in cutting, Journal of Manufacturing Science and Engineering, Transaction of the ASME 128 (2006) 130-135.

[15] J. Sun et al., Effects of coolant supply methods and cutting conditions on tool life in end milling titanium alloy, Machining Science and Technology 10 (2006) 355-370.

[16] Iqbal A et al., Optimizing cutting parameters in minimum quantity lubrication milling of hardened cold work tool steel, Proceedings of the IMechE Part B: Journal of Engineering Manufacture 223 (2006) 43-54.

[17] T. Obikawa et al., Micro-liter lubrication machining of Inconel 718, International Journal of Machine Tools and Manufacture 48 (2008) 1605-1612.

[18] T. Thepshonti et al., Investigation into minimal-cutting-fluid application in high-speed milling of hardened steel using carbide mills, International Journal of Machine Tools and Manufacture 49 (2009) 156-162.

[19] V.P. Astakhov, Metal cutting theory foundation of near-dry (MQL) machining, Int. J. Machining and Machinability of Materials 7 (1/2) (2010) 1-16.

[20] Peace G S, Taguchi Methods : A Hands-On Approach to Quality Engineering, Addison-Wesley, Massachusetts, 1993, p. 2.

[21] Da Silva M.B., and J. Wallbank, Lubrication and application method in machining, Industrial Lubrication and Tribology, 50(4) 1998 149-152.

5-19

Development of a free-machining (α+β) Titanium alloy based on Ti 6Al 2Sn 4Zr 6Mo

M. S. Hussain, C. Siemers and J. Rösler
Institut für Werkstoffe, Technische Universität Braunschweig, Braunschweig, Germany

Abstract. Titanium alloys are widely used in the aerospace and power generation industries due to their high specific strength and corrosion resistance. On the other hand, Titanium alloys like the modern (α+β) titanium alloy Ti 6Al 2Sn 4Zr 6Mo (Ti-6246) are difficult to machine due to the formation of long chips which hinders automated manufacturing. In the present study, small amounts of Lanthanum have been added to the standard alloy Ti-6246 to improve its machinability, i. e. to reduce the chips' length. As Lanthanum and Tin form the La_5Sn_3 intermetallic phase, the 2% of Tin had to be replaced by 3% of Zirconium. The matrix of Ti 6Al 7Zr 6Mo 0.9La (Ti-676-0.9) containes pure metallic Lanthanum precipitates which have a relatively low melting point compared to Titanium. During machining of this new free-machining alloy short and strongly segmented chips are observed enabling automation of machining operations. This can be explained by softening of Lanthanum particles during segmented chip formation. The microstructure, phase composition and mechanical properties of the new free-machining alloy were analysed after different thermo-mechanical treatments.

Keywords: Titanium, Ti6Al 4V, Lanthanum, machinability, free-machining alloy

1. Introduction

Titanium alloys have been widely used in aerospace, biomedical and chemeical plant industries because of their good strength to weight ratio and superior corrosion resistance. However, machining of Titanium alloys is difficult due to their poor machinability [1]. This difficulties arise from the physical, mechanical and chemical properties of Titanium. Due to the relatively poor thermal conductivity of Titanium, heat generated by the cutting action cannot diffuse quickly into the chips' material so that heat is concentrated in front of the rake face of tool. Low modulus of elastitcity of Titanium results in springback during the cutting action causing chatter, deflection and rubbing problems. The high strength of Titanium alloys is maintained up to elevated temperature so that a high amount of engery is needed to form a chip [2]. The high chemical reactivity of Titanium limits the number of possible materials for the cutting tools as Titanium has a strong affinity to elements used in cutting tools at operating tempareture. This causes galling, welding, and smearing leading to rapid tool destruction and, in addition, decreases the quality of the finished workpiece [2]. Finally, machining operations cannot be automated due to the formation of long chips. These chips have to be removed from the process zone by an operator [3].

In machining, three different types of chips are known to form, namely, continous chips having a constant chips thickness, segmented chips showing a saw-tooth-like geometry and completely separated segments. (α+β)-Titanium alloys like Ti 6Al 2Sn 4Zr 6Mo(Ti-6246) form segmented chips for many different machining process and for a wide range of cutting speeds and cutting depths [4]. Segmented chip formation can be explained as follows: During the beginning of the cut, the tool is penetrating the workpiece and the material is dammed in front of the tool. The plastic deformation is concentrated in a narrow zone, the so-called primary shear zone, Most of the energy used for the plastic deformation is transformed into heat in the primary shear zone which leads to local softeneing of the material and, hence, to the formation of segmented chips, The strain in shear bands can easily exceed 800% at strain rates up to 10^7 s^{-1}. The temperature in the shear band of titanium alloys can easily exceed 1000°C. The chip is afterwards guided along the rake face of the tool, the so-called secondary shear zone. The temperature at the end of the secondary shear zone can also rise to more than 900°C [4].

In the present study, the machinability and the chip formation process of Ti 6Al 2Sn 4Zr 6Mo (Ti-6246) and a modified alloy Ti 6Al 7Zr 6Mo 0.9La (Ti-676-0.9) alloy have been studied in CNC turning experiments. The microstructure of the resulting chips has been investigated by optical microscopy and scanning electron microscopy (SEM) including chemical analysis by energy dispersive X-ray spectroscopy (EDS).

2. Material and experimental procedure

2.1. Material and alloy production

Ti-6246 alloy was produced by the GfE Metalle and Materialien GmbH in Nuremberg, Germany. After 2x vacuum arc remelting (VAR) the alloy was forged from approx. diameter 200 mm to diameter 75 mm in the two-phase field followed by air cool and stress releif anneal.

For alloy modification, 0.9% of Lanthanum (La) have been added to improve the machinability, i. e. to reduce the chips' length [5]. Tin (Sn) was replaced by Zirconium (Zr) as Lanthanum and Tin form intermetallics like La_5Sn_3 during crystallisation. From earlier studies it is known that La_5Sn_3 particles do not lead to improved machinability of Titanium alloys as its dissolution temperature lies above 1500°C [6]. 3% Zirconium have been used instead of 2% Tin to ensure similar solid solution hardening and similar β-transus tempertures in both alloys. The final composition of the modified alloy was therefore Ti 6Al 7Zr 6Mo 0.9La (Ti-676-0.9).

To ensure similar starting conditions in the cutting experiments, the two alloys have been produced by plasma arc melting (PB-CHM) in a laboratory furnace with a capacity of about 300 g Titanium [7]. The standard Ti-6246 alloy (remelting of the as-received mateieral) and the modified alloy Ti-676-0.9 were melted and twice remelted to achieve a homogenous alloy. Finally, the alloys have been cast into a water cooled copper crucible of cylindrical shape (fast cooling). The rods had a diameter of 13.2 mm and a length of approx. 90 mm.

2.2. Turning Experiments

The two Titanium alloys have been subjected to turning experiments on a CNC lathe at conventional cutting speeds (v_c) between 30 m/min to 60 m/min. Cutting depths (a_p) of 0.5 mm and 1.0 mm have been used at a constant feed rate (f) of 0.1 mm/rev.

3. Results and Discussion

3.1. Microstructure and Phase Analyses

Both alloys consist of α' martensite only after casting as expected. As the solubility of Lanthanum in Titanium is extremely low at room temperature discrete particles (globular shape) with a high Lanthanum content are present mainly on the grain boundaries in Ti-676-0.9, see Fig. 1. The average particle size is about 2 µm

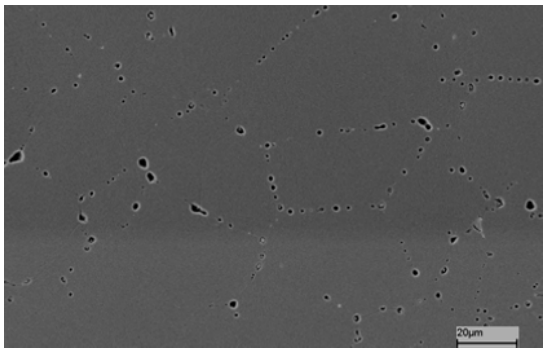

Fig. 1. Microstructure of Ti-676-0.9: Besides the Titanium matrix Lanthanum-rich particles are visible on the grain boundaries.

Hard X-ray (BW5, HASYLAB, DESY) investigations at modified CP-Titanium, Ti 6Al 4V (Ti-64) and Ti 5Al 5V 5Mo 3Cr (Ti-5553) alloys have shown that the precipitates consisted of metallic Lanthanum [8]. Hence, it is very likely that the particles in Ti-676-0.9 alloy are of metallic nature, too.

The grain size of Ti-6246 has been measured to 147 µm ± 2.1µm whereas the grain size of as cast sample of Ti-676-0.9 was 43 µm ± 1.5µm which shows that the Lanthanum particles act as a grain refiner in the new alloy during crystallization. Due to this observation, heat treatments at different temperatures have been carried out. It has been observed that no grain growth occures in Ti-676-0.9 alloy at temperatures below beta transus whereas grain growth has been observed in the standard Ti-6246 alloy in all heat treatments see Fig. 2. This once more confirms the grain size stabilisation effect of Lanthanum in (α+β)-Titanium alloys.

The β-transus temperature has been investigated by heating the sample to three different temperatures followed by water quenching. It was observed that β-transus of both alloys lie between 900°C and 915°C. As Lanthanum (α-stabiliser) is mostly present in precipitates and not dissolved in the matrix, it is obvious that Lanthanum does not affect the β-transus temperture.

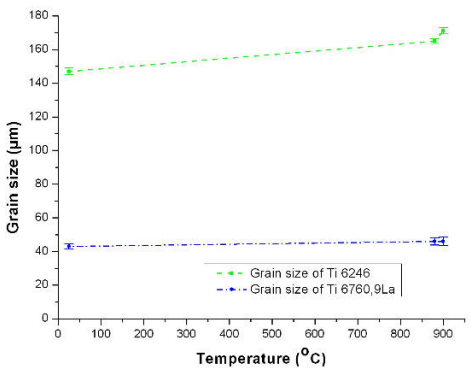

Fig. 2. Grain size with respect to temperature of both alloys.

3.2. Machinability

3.2.1. Chip Morphology

During machining of the standard Ti-6246 alloy long chips devloped in all cutting conditions whereas machining of modified alloy Ti-676-0.9 lead to the formation of short breaking chips, see Fig. 3.

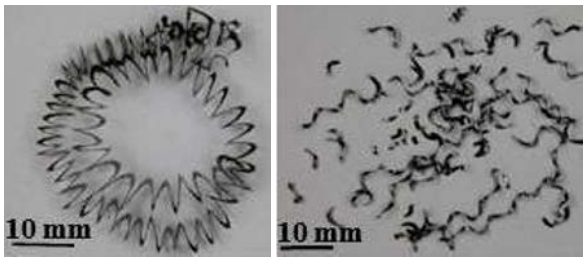

Fig. 3. Chips of Ti-6246 (left) and Ti-676-0.9 (right) alloys. The difference in the length of the chips is clearly visible.

This observation can be explained as follows: During segmented chip formation the temperature in the shear bands reaches or exceeds 1000°C, metallic Lanthanum particles (melting temperature: 918°C) which are present in zone of localized deformation will drastically soften or even melt once the segment starts to form. The adhesion between the segments will be diminished so that the chips fall apart either directly once the shear band forms or due to vibrations during further progress of the tool after the segment is completely developed. The chip separation is shown in Fig. 4.

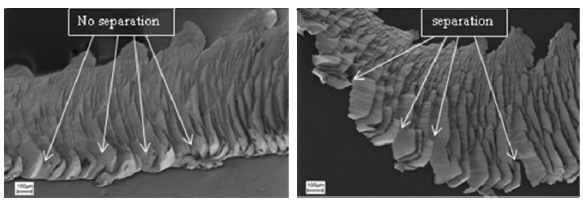

Fig. 4. Chip morphology of Ti-6246 (left) and Ti-676-0.9 (right). The top-down SEM images clearly show the chip separation in case of Ti-676-0.9 alloy.

Several benefiting effect result from the formation of short breaking chips: (1) As the chips are much shorter than in the standard alloy, the contact length between chip and tool decreases so that the temperature of the rake face also decreases. Hence, the tool wear is reduced. (2) As the contact pressure between tool and work piece is diminished, the surface roughness of the finished work piece is reduced. (3) Finally, automated machining processes are now possible as the removal of the chips by cooling fluids is now enabled.

3.2.2. Effect of Cutting Parameters on Chip Geometry

Cross sections of chips of the two Titanium alloys have been analysed by optical microscopy with resepct to their dependencies of the cutting parameters. Two different geometrical features of the chips, namley the degree of segementation (d_s, $d_s = (h_{max} - h_{min}/h_{max})$ and the segmented shear angle (ϕ_s) have been investigated, see Fig. 5.

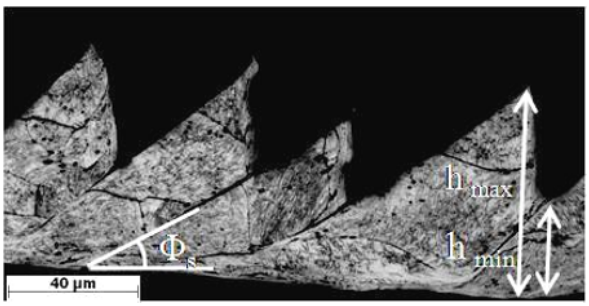

Fig. 5. Definition of geometrical parameters used for the comparison of different chips.

The degree of segementation increased with increasing cutting depth and cutting speed. In addition, it can be stated that the absolute degree of segmentation was higher ($0.5 \leq d_s \leq 0.8$) in chips of Ti-676-0.9 alloy compared to the standard alloy ($0.2 \leq d_s \leq 0.4$). Material separations (which also increase the degree of segementation) are visible in the primnary shear zone in case of Ti-676-0.9 alloy, see Fig. 6. The tendency for shear band separations increases with increasing cutting speed. The primary shear zones in Ti-6246 alloy on the other hand do not show any material separations. This once more shows that short chips in case of Ti-676-0.9 alloy are a result of reduced adhesion between the segments.

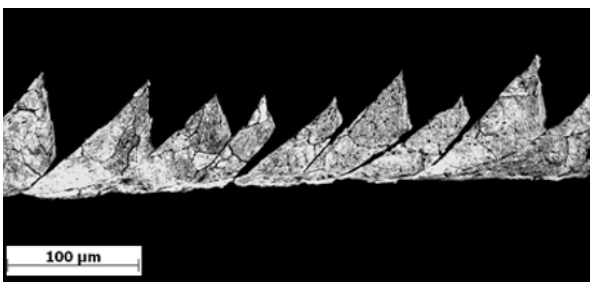

Fig. 6. Microstructure of Ti-676-0.9 alloy chips, $v_c = 40$ m/min, $a_p = 0.5$ mm, $f = 0.1$ mm/rev. The material separations in the primary shear zones are clearly visible.

In Ti-6246 alloy the segment shear angle has been measured between 40° and 45° independent of the cutting depth and cutting speed. The shear angle for Ti-676-0.9 alloy increases with increasing cutting speed and cutting

depth from about 30° to 57°. The results of the geometry measurements are summarised in Fig. 7.

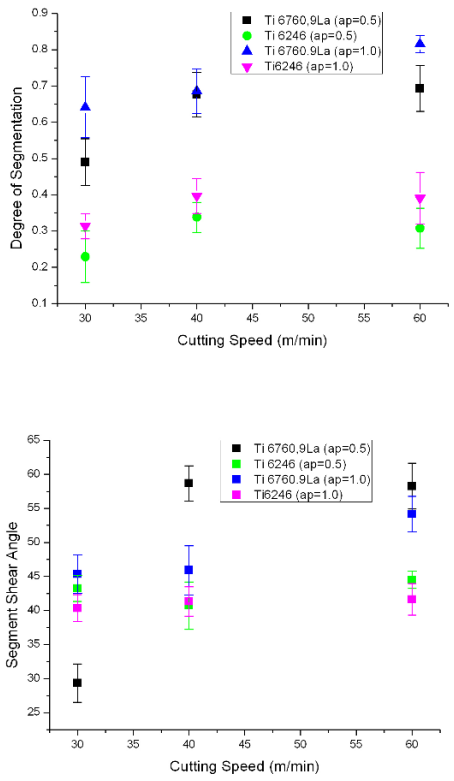

Fig. 7. Degree of segmentation of the chips (top) and segmented shear angle (bottom) for the tow different alloys as a function of cutting speed (v_c) and cutting depth (a_p).

4. Conclusion and Future Work

The machinability of (α+β)-Titanium alloys like Ti-6246 can be improved by the introduction of micrometer-size second-phase particles into the Titanium matrix. The size of the particles should not undercut 1 µm (which is the smallest shear band width observed in the experiments presented here) as otherwise the adhesion between the segments will not be small enough to produce short chips in machining. The melting point of the precipitates should be lower than 1000°C. These two requirements are fulfilled by the two rare earth metal elements Cerium (T_{Melt} = 698°C) and Lanthanum (T_{Melt} = 916°C). In our study, Lanthanum has been chosen to maintain the mechanical properties also to elevated temperature. Benefitting effects of such modified alloys are reduced tool wear, better surface quality and the possibility of automated machining, especially in turning and drilling operations. If in addition, the particles are mainly located on the grain boundaries, an effect of grain refinement is observed as well. Future work will now concentrate on the investigation of possible deformation routes like extrusion and forging and adequate heat treatment procedures for the modified alloy. Afterwards, physical and static and dynamic mechanical properties of the new modified alloy will be investigated to study the feasibility of industrial applications.

Acknowledgment: The research leading to these results has received funding from the European Union Seventh Framework Programme (FP7/2007-2013) under grant agreement No. PITN-GA-2008-211536, project MaMiNa. Financial support of the European Commission is therefore gratefully acknowledged.

References

[1] Peters M and Leyens C (2002) Titanium and Titanium Alloys, Wiley-VCH, Weinheim, Germany.

[2] Donarchie J (1988.) Titanium – A Technical Guide, ASM International, Metals Park, Ohio, USA.

[3] Lütjering G und Williams J C (2003) Titanium, Springer Verlag, Berlin, Heidelberg, Germany.

[4] Rösler J, Bäker M, Siemers C, (2005) Mechanisms of Chip Formation in: H.-K. Tönshoff and F. Hollmann (eds.), High Speed Machining, VCH-Wiley, Weinheim, Germany

[5] Siemers C, Laukart J, Zahra B, Rösler J, Spotz Z and Saksl Kl, (2011) Materials Science Form Vol. 690 262-265.

[6] Siemers C, Jencus P, Baeker M, Roesler J, Feyerabend F (2007): A new free machining Titanium alloy containing Lanthanum Proceedings of the 11th World Conference on Titanium (Ti-2007), Kyoto, Japan, Vol. I, pp. 709 – 712.

[7] Siemers C, Laukart J, Zahra B, Rösler J, Spotz Z and Saksl K, (2010) Proceedings of the COM2010, Section Light Metals 2010 - Advances in Materials and Processes, Vancouver, Canada, pp. 311 – 322.

[8] Technische Universität Braunschweig, Rösler J, Bäker M and Siemers C, (2004) German Patent DE 103 32 078, DPMA Publications.

[9] Siemers C, Laukart J, Zahra B, Rösler J, Rokicki P, Saksl K, (2011) Advanced Titanium Alloys containing Micrometer-Size Particles, Proceedings of the 12th World Conference on Titanium (Ti-2011), Beijing, China, (in press).

5-20

An improved setup for precision polishing of metallic materials using ice bonded abrasive tool

Boopalan M., Venkatarathnam G. and Ramesh Babu.
Department of Mechanical Engineering, Indian Institute of Technology Madras, Chennai, India – 600036

Abstract. This paper presents an improved setup for Ice Bonded Abrasive Polishing (IBAP) of materials with in-built refrigerating unit and temperature controller. Freezing of water into ice serves as a bond that can firmly hold the abrasives and aids to form a flexible tool for polishing. Unlike the earlier setup that made use of liquid nitrogen to prepare a IBAP tool, this work was attempted to develop a refrigerating unit that helps to prepare the tool in-situ and to enhance the life of tool by maintaining its temperature within reasonable limits. Preliminary experiments were attempted on Ti6Al4V alloy, copper and stainless steel in order to study the effectiveness of polishing of metallic materials with the improved setup.

Keywords: Bonded abrasive tool, Refrigeration, Ice.

1. Introduction

The functional performance of a material is directly influenced by the quality of surface generated by finishing process. Production of high precision components, used in various applications like optical systems, silicon wafers, solar cells, micro-electromechanical systems and medical applications, has been under the focus of attention for a long time.

Ultra fine surface generation processes essentially consume enormous time and require extreme care to produce fine and precise surfaces on the components. Hence, several efforts were made to develop efficient processes which can provide ultra-high precision with ease and also provide enough flexibility in handling of simple to complex parts made of high-strength and wear resistant materials.

In view of the complexity and non-deterministic nature of conventional polishing methods, several unconventional polishing processes, like chemical polishing, laser assisted polishing, electrochemical polishing, magneto-rheological polishing and chemical mechanical polishing methods, are developed over the recent times [1]. Among them, chemical mechanical polishing is widely used for planarization of materials to achieve high degree of surface intergrity with tighter tolerances. Certain difficulties in chemical mechanical polishing include precise feeding of slurry into polishing zone, flexibility of the process in polishing of simple to complex profiles, poor material removal rates, deflection of pad surface and periodic reconditioning of the pad.

Some of these drawbacks can be overcome with Ice bonded abrasive polishing (IBAP) process [2]. This process is a cryogenic type chemical mechanical polishing process where ice acts as a bonding medium to hold abrasives together for polishing of simple to complex surfaces. During polishing, certain amount of heat generated due to friction between tool and work surface causes ice to melt continuously thus exposing fresh abrasives for polishing. Studies have shown the production of nano-level surface finish i.e. Ra = 8nm on 304L stainless steel specimen with ice bonded abrasive polishing process [3]. In this setup, liquid nitrogen was poured into the slurry of water and abrasives in order to prepare the tool for polishing of flat specimen. But the tool prepared could be used only for about 15 minutes. Further, the tool prepared has shown certain inconsistency in its composition and structure due to over or under freezing of water in different regions of the slurry in the mould. Maintaining the temperature of the tool has been one of the challenges in this setup and has thus reduced the effective life of tool for polishing of the specimen.

With a view to enhance the life and effectiveness of ice bonded abrasive polishing tool, this paper covers the efforts made to develop a setup containing a refrigerating unit with an appropriate temperature control scheme for polishing of specimen. It presents the details of the refrigerating unit along with kinematic arrangement of IBAP setup. Preliminary studies were attempted to polish copper specimen with the improved setup. Based on the feasibility of setup for polishing of copper specimen, the studies were extended to polish Ti6Al4V and stainless steel specimen in order to demonstrate the effectiveness of this process for polishing different metallic materials.

2. Basis for the development of setup

A setup for in-situ preparation of IBAP tool was felt essential to polish specimen for a longer duration. Several factors influenced the generation of heat during polishing and has thus shortened the life of tool prepared by freezing the mixture of water and abrasives with liquid nitrogen in offline mode. Control over the temperature of the tool plays a crucial role in the preparation of tool and in polishing the specimen. In order to gain insight into various phenomenon that have contributed to thermal degradation of tool, an attempt was made to estimate the energy inputs to frozen tool i.e. heat input due to conduction, convection, radiation and friction between the tool and the work surface, by considering the configuration of existing setup.

Table 1. Energy losses due to different phenomena in IBAP tool

Mode	Theoretical heat addition (J/s)
Friction between tool and workpiece [4]	0.29
Convection (Top, bottom and radial)	40.39
Radial conduction	3.32
Motor heat	53.81

From the estimates listed in Table 1, it is clear that convection over the top, bottom and radial directions of IBAP tool and motor heat input are the major contributors in melting of ice into water and thus shortening the life of IBAP tool. Heat input into the tool due to radiation and friction are seen to be negligibly small. However, the frictional heat liberated between tool and work surface is sufficient to refresh the tool during polishing by way of melting of ice into water. In order to enhance the overall life of tool, several changes were made to bring out a new setup that can minimize the amount of heat input into the system. Modifications made in the configuration of the setup include:

- Refrigerant supply in the annulus between the inner and outer cylinder so as to reduce conduction and convection from the bottom;
- Insulation of outer cylinder to reduce the transfer of heat from the refrigerant to the ambience;
- Belt and pulley drive to offset the motor from IBAP tool so as to avoid the conduction of motor heat into the tool;
- Replacement of swing arm (over hanging beam) type workpiece holder with a straight flat arm (fixed beam) to hold and place the work flat over the tool;
- Removal of tool dressing unit with an appropriate tool preparation technique.

3. Description of the improved IBAP setup

Figure 1 shows the configuration of improved setup made for in-situ preparation of IBAP tool for polishing of flat specimen. It consists of a refrigeration unit, a drive unit and a tool and work holding unit.

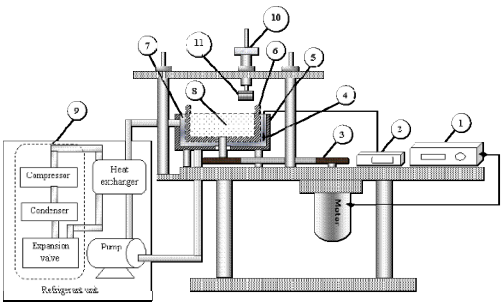

Fig. 1. Schematic of improved setup for flat specimen

[1. Motor speed control, 2. Temperature display unit, 3. Belt and pulley drive, 4. Thermocouple, 5. Stainless steel outer cylinder, 6. Stainless steel inner cylinder, 7. Annulus between the inner and outer cylinder, 8. IBAP tool, 9. Vapor compression refrigeration system, 10. Dead weight loading mechanism, 11. Workpiece holder]

3.1. Refrigeration unit

Figure 2 shows the refrigeration unit that was used to supply the refrigerant at low temperature to IBAP system. The unit basically consists of a primary refrigeration system, a coil-in-coil type heat exchanger and a secondary refrigerant unit. The primary refrigeration system, enclosed by dotted lines in Fig. 2, follows vapor compression refrigeration cycle where R134a is used as the refrigerant. As this refrigerant cannot be supplied directly to the open atmospheric condition prevailing in IBAP system, a secondary refrigerant is used to transfer the cooling effect to the IBAP system at ambient conditions. The heat transfer between the refrigerants occurs in coil-in-coil type heat exchanger. This secondary refrigerant is then pumped to the top of the stationary outer cylinder in IBAP system and is made to flow through the annulus between the outer and inner cylinders.

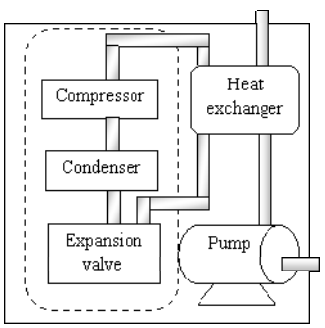

Fig. 2. Schematic diagram of the refrigeration unit employed in IBAP setup

Ethylene glycol, the most commonly used anti-freeze, was employed as the secondary refrigerant, since it is cheaper and readily available in the market. By adding 30% water to 70% ethylene glycol (by weight), the freezing temperature of the solution reduced to -50°C. A commercially available AC monoblock pump (9m head and 500 lph) was used to pump the secondary refrigerant to the IBAP system. This arrangement provided -20°C under no load conditions and -12°C when coupled with the IBAP setup. The extent of insulation needed to maintain this temperature in the setup was determined by trial and error.

3.2. Drive unit, tool and work holding unit

Figure 3 shows the drive unit which comprises of a DC motor and a belt and pulley arrangement, inner cylinder which holds the tool and work holder unit. The belt and pulley system connects the motor to the inner cylinder for rotation of the tool. The tool is firmly held inside the inner steel cylinder with the help of reinforcements that are provided at the bottom of the cylinder. The work holding unit is held flat against the tool by a straight horizontal arm during the polishing process.

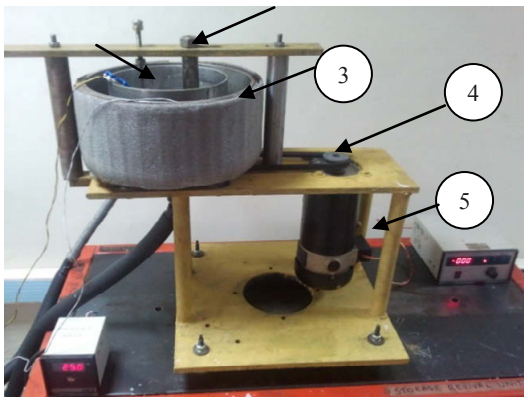

Fig. 3. A photograph of drive unit, tool holder and work holder units in IBAP setup
[1. Work holder, 2. Inner stainless steel cylinder, 3. Outer stainless steel cylinder with insulation, 4. Belt and pulley drive, 5. DC motor]

4. Preparation of IBAP tool

The slurry is prepared by mixing abrasives and water in a fixed concentration by weight, as shown in Table 2. It is then filled layer by layer, into the inner cylinder of the setup, shown in Fig. 3, to form the IBAP tool. To avoid unnecessary use of abrasives in the formation of tool, pure water was poured until the reinforcements submerge in it.

Unlike the previous setup which used liquid nitrogen, the refrigeration unit in the current setup took longer time to freeze the slurry. During this time, certain amount of settlement of abrasives at the bottom of the layer was observed. To avoid this particular drawback, the volume of slurry poured was limited to 20ml. Through various experiments carried out on the setup, it was observed that the temperature of the tool was 2-5°C less than the temperature of secondary refrigerant. To avoid under or over freezing of tool, the optimum temperature range of secondary refrigerant had to be -5°C to -10°C. The tool prepared was expected to have uniform distribution of abrasives in the ice.

5. Preliminary experimentation

The tool prepared with this improved setup was used to polish electrically condutive copper, 304L stainless steel and Ti6Al4V specimens employing optimum parameters found from the earlier studies [5], and these parameters are listed in Table 2. Each specimen of 22mm diameter and 18 to 20mm thick was first turned in CNC lathe and was then ground on surface grinding machine, before their polishing with IBAP tool.

Table 2. Process parameters of IBAP process

Abrasive	Silicon carbide, 2µm
Concentration by weight	10%
Polishing speed	150rpm
Polishing duration	15 minutes (Cu), 30 minutes (SS, Ti6Al4V)
Polishing load	25kPa

A stylus type roughness measuring (MAHR MARSURF perthometer) instrument was used to measure the finish, in terms of Ra, on the specimen.

6. Results and discussion

Table 3 shows the trends of improvement of finish on copper specimen polished using the earlier and improved IBAP setup. The improvement in surface roughness (Ra) was found to vary in the range of about 50-65% using the improved setup whereas the old setup gave around 52%.

Table 3. Improvement in surface finish (Ra) on copper specimen

Earlier setup [3]	51.95%
Current setup	
Sample 1	63.27%
Sample 2	51.40%
Sample 3	58.53%

Figure 4 shows trend of variation of surface finish for copper specimen polished with the current setup. This trend clearly shows the consistency of improvement in surface finish achieved on copper specimen. Figure 5 shows a similar trend of improvement in finish on

Ti6Al4V and 304L stainless steel specimen polished with IBAP tool.

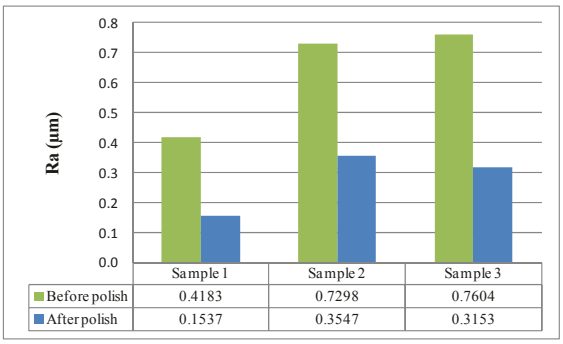

	Sample 1	Sample 2	Sample 3
Before polish	0.4183	0.7298	0.7604
After polish	0.1537	0.3547	0.3153

Fig. 4. Improvement in arithmetical mean roughness (Ra) for Copper specimens

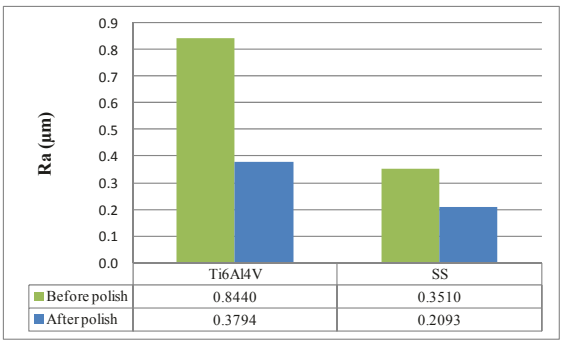

	Ti6Al4V	SS
Before polish	0.8440	0.3510
After polish	0.3794	0.2093

Fig. 5. Improvement in arithmetical mean roughness (Ra) with 8micron SiC abrasives

The percentage improvement in finish was about 55% for Ti6Al4V and 40% for 304L stainless steel. All these trends clearly demonstrate the effectiveness of the improved setup in polishing of different metallic specimen. Apart from this, the current setup made the task of preparing the IBAP tool easier and enhanced the life of the tool. Though the polishing trials conducted with the current setup was limited to 30 minutes, the refrigeration unit provided in the system is capable of maintaining the tool life for much longer period.

7. Conclusion

The developed IBAP setup included a vapor compression refrigeration unit that enabled precise temperature control during tool preparation. This avoided the formation of undesirable cracks and dents in the tool due to over cooling. The secondary refrigerant flow in the annulus between inner and outer cylinder of the IBAP setup helped in maintaining the tool temperature between -5°C to -10°C during polishing. This has considerably improved the life of tool. Polishing studies on copper, Ti6Al4V and 304L stainless steel specimen with the current setup demonstrated its feasibility to polish different metallic materials.

Acknowledgement: The authors would like to sincerely acknowledge the assistance of Mr.Elangovan and Mr.Srinivas, Refrigeration and Air conditioning laboratory, IIT Madras during the fabrication of refrigeration unit.

References

[1] Zhong ZW, (2008) Recent Advances in Polishing of Advanced Materials, Materials and Manufacturing Processes, 23(5):449-456

[2] Mohan R, Ramesh Babu N, (2011) Design, development and characterization of ice bonded abrasive polishing process, International Journal Abrasive Technology, 4(1):57-76

[3] Mohan R, Ramesh Babu N, (2010) Ultra-fine finishing of metallic surfaces with ice bonded abrasive polishing process, Proceedings of 36th International Conference on Manufacturing Automation and Systems Technology Applications Design Organisation and Management Research (MATADOR), Manchester, UK, 105-108

[4] De Koning JJ, De Groot G, Van Ingen Schenau GJ, (1992) Ice friction during Speed Skating, Journal of Biomechanics, 25(6):565-571

[5] Mohan R, Investigations on ice bonded abrasive polishing of metallic materials, PhD Thesis, IIT Madras.

Experimental investigation and FEA simulation of drilling of Inconel 718 alloy

Sureshkumar M.S[1], Lakshmanan D[2] and A. Murugarajan[1]
[1] Department of Mechanical Engineering, Sri Ramakrishna Engineering College, Coimbatore, India
[2] Park College of Technology, Coimbatore, India

Abstract. Drilling of Inconel alloy structures is widely used for aerospace components. Inconel 718, a high strength, thermal resistant Nickel-based alloy, is mainly used in the aircraft industries. Due to the extreme toughness and work hardening characteristics of the alloy, the problem of machining Inconel 718 is one of the ever-increasing magnitudes. This paper discusses the drilling cutting conditions on the machinability of Inconel 718. In this work, an empirical modelling is proposed for predicting the cutting force exerted during the drilling of alloy. The full factorial design is constructed based on the significant drilling process parameters. The cutting force is measured using the dynamometer.. The experiments are conducted on high speed radial drilling machine at a constant depth of cut. Using the experimental results the empirical model is developed for prediction of cutting force and verification results are compared with DEFORM 3D simulation software. The validation experiments are well correlated with empirical model and simulation results for prediction cutting force. However the proposed simulation model further to be considering chatter and vibration of the machine tool structure and different drilling tool geomentry.

Keywords: Inconel718, Drilling, Cutting force, DEFORM.

1. Introduction

The knowledge of cutting forces developing in the various machining processes under given cutting factors is of great importance, being a dominating criterion of material machinability, to both: the designer-manufacturer of machine tools, as well as to user. The prediction of cutting force helps in the analysis of optimization problems in machining economics, in adaptive control applications, in the formulation of simulation models used in cutting databases. Also it is useful to study the machinability characteristics of the work materials, to estimate the cutting power consumption during machining and in monitoring the conditions of the cutting tool and machine tool. Cutting force calculation and modeling are one of the major concerns of metal cutting theory [1]. The large number of interrelated parameters that influence the cutting forces (cutting speed, feed, depth of cut, primary and secondary cutting edge angles, rake angle, nose radius, clearance angle, cutting edge inclination angle, cutting tool wear, physical and chemical characteristics of the machined part, cutting tool coating type, chip breaker geometry, etc.) makes the development of a proper model a very difficult task. Although an enormous amount of cutting force related data is available in machining handbooks, most of such data attempt to define the relationship between a few of the possible cutting parameters whilst keeping the other parameters fixed.

In the aerospace industry, drilling accounts for nearly 40% of all the metal-removal operations [2]. About 60% of the rejections are due to the defects in the holes. These defects would create reduction in structural stiffness, leading to variation in the dynamic performance of the whole structure. Many of these problems are due to the use of non-optimal cutting tool designs, rapid tool wear, and machining conditions [3–5]. In conventional machining, the drilling by twist drill is the most applied method though as much as 40% for all materials removal processes [6]. Prediction of critical thrust force was the objective of several studies [7–11] during drilling of composites. With the recent rapid development of industry, the need has increased for precision drilling of special materials like Inconel 718 alloy, which is widely used in Gas turbines, rocket motors, spacecraft, nuclear reactors, pumps.

In this paper, an experimental analysis is carried out for prediction of drilling force in machining of Inconel 718 alloy Titanium Carbide drill bit. The full factorial experimental design is constructed based on the key process parameters includes feed rate and cutting speed. The experiments are carried out and cutting force exerted during machining of alloy is measured using the drill tool dynamometer. The empirical model is developed and verified with experimental results. Furthermore, the proposed empirical model is compared with FEA simulation using Deform 3D software.

Table 1. Input parameters

Parameters	Unit	Notation	Level 1	Level 2	Level 3
Cutting speed	rpm	*v*	450	640	820
Feed rate	mm/rev	*f*	0.104	0.211	0.315

2. Experimentation

Factorial designs are used widely in experiments involving several factors on a response. The meaning of factorial design is that each complete test or replications of all the possible combinations of the levels of the factors are investigated [2]. Using full factorial design of experiment, empirical model of cutting force as a function of speed (v), feed (f) have been developed with 95% confidence level. These model equations have been used to predict the cutting force. Table 1 shows the variables and their levels considered for the experimentation.

Inconel 718 alloy of dimensions 110mm x 40mm x 6 mm plate is used for the experiment. Drilling is performed by a radial drilling machine (Model P2/25/GTA).The experiment is carried out by Titanium Carbide drill bit of 6.1mm diameter under MQL condition. The cutting force measurement is acquired by drill tool dynamometer (strain gauge type). Figure 1 shows the schematic view of the experimental setup. Figure 2 shows the photographic view of the setup. The experiments were carried out and the cutting force measurements were observed from the digital output of the drill tool dynamometer.

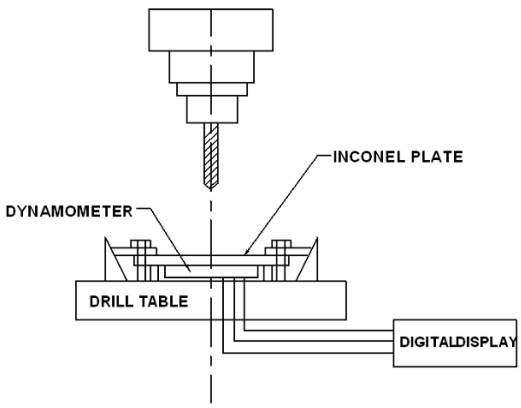

Fig. 1. Schematic view of the experimental setup.

Fig. 2. Photograph of the experimenta setup

3. Emperical cutting force model

The empirical model of cutting force is formed as the relationship between dependant output variable and the two independent input parameters. The functional relationship between output parameter with the input parameters could be postulated using the following equation,

$$F_r = Av^a f^b \tag{1}$$

The above non-linear equation is converted into linear form by logarithmic transformation and can be written as

$$log\, F = log\, A + a\, log\, v + b\, log\, f \tag{2}$$

The above equation can be written in the linear form as as

$$y = \lambda_0 + \lambda_1 v + \lambda_2 f \tag{3}$$

Where, y is the true value of dependent machining output on a logarithmic scale *v* and *f* are the logarithmic transformation of the different input parameters λ_0, λ_1 and λ_2 are the corresponding parameters to be estimated. The empirical model of cutting force is formulated using the experimental conditions and measured force with the help of MINITAB software. The measured cutting force values for given experimental conditions are summarized in Table 2. The empirical model was developed based on measured cutting force and it is formulated as,

$$F = 112 + 0.098v + 708\, f \tag{4}$$

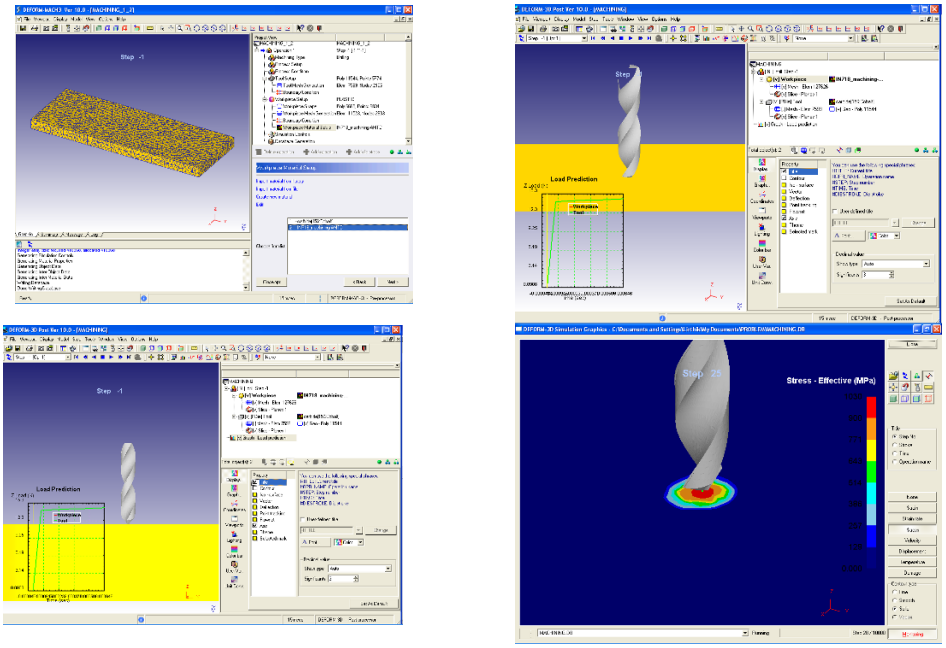

Fig. 3. Screen shot of different steps involved in drilling simulation of Inconel 718 alloy using DEFORM 3D

4. FEA simulation model

DEFORM-3D is a robust simulation tool that uses the finite element method (FEM) to model complex machining processes in three dimensions[12]. One of the most recent processes that has been modeled in DEFORM is drilling. During the drilling simulation, the cutting edges of the drill bit are shearing the workpiece material at different cutting speeds which separate the material from the workpiece by chip formation. Initially, a parting line model was assumed to simplify the simulation process. The stress distribution is simulated and further software can predict the cutting force with help of machining simulation capabilities. A machining specific preprocessor streamlines the setup of routine drilling simulations. Figure 3 shows screen shot of different steps involved in simulation of drilling of Incone 718 alloy using DEFORM 3D. The different runs of trial is conducted for the experimental conditions. The obtained simulated cutting force results are summarized in Table 2.

5. Experimental results

The experiments were carried out using carbide drilling tool for the experimental conditions. The predicted force calculated from empirical formula, measured resultant forces acquired using dynamometer and the forces calculated from simulation model and empirical model are tabulated in Table 2.

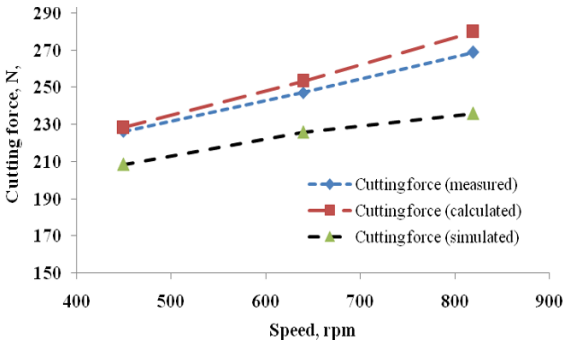

(a) Speed vs Cutting force at feed of 0.104 mm

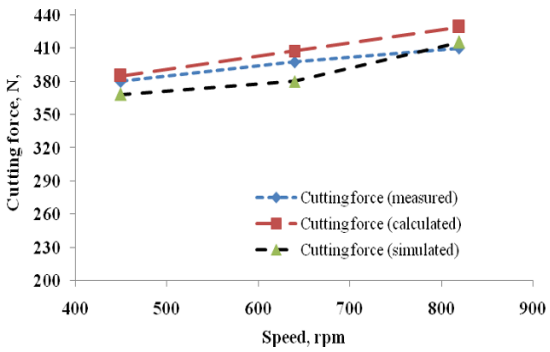

(b) Speed vs Cutting force at feed of 0.315 mm

Fig. 4. Cutting force obtained at different feed rate

Table 2. Measured, calculated and simulated cutting force values at different experimental conditions.

Exp No	Speed (v) rpm	Feed (f) mm/rev	*Cutting force, N*		
			Measured	*Calculated using emprical formula*	*Simulated from FEA model (DEFORM -3D)*
			F_{Ex}	F_{Em}	F_{Si}
1	450	0.104	226.33	228.33	208.59
2	450	0.211	295.45	301.45	256.49
3	450	0.315	380.34	385.34	368.46
4	640	0.104	247.27	253.27	225.95
5	640	0.211	301.34	301.34	265.56
6	640	0.315	397.73	407.73	380.31
7	820	0.104	268.92	279.92	236.05
8	820	0.211	332.48	345.48	304.94
9	820	0.315	410.33	429.33	415.69

It is observed that increasing the feed rate leads to increase in cutting force exerted during drilling of Inconel 718 alloy. Also similar trend is observed when increasing the speed. The results revealed that measured cutting force good agreement with calculated force using empirical model and FEA simulation model as shown in Fig. 4. However, the experiments are to be conducted for full factorial design and considering surface finish and delaminating factor to be useful for further research.

6. Conclusion

The following conclusions are found out from experimental and empirical model results. The cutting force could be effectively predicted by using spindle speed and feed rate as the input parameters for drilling of Inconel 718 alloy using carbide drilling tool. Also apart two input process parameters, feed rate was found to be the most influencing parameter compared with spindle speed. The predicted values from empirical analysis are compared with FEA Simulation model using DEFORM-3D. The results showed are in well agreement with experimental results. It is suggested that a proposed empirical relationship for the measurement uncertainty should always be provided in cutting force measurements, with account being taken of process-related contributions and external disturbances. Furthermore, the model enables the prediction of the uncertainty of cutting force measurements for a defined range of cutting parameters such as considering tool wear, chatter and vibration of the machine tool and data acquisition.

References

[1] Tamas Szecsi, (1997) Cutting force modelling using artificial networking. Mater. Process Technol 92-93: 344-349.

[2] Subramanian K, Cook NH. (1997) Sensing of drill wear and prediction of drill life. Transactions of the ASME, Journal of Engineering for Industry. 99:295–301.

[3] Konig W, Cronjager L, Spur G, Tonshoff HK. (1990) Machining of new materials. Ann CIRP : 39(2):673–80.

[4] Komanduri R (1997). Machining of fibre reinforced composites. Mach Sci Technol; 1(1):113–52.

[5] Davim JP, Pedro Reis, Conceicao Antonia. (2004) Experimental study of drilling glass fiber reinforced (GFRP) manufactured by hand lay-up. Comp. Sci Tech.; 64:289–97.

[6] Brinksmeier, E.(1990). Prediction of tool fracture in drilling. Ann CIRP: 39 (1), 97–100.

[7] Hocheng H, Dharan CKH. (1990) Delamination during drilling in composite laminates. Trans ASME ;112:236–9.

[8] Bhatnagar N, Naik NK, Ramakrishnan N. (1993) Experimental investigations of drilling on CFRP composites. Mater Manufact Process ;8(6):683–701.

[9] Xin W, Wang LJ, Tao JP. (2004) Investigation on thrust force in vibration drilling of fiber-reinforced plastics. J Mater Process Technol : 148:239–44.

[10] Tsao CC, Hocheng H. (2005) Effect of eccentricity of twist drill and candle drill on delamination in drilling of composite materials. Int J Mach Tools Manufact; 45:125–30.

[11] Singh I, Bhatnagar N, Viswanath P (2008) Drilling of uni-directional glass fiber reinforced plastics: experimental and finite element study. Mater Des:299(2):546-553

[12] Gardner JD, Dornfeld, D (2006) Finite element modelling of drilling using DEFORM, Consortium on deburring and Edge finishing.

Performance evaluation of bandsaw using scientific method when cutting tool steels

M. Sarwar[1], J. Haider[2], M. Persson[3] and H. Hellbergh[3]
[1] School of CEIS, Northumbria University, Newcastle upon Tyne, NE1 8ST, United Kingdom
[2] School of Engineering, Manchester Metropolitan University, Manchester M1 5GD, United Kingdom
[3] R&D Saws, SNA Europe, Fiskaregatan 1, Lidkoping, Sweden

Abstract. Bandsawing is a key primary machining operation for cutting off raw material into required dimensions, which is subjected to further secondary machining operation(s) to manufacture a product or a component. Bandsawing is distinctively characterised from other multipoint cutting operations with small depth of cut or feed per tooth (5 µm - 50 µm) compared to the cutting edge radius (5 µm - 15 µm). Bandsawing performance significantly differs depending on workpiece material characteristics. In the current investigation, performance of bandsawing operation has been scientifically evaluated when cutting two different tool steel materials (Orvar Supreme and Sverker). Bandsawing tests were carried out with 6 different cutting speeds ranging from 31 m/min to 90 m/min and four different depths of cut ranging from 1 µm to 4 µm. Cutting forces and thrust forces were continuously measured throughout the cutting tests. Specific cutting energy parameter calculated based on cutting force and material removal data has been used to quantitatively measure the efficiency of the metal cutting process at different feeds and speeds. The bandsaw teeth at the worn condition have been studied under a Scanning Electron Microscope to identify wear modes and mechanisms. The chip characteristics at different feeds and speeds have also been discussed. The sawing community including bandsaw end users and design engineers should find the results presented of interest.

Keywords: Bimetal Bandsaw, Bandsawing, Tool steel, Cutting Force, Specific Cutting Energy, Wear

1. Introduction

Bandsawing is a primary machining operation extensively used by steel stockholders and steel manufacturers to cut off raw materials in a suitable size for secondary machining operations (turning, milling, drilling etc.). Bandsawing process has not been studied by the scientific community to the same depth and extent as in other machining opearations. Several researchers in the past have contributed to the understanding of the bandsawing process [1-8]. Particularly, Thompson, Sarwar and colleagues were very instrumental in distinguishing the bandsawing from other machining operations with the following characteristics: multipoint intermittent cutting action, small feed per tooth (5 µm - 50 µm) compared to the edge radius (5 µm - 15 µm), smaller chip ratios (0.1 as compared 0.3 in turning), variation in number of active cutting edges in contact with the workpiece, restricted chip flow in bandsaw gullets etc.

New materials with improved properties are constantly being developed to meet the demand for different applications. Machining community faces the challenge of efficiently cutting the newly developed materials. Knowledge and understanding of chip formation mechanism, optimum machining parameters, forces developed in the cutting tool and tool wear characteristics are essential to minimise the machining cost, to extend tool life and to improve product quality. Previously the authors scientifically evaluated the bandsawing performance of several steel workpieces (ball bearing steel, stainless steel, Ni-Cr-Mo steel) by studying chip formation mechanism, measuring forces and specific cutting energy (Esp) and establishing wear modes and mechanisms in bandsaw teeth [5, 6]. The aim of this investigation is to assess the performance of bandsaws when cutting tool steel workpieces at different cutting parameters. Esp has been used to quantitatively measure the bandsawing efficiency as it is more sensitive to low depths of cut, which is the case in bandsawing.

2. Experimental procedure

2.1. Workpiece material

Two different tool steels were selected as workpiece materials for the bandsawing investigation. The details of the workpeice materials are given in Table 1. Orvar supreme is particularly useful for casting dies, forging tools and extrusion tools. Sverker is recommended for

applications such as blanking and shearing tools, press tools, forming tools and plastic moulds.

Table 1. Workpiece materials details

Material characteristics	Workpiece 1	Workpiece 2
Trade name	Orvar Supreme (BS 4659 BH13)	Sverker (BS 4659 BD6)
Bar dimension	254 mm × 153 mm	254 mm × 153 mm
Vickers Hardness 5 kg (Kgf/mm^2)	200	260
Chemical composition (wt%)	C (0.32-0.42); Si (0.85-1.15); Mn (0.40); S (0.035); Cr (4.75-5.25); Mo (1.25-1.75); Ni (0.40); V (0.90-1.10)	C (2.05); Si (0.30); Mn (0.80); W (1.10); Cr (12.70)

2.2. Cutting tool

Variable pitch bimetal bandsaws (M42 High Speed Steel welded to low alloy backing material) in the form of loops were used for the machining tests. The band thickness, width, tooth pitch and loop length were 1.6 mm, 54 mm, 1.4/2 TPI and 8.8 m respectively. The rake angle and clearance angle of each tooth were 10^o and 35^o.

Fig. 1. Bandsaw (1.4/2 TPI) teeth used in this investigation

Fig. 1 shows a section of the bandsaw used. The bandsaw teeth were set according to the sequence of Right (R) - Left (L) - Neutral (0).

2.3. Machining test

A fully instrumented vertical feed bandsaw machine (NC controlled, Behringer HBP650/850A/CNC) was used to carry out the full bandsaw cutting tests by sawing off small sections from a long workpiece. Fig. 2 shows the experimental set-up and cutting and feed directions during bandsawing. The bandsaw machine was calibrated using a 3-axis Kistler dynamometer and relevant transducers. Cutting force and thrust force components, cutting speed and feed rate were measured during the bandsawing tests. The test conditions are given in Table 2. The saw blade was flooded with a coolant (Castrol Cooledge) during sawing at a flow rate of 3.8 liters/min. Samples of cutting edges were examined using a scanning Electron Microscope (SEM). Chips were also collected for different test conditions in order to characterise them

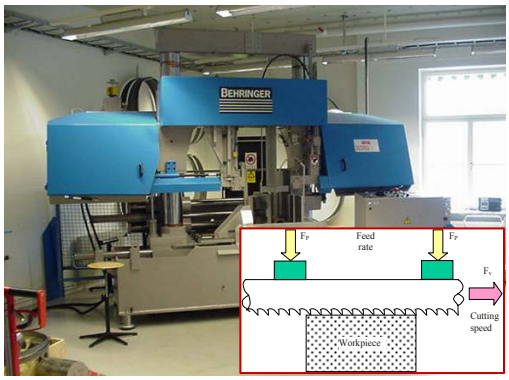

Fig. 2. Experimental set-up used for bandsawing tests with schematic diagram of cutting and feed directions

Table 2. Machining conditions for the selected workpieces

Material	Cutting speed (m/min)	Set depth of cut per tooth or Feed (µm)
Orvar Supreme	31, 45, 60, 75, 90	1, 2, 3, 4
Sverker	31, 40, 50, 60	1, 2, 3, 4

3. Results and discussions

3.1. Forces and specific cutting energy

The cutting and thrust forces generated at different depths of cut and cutting speeds with Orvar supreme and Sverker are presented in Fig. 3 and Fig. 4 respectively. The forces increased with the increase of depth of cut per tooth due to the higher material removal rate. In general, cutting forces (Fv) were higher than the thrust forces (Fp) [8]. However, in some cases Fv was equal to Fp or Fp was even slightly greater than Fv. The combination of cutting parameters and material characteristics could be responsible for this.

The specific cutting energy (Esp) was calculated from cutting force and material removal rate data [7] and presented in Fig. 5 and Fig. 6 for the workpiece materials. All the curves showed exponential nature with the depths of cut. At low depth of cut, the machining efficiency was

poor as indicated by higher Esp due to the significant edge radius effect or size effect (edge radius being greater than the depth of cut). The decrease of edge radius effect at higher depth of cut indicated a better machinability characteristic (lower Esp). For Orvar Supreme the general trend of Esp was satisfactory i.e., the cutting efficiency improved with the increase in cutting speed. However, the bandsawing efficiency deteriorated with the increase in cutting speed when cutting Sverker possibly due to a different material characteristic.

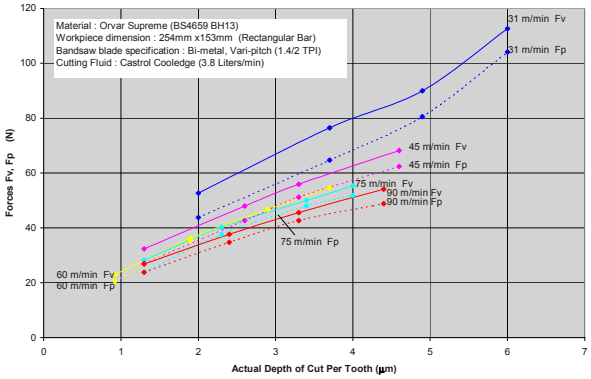

Fig. 3. Influence of cutting speed on forces when cutting Orvar Supreme workpiece

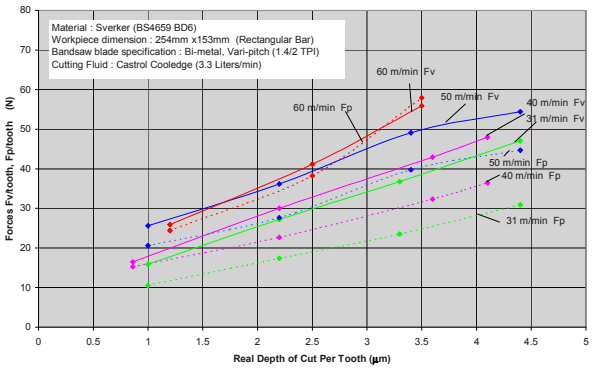

Fig. 4. Influence of cutting speed on forces when cutting Sverker workpiece

It should be noted that the actual depths of cut achieved (Fig. 3 to Fig. 6) by the bandsaw were not equal to the set depths of cut (Table 2). The depth of cut achieved per tooth was influenced by the cutting speed and furthermore by the workpiece material characteristics.

3.2. Cutting edge wear chracteristics

At the new condition, the cutting edges were nominally sharp. However, at high magnification under SEM sign of damage along the cutting edge was visible possibly due to the breaking of very small grinding edge-burr during the production of the teeth. This process created an edge radius of approximately 7 µm.

Bandsaw teeth are worn in such a way that wear flat (flank wear) was produced at the tip of each tooth and the outer corners of the teeth are rounded (corner wear). The SEM pictures of the worn cutting edges are presented in Fig. 7 after cutting 20 sections of Orvar Supreme and Sverker materials. It was established that flank and corner wear were the principal wear modes. A combination of abrasion and adhesion were identified as the underlying mechanisms of the flank and corner wear [5, 6]. However, workpiece adhesion on the bandsaw cutting edge was more severe for cutting Sverker than Orvar Supreme. Rake face wear was generally not as severe as the flank wear. The wear in bandsaw tooth alters the edge geometry and affects the chip formation mechanism [8].

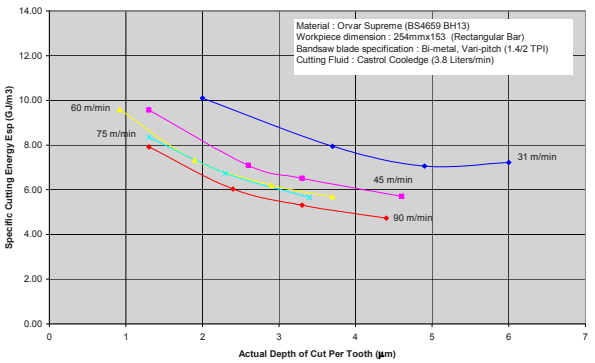

Fig. 5. Influence of cutting speed on specific cutting energy when cutting Orvar Supreme workpiece

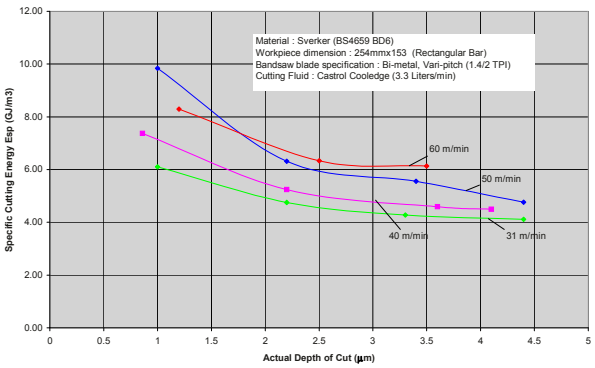

Fig. 6. Influence of cutting speed on specific cutting energy when cutting Sverker workpiece

3.3. Chip chracteristics

Fig. 8 and Fig. 9 present the examples of chips produced during machining of the two workpiece materials at different bandsawing parameters. In general, long chips were found when machining Orvar Supreme material. However, chips produced from Sverker were generally shorter. In case of Orvar Supreme, the chips turned into more curly shape with the increasing speed irrespective of the depth of cut. On the other hand, for Sverker the chips turned into more curly shape with the increasing speed at

low depth of cut only. At higher depth of cut, the chips became shorter and straighter.

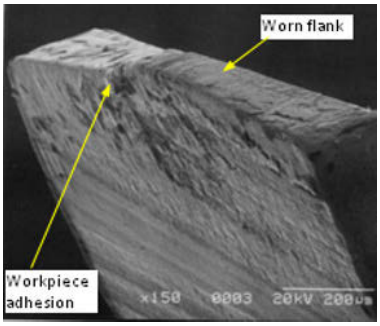

a

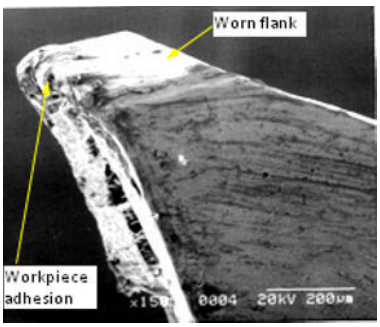

b

Fig. 7. SEM pictures of worn bandsaw teeth after 20 cuts when cutting (a) Orvar Supreme and (b) Sverker workpieces

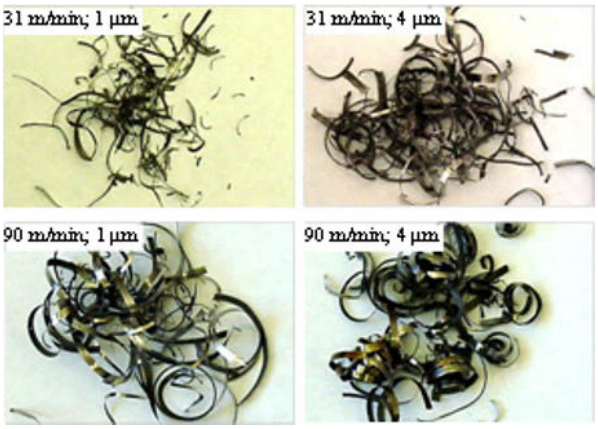

Fig. 8. Chip characteristics when cutting Orvar Supreme material at different combinations of speeds and depths of cut

4. Conclusions

The following conclusions can be drawn from the full bandsawing tests carried out on two different tool steel materials (Orvar Supreme and Sverker). The forces (cutting and thrust) were influenced by the cutting speed and depth of cut (forces increase). The bandsawing efficiency increased (lower Esp) with the cutting speed when cutting Orvar Supreme. However, with the increase in cutting speed, the bandsawing operation became less efficient for Sverker (higher Esp). Flank and corner wear were caused by a combination abrasion and adhesion. Workpiece adhesion on the worn flank was more prominent for Sverker. The characteristics of the chips produced during bandsawing were influenced by workpiece materials and cutting parameters.

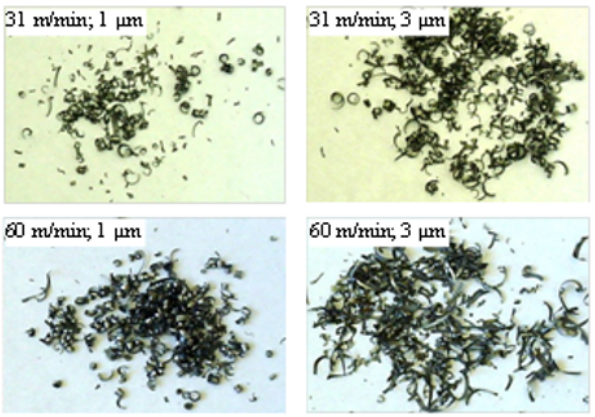

Fig. 9. Chip characteristics when cutting Sverker material at different combinations of speeds and depths of cut

References

[1] Colwell LV, McKee RE, (1954) Evaluation of bandsaw performance, Transactions of the ASME 77:951–960

[2] Sarwar, M, Thompson PJ, (1974) Simulation of the cutting action of a single hacksaw blade tooth, The Production Engineer 53:195-198

[3] Ahmad MM, Hogan B, Goode E, (1989) Effect of machining parameters and workpiece shape on a bandsawing process, International Journal of Machine tools and Manufacture 29:173–183

[4] Andersson C, Stahl JE, Hellbergh H, (2001) Bandsawing. Part II: detecting positional errors, tool dynamics and wear by cutting force measurement, International Journal of Machine Tools and Manufacture 41:237-253

[5] Sarwar M, Persson M, Hellbergh H, (2005) Wear and failure modes in the bandsawing operation when cutting ball-bearing steel, Wear 259:1144–1150

[6] Sarwar M, Persson M, Hellbergh H, (2007) Wear of the cutting edge in the bandsawing operation when cutting austenitic 17–7 stainless steel, Wear 263:1438–1441

[7] Sarwar M, Persson M, Hellbergh H, Haider J, (2009) Measurement of specific cutting energy for evaluating the efficiency of bandsawing different workpiece materials, International Journal of Machine tools and Manufacture 49:958-965

[8] Sarwar M, Persson M, Hellbergh H, Haider J, (2010) Forces, wear modes and mechanisms in bandsawing steel workpieces. IMechE Proceedings Part B: Journal of Engineering Manufacture 224:1655-16662